CO_2 Human Emissions

Sampling Strategy for additional tracers

F Chevallier and the WP4 CHE partners

Co-ordinated by ECMWF

D4.4 Sampling Strategy for additional tracers

Dissemination Level:	Public
Author(s):	F Chevallier (CEA)
Date:	04/02/2021
Version:	1.0
Contractual Delivery Date:	31/12/2020
Work Package/ Task:	WP4/ T4.3
Document Owner:	CEA
Contributors:	EMPA, MPG, NILU, UEA
Status:	Final

CHE: CO2 Human Emissions Project

Coordination and Support Action (CSA)
H2020-EO-3-2017 Preparation for a European capacity to monitor CO2 anthropogenic emissions

Project Coordinator: Dr Gianpaolo Balsamo (ECMWF)
Project Start Date: 01/10/2017
Project Duration: 39 months

Published by the CHE Consortium

Contact:
ECMWF, Shinfield Park, Reading, RG2 9AX,
gianpaolo.balsamo@ecmwf.int

The CHE project has received funding from the European Union's Horizon 2020 research and innovation programme under grant agreement No 776186.

Table of Contents

Executive Summary

Using new modelling and experimental results, this report synthesizes the CHE effort to assess the potential value of ground-based tracer measurements related to fossil fuel (FF) carbon dioxide (CO_2) within an anthropogenic CO_2 emissions Monitoring and Verification Support capacity (CO_2MVS) and in addition to the future Copernicus CO_2 monitoring (CO2M) satellite measurements. It attempts at defining a sampling strategy for these tracers. This report explores the practical implications of distinguishing between anthropogenic (meaning fossil fuel emissions, and also non-fossil waste burning, biofuels, etc.) vs. biogenic CO_2 fluxes. It is specifically dedicated to the optimization of the space-time sampling of radiocarbon (^{14}C in CO_2), carbon monoxide (CO) and Atmospheric Potential Oxygen (APO). Its strategy relies on a series of numerical simulations prepared by CEA/LSCE, EMPA, MPG and NILU, with the help of TNO and UEA. They cover some of Europe with unprecedented detail, including for the spatial variability of the corresponding emissions per emission type. The report also exploits experimental results obtained during the first Covid-19 lockdown restrictions in the United Kingdom and analysed by UEA.

CEA/LSCE analysed the uncertainty reduction brought by the CO2M satellite retrievals in combination with ground-based measurements of either $^{14}CO_2$, CO_2 or CO. These results bring contrasted conclusions regarding the potential of the combination between the satellite observation and surface networks. The satellite, as a stand-alone system, is seen to yield accurate estimates of the regional budgets of FF emissions in the morning of its days of overpass within its field of view and in favourable observation conditions, but it does not provide direct information on emissions during the afternoon or during the night, and hardly provides information on plants, cities and regions outside its field of view. The need for complementary sources of information to derive daily to annual budgets is thus critical. The results confirm that there is a large impact of the uncertainties in the Net Ecosystem Exchange (NEE) for the estimate of the FF emissions, but uncertainties in biofuel emissions do not appear to have a significant impact on the estimate of FF emissions with current biofuel emission levels. Relatively dense surface networks of CO_2 and radiocarbon measurements close to highly emitting areas can help further decrease the uncertainty in the FF emissions estimates when combined with satellite observations, in contrast to isolated rural stations. This suggests that surface CO_2 and/or $^{14}CO_2$ measurements in support of the FF emission monitoring should be targeting FF emission areas directly rather than the surrounding biosphere. Both hourly CO_2 and daily $^{14}CO_2$ data can provide useful information on the FF emissions, the former catching the signature of these emissions at high frequency and the latter being much less sensitive to the uncertainties in the NEE. The results also indicate little information from sparse CO surface networks when combined with CO_2 satellite and surface observations: the level of independence between the FF CO and FF CO_2 emissions appears to be too high to reach finer precision in the FF CO_2 estimates when adding CO data compared to those reached with CO_2 data only, or even to those from state-of-the-art prior inventories. Finally, the results also show an overall decrease of the potential from each observation subsystem studied here rather than an amplification of these potentials when combining them into a large observation system with satellite and surface data. This is the natural consequence of the asymptotic convergence of the precision of inversions towards low values when adding observations. These various results support the deployment of very dense CO_2/$^{14}CO_2$ surface networks to complement the satellite observation, with at least three sites per European administrative region. The large-scale deployment of such dense networks is probably unaffordable for the coming decade, but some regions are now equipped with many stations and in some locations, the complementarity between satellite and surface networks could thus be demonstrated. Frequent (up to daily) samplings of $^{14}CO_2$ would be needed to ensure $^{14}CO_2$ data can bring information on FF emissions more precise than that of hourly CO_2 stations.

EMPA analysed near-surface emission signals of $^{14}CO_2$, CO_2 and CO. Long-range transport from neighbouring regions appeared to play a minor role in the measurement variability. This

implies controlling the fluxes at high resolution in the atmospheric inverse systems rather than in the form of aggregated fluxes in large regions. Radiocarbon measurements seem to be affected by nuclear power plant emissions only in their close proximity (within about 100 km) and only during the periods when some plant plume reaches the station: filtering out such periods should make it possible to minimize interferences from nuclear power point signals. In general, in winter, fossil fuel emissions strongly dominate $^{14}CO_2$ variability (90% - 100%) over most of Europe. However, in summer their contribution drops to 70%-80% due to a non-negligible contribution from biospheric fluxes. CO could be a particularly valuable tracer of fossil fuel emissions during summer, when the use of biofuels is reduced. However, this would not be true during periods of biomass or agricultural waste burning. Further, since variations in background CO concentrations are relatively large in summer, it would be necessary to separate large-scale variations in background CO from smaller-scale variations in fossil fuel CO. With a sufficiently dense measurement network, such a separation should be feasible. As shown in some previous studies (but in contrast to the CEA/LSCE conclusion), CO could also be useful as a high-frequency tracer that can be used to interpolate between typically weekly ^{14}C measurements at the same site. However, since CO has a large contribution from biofuels, this can only be successful if the signals from biofuels and fossil fuels are strongly correlated.

MPG initially performed an analysis of the station footprints and showed the possibility to group the stations into regional clusters based on the correlations of their footprints. For a continental-wide observing system, at least one station per cluster is required. Furthermore, stations near urban centres were shown to be more sensitive to fossil fuel emissions and stations far from urban centres appeared to be more sensitive to biospheric emissions. While it is clear that stations near cities are required to constrain the fossil fuel emissions, it is important to keep in mind that atmospheric inverse modelling is based on the gradients between stations. Hence, the network should have stations upwind and downwind from the cities in order to capture gradients. The different tracers studied were found complementary. In the determination of FF emissions from atmospheric measurements, APO had the best performance except for coastal stations, where oceanic fluxes can impede the accurate determination of FF emissions. Furthermore, although APO is a tracer that was design to be conservative with respect biospheric fluxes, MPG observed that biospheric fluxes have non-negligible contributions to the regional APO signal because the oxidative ratios of photosynthesis and respiration deviate from the -1.1 ratio that defines the APO tracer. $\delta^{14}CO_2$ observations, which are assumed to be the “gold-standard” to determine FF emissions because fossil fuels are void of ^{14}C, have significant interference from $^{14}CO_2$ emissions from gas-cooled nuclear power plants, biospheric fluxes and biomass burning emissions. Importantly, studies to determine FF emissions based on atmospheric measurements have often only considered fossil fuel emissions and biospheric fluxes (photosynthesis and respiration). Yet, in this study MPG found significant interference from biomass burning emissions across the domain even though Western Europe is not a region with strong biomass burning emissions. The analysis of uncertainty of the inverse model results provided important information on how well the signals from different regions and processes were constrained. However, it was not capable of fully separating the contribution from fossil fuels and the contribution from the rest of the flux processes.

NILU performed forward and backward simulations around the city of Oslo for CO_2, CO, $^{14}CO_2$ and APO. While assessing anthropogenic emission fluxes of CO_2, measurements in or close to the city centre were shown to provide a stronger constraint than rural sites. NILU tested the hypothesis that stations located within the highest emitting grid cells provide the most information. They found that when using a limited amount of measuring points, the accuracy of the retrieved fluxes has a weak correlation with the measurements located in the highest emitting cells. The alternative arrangement consists in measurements up and downwind from the highest emitting grid cells, such as in a ring distribution around the city centre, in agreement with previous examples described in the literature. In the configuration used here, the weak correlation with the city centre holds for calculations with the three different proxy CO_2^{ff} (CO,

^{14}C, and APO) tracers. However, in the idealised setting used here, there is sufficiently good knowledge of the background magnitude of the additional tracers and only perturbations thereof are studied. In a more realistic setting great care should be taken in properly assessing the background of all three species. A similar statement applies to the factors used to convert each additional tracer and CO_2^{ff} as these vary with season and location and likely have long term trends.

UEA detected a reduction in fossil-fuel-derived CO_2 mole fraction ($ffCO_2$) in the atmosphere associated with the Covid-19 lockdown restrictions in the UK with a machine learning approach combining discrete APO samples and continuous atmospheric CO_2 data. This novel approach circumvents the traditional pitfalls of the discrete sampling of APO, one of the best $ffCO_2$ tracers, as illustrated here by the MPG simulations.

All these works highlight the complex link between the CO_2, CO, $^{14}CO_2$, CO and APO atmospheric tracers on the one hand, and the CO_2 fossil fuel emissions on the other hand. This complexity comes with modelling uncertainties that remain too large for a CO_2 emissions Monitoring and Verification Support capacity to rely on a single tracer. The observation system has therefore to expand into a robust system of systems where redundancy among information sources compensates for modelling errors, and where complementarity among tracers compensates for the temporary blindness of some data sources during longer or shorter periods of time.

1 Introduction

1.1 Background

The initial CO_2 report commissioned by the European Commission (Ciais et al., 2015) highlighted the need to complement the satellite observation system that is now called the Copernicus Anthropogenic Carbon Dioxide Monitoring (CO2M) constellation, with routine measurements of additional trace species of fossil fuel CO_2 such as radiocarbon (^{14}C in CO_2) and carbon monoxide. The motivation behind this requirement of a ground-based component for the anthropogenic CO_2 emissions Monitoring and Verification Support (CO_2MVS) capacity (e.g., Janssens-Maenhout et al., 2020) was twofold: (i) separating fossil CO_2 emissions from biogenic fluxes at regional scale, and (ii) independently evaluating the satellite-based emission estimates. For radiocarbon, Ciais et al. (2015) recommended the deployment of approximately 50 sampling stations across the European continent, with higher density over regions with high emissions. We can now add Atmospheric Potential Oxygen (APO) to the list of relevant additional trace species of fossil fuel CO_2 further to the work of Pickers (2016).

In practice, different strategies can be envisaged to use these additional tracer measurements: the link between CO_2 fossil emissions and these measurements can be established at the concentration level (using a constant or weakly-varying concentration ratio), or at the emission level (assuming some correlations between CO_2 and tracer emission errors in the inventories, or assuming that the inventory emission ratio is correct or can be optimized from the measurements); additional tracers can also be combined together (for instance to interpolate infrequent radiocarbon samples in time, by assuming that their ratio is constant or weakly variable). In addition to its hypotheses, each method requires a clean background reference for the additional tracers, their non-fossil fuel sources need to be well quantified (e.g., emissions from nuclear power plants for radiocarbon measurements) and modelling uncertainty need to be fairly accounted for (e.g., for the vegetation isotopic signature in the case of radiocarbon measurements, or for emission ratios in the case of tracers co-emitted with CO_2).

This report explores the practical implications of distinguishing between anthropogenic (meaning fossil fuel emissions, and also non-fossil waste burning, biofuels, etc.) vs. biogenic CO_2 fluxes. It is specifically dedicated to the optimization of the space-time sampling of $^{14}CO_2$, CO and APO. Its strategy relies on a series of numerical simulations prepared by CEA/LSCE, EMPA, MPG and NILU, with the help of TNO and UEA. They cover some of Europe with unprecedented detail, including for the spatial variability of the corresponding emissions per emission type. This work follows and builds on CHE deliverables:

- D4.1, “Current European in-situ atmospheric measurement capacity”, that summarized the current European in-situ atmospheric measurement capacity and typical sampling for CO_2, CO, $^{14}CO_2$ and APO),
- D4.2, “Database of high-resolution scenarios of CO_2 and CO emissions”, that provided high-resolution scenarios of CO_2 and CO emissions associated with anthropogenic activities in Europe over a full year including associated uncertainty statistics and documentation, and
- D4.3, “Attribution Problem Configurations”, that described the specific configurations implemented in the four modelling frameworks to study the attribution problem.

This work also exploits Section 7 of CHE deliverable D1.3 “Reconciliation of top-down and bottom-up estimates of the carbon balance”, written by UEA about the potential benefits of including continuous fossil-fuel-derived CO_2 mole fraction ($ffCO_2$) tracers in Europe’s surface greenhouse gas network.

1.2 Scope of this deliverable

1.2.1 Objectives of this deliverables

This deliverable synthesizes the CHE effort to assess the potential value of additional ground-based tracer measurements related to fossil fuel CO_2 using new modelling and experimental results. It attempts at defining a sampling strategy for these tracers. The ensemble of contributions to this report allows for the representation of different views on the complexity of the attribution problem and different strategies to address it, so that a consensus can be reached on a factual basis.

1.2.2 Work performed in this deliverable

This deliverable is based on new experimental work performed in CHE WP1, and forward modelling and inverse modelling work performed in CHE WP4.

1.2.3 Deviations and countermeasures

This deliverable required much more complex modelling work than initially anticipated due to the high resolution of the simulations. The technical challenges related to the massive amount of computation needed for realistic model forward and inverse simulations have therefore slowed progress down and the study extended over four more months than planned.

2 Assessment from CEA/LSCE

2.1 Introduction

Within this project, CEA/LSCE has developed a high dimensional inversion framework designed for the co-assimilation of CO_2 and additional tracers of fossil fuel (FF) emissions (CO, $^{14}CO_2$ ground-based observations) and separately controlling emissions from large industrial plants, cities and regional budgets of more diffuse emissions. Such a high-resolution control vector avoids over-optimistic assessment of the capability of sparse observation systems, but involves a very large computational burden. First tests indicated a weak statistical constraint from the CO data. We therefore decided to separately consider the assimilation of CO and $^{14}CO_2$ in order to optimize the computational effort for each tracer. For the "CO-CO_2 inversion configuration", we prioritize the control of the different sectors of anthropogenic activity emitting both CO_2 and CO (traffic, domestic and commercial heating etc.) for each target area but we focus on Belgium only. For the "$^{14}CO_2$-CO_2 inversion configuration", we do not need the sectoral resolution and can put the priority on the distinction between various regions around Belgium in the control vector. The two configurations are described in detail in the D3.4 CHE report "Inversion strategy based on OSSEs".

Our study considers retrievals of the CO_2 column-average dry air mole fraction (XCO_2) from individual tracks from a CO_2M-like satellite in western Europe at 12:00 local solar time (LST). The inversions are conducted over 1-day windows from 00:00 to 24:00 (LST hereafter) on different days. Previous studies like Broquet et al. (2018) and Santaren et al. (2020) have shown that the direct information on CO_2 FF emissions from XCO_2 imagery with current measurement precision applies to periods of a few hours before the satellite overpass only. After a few hours, with air having been transported over typically 100 km, the signal from individual FF CO_2 sources (plants, cities, regions) is much diffused and hardly detectable in XCO_2 images. The ability to track large scale budgets of FF emissions over longer time periods likely relies on complementary observations of FF emission tracers which may help filter such a low signal from the signal from biogenic fluxes which is generally much larger over long distances. Ground-based networks could support such a tracking along with strengthening the constraint on the FF CO_2 emission estimates during the few hours before the satellite overpass. By starting the inversion window 12 hours before the satellite overpass (at 12:00 in our experiments), and 10 hours before surface measurements can be properly assimilated, we account for such an extension of the window of direct constraint on the FF CO_2 emission estimates from the satellite. The inversion window also ends more than six hours after the last ground-based measurement is assimilated. This time window is wider than the one chosen in Broquet et al (2018) or Santaren et al. (2020).

However, by limiting the inversion window to a single day, we avoid analysing to which extent the temporal correlations of the uncertainties in the FF CO_2 emission inventories allow for cross-referencing the information from data during different days. This assessment should rely on a strong knowledge on the structures of uncertainties in the FF emissions, which is still missing even though efforts have been conducted to improve it in CHE (WP3 and WP4) and other projects (Wang et al. 2020; Super et al. 2020). The 1-day inversion window also imposes the assimilation of daily samples of $^{14}CO_2$. However, the assumption that $^{14}CO_2$ could be sampled every day is currently difficult to envisage due to the corresponding measurement cost, and is thus optimistic (Wang 2016).

Inversions with the CO-CO_2 configuration are conducted for 2 different days: one in January (when the CO_2 biogenic fluxes are very low), the other one in May (when the CO_2 biogenic fluxes are relatively high). Inversions with the $^{14}CO_2$-CO_2 configuration are conducted for one day only (in July, when the biogenic fluxes are relatively high). This restriction is due to the

computation cost associated with the preparation of each day of analytical inversion, and to the specific schedule of the project.

2.2 Inversion configurations

This section summarizes the description of the two inversion configurations detailed in the D3.4 CHE report “Inversion strategy based on OSSEs”. The inversion systems rely on:

- A regional atmospheric transport model for Western Europe which corresponds to a zoomed configuration of the CHIMERE mesoscale chemistry-transport model (Menut et al. 2013) with 2-km resolution in the centre (see Figure 2-1). Our simulation and inversion periods correspond to two days for the CO-CO_2 configuration, one in winter (January 5 2015), the other one in spring (May 11 2015), and 1 day in summer (July 1 2015) for $^{14}CO_2$-CO_2 configuration.

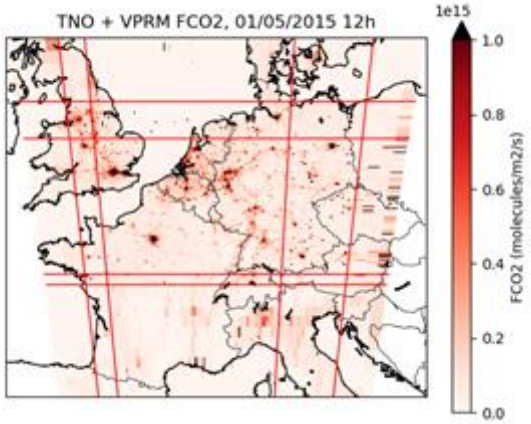

Figure 2-1: CO_2 flux map (based on values from the TNO inventory and VPRM simulations for 01/05/2015 at 12:00) over the atmospheric transport modelling grid. The red lines delimit the spatial resolution changes within the domain (from 2 km to 10 km and then 50 km from middle to edges of the domain).

- Analytical inversion frameworks (Wu et al., 2016) in which budgets of surface anthropogenic and natural fluxes or auxiliary parameters are controlled at plant, city or regional scales, and at hourly to daily resolution. In the following, the “control” parameters mainly correspond to flux budgets.

- Maps of all types of surface CO_2, CO and $^{14}CO_2$ fluxes (at temporal resolution up to 1 hour) provided within the project by TNO and CEA, whose plant or city to regional areas are re-scaled by the inversion using daily to hourly scaling factors to better fit the observations (Figures 2-2 and 2-3).

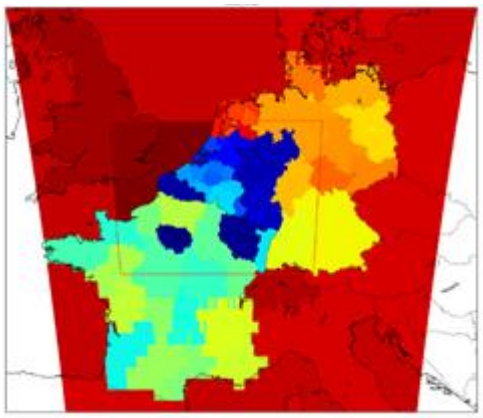

Figure 2-2: Administrative regions and coarser areas for which the biogenic flux budgets and the anthropogenic emission budget, are controlled in the $^{14}CO_2$-CO_2 inversion configuration. The red line delimits the 2 km × 2 km-resolution zoom of the CHIMERE transport model.

Figure 2-3: Controlled areas in the CO-CO_2 inversion configuration: nine Belgium administrative regions and the rest of the domain.

The inversion tests correspond to experiments with synthetic data (such as in Observing System Simulation Experiments, OSSEs). We provide observation location, time and corresponding observation uncertainties to the system. However, our analysis relies on the Bayesian framework of the inversions, updating a prior information on the control variables, and on the direct computations of uncertainties in the estimates of the control variables by the analytical systems. Therefore, we do not have to generate values for the synthetic data, and to conduct Monte Carlo experiments to derive the statistics of uncertainties. We analyse the uncertainties in inverted ("posterior") control parameters as a function of the observation system that is used for the inversion, and the corresponding uncertainty reduction, i.e., the relative difference between the posterior uncertainties and the prior uncertainties (expressed in terms of standard deviations) in the control variables:

$$UR = 1 - \frac{\sigma_{post}}{\sigma_{prior}}$$

The basics of the Bayesian inversion theoretical framework have been reminded in the D4.3 CHE report "Attribution Problem Configurations". The principles, theoretical framework and many parameters of the inversion configurations used here are very close to that used by Santaren et al. (2020) to study the potential of XCO_2 imagery for the monitoring of CO_2 anthropogenic emissions at the regional, city and plant scale. However, in practice, since the inversions here handle the co-assimilation of surface CO, $^{14}CO_2$ and CO_2 data, and since they are based on input products from the CHE projects, they rely on different configurations of the transport model and the analytical inversion. Further detail on the inversion concepts and principles relevant for our experiments co-assimilating CO_2 and $^{14}CO_2$ data can be found in Wang (2016).

Note that the CO-CO_2 configuration, as described in D3.4, does not assume perfect knowledge of the CO:CO_2 emission ratio: an optimistic correlation of 0.8 is assigned between prior uncertainties in CO and CO_2 anthropogenic FF or BF emissions in each sector of activity.

An important input of the experiments here is the simulation of CO_2M XCO_2 samplings over the area of interest generated by IUP-UB in the framework of the ESA PMIF project (Wang et al., 2020, Lespinas et al. 2020).

The following table lists the different experiments analysed afterwards.

Table 2.1: List of OSSE Experiments

Assimilated observations	Europe: $^{14}CO_2$-CO_2 inversion configuration on 1st of July 2015	Belgium: CO-CO_2 inversion configuration on 5th of January 2015 or on 11th of May 2015
Satellite XCO_2	EUR-Sat	BE-Sat
Surface CO_2	EUR-CO_2	BE-CO_2
Satellite XCO_2 + Surface CO_2	EUR-Sat-CO_2	BE-Sat-CO_2
Surface $^{14}CO_2$	EUR-$^{14}CO_2$	no
Satellite XCO_2 + Surface $^{14}CO_2$	EUR-Sat-$^{14}CO_2$	no
Satellite XCO_2 + Surface CO_2 and $^{14}CO_2$	EUR-Sat-CO_2-$^{14}CO_2$	no
Surface CO	no	BE-CO
Satellite XCO_2 + Surface CO_2 and CO	no	BE-Sat-CO_2-CO

Some sensitivity tests are also conducted by setting the prior uncertainties in NEE and BF fluxes to 0 (i.e. ignoring these fluxes) but we do not explicitly label them.

2.3 Results

2.3.1 Potential of the satellite observations as a standalone observation system

This section describes results when assimilating the data from the satellite track only. It focuses on the results from the corresponding EUR-Sat inversion with the high dimensional $^{14}CO_2$-CO_2 inversion configuration since this configuration provides a more extensive view of the results when using satellite data.

The uncertainty reductions for the 24-hour regional budgets of FF emissions (regional budgets aggregates emissions from urban areas, point source and the rest of the regions hereafter) range from 0 to 34% in the main area of interest (Figure 2.4). They are nearly null for regions

outside the ground coverage of the satellite. The northeast direction of the wind on the day of analysis is nearly aligned with the satellite track, which tends to confirm that the observation footprint does not extend out of this coverage. However, the relatively large wind speeds over Western Germany (~5-6 ms^{-1} near the surface) allows for significant uncertainty reduction (~19%) in the region of Essen which is not in this coverage. The uncertainty reductions rise to a range from 0 to 66% for the regional morning budget (Figure 2-4 and Table 2-2), i.e. when focusing better on the temporal footprint of the satellite observation. Larger emission budgets generally lead to larger uncertainty reductions. However, for similar emission budgets, uncertainty reductions are significantly higher for emissions from urban areas and cities than for the other regional emissions since dense emissions areas generate atmospheric signatures that are easier to detect and filter (because of their larger amplitude) than more extended but more diffuse emissions areas (Santaren et al., 2020).

Uncertainty reductions for the afternoon emissions entirely rely on the specification of 3-h temporal auto-correlation in the prior uncertainties in the emissions since these afternoon emissions are not directly seen by the satellite. Consequently, they are low for all types of sources. Figure 2-4 and Table 2-2 show uncertainty reductions for afternoon regional budgets ranging from 0 to 6%.

Overall, the results show contrasted skills for the monitoring of the FF emissions. The lack of constraint outside the satellite coverage and during periods other than the morning confirms the need for complementary data to extrapolate in space and time the information from the satellite. The scores of uncertainty reductions result in various levels of precision on the emission estimates, with 6.5% to 30% posterior uncertainties in regional budgets for 24-h budgets in the main area of interest.

UR EUR-Sat	a 24-h Budget	b Morning Budget	c Afternoon Budget
FF	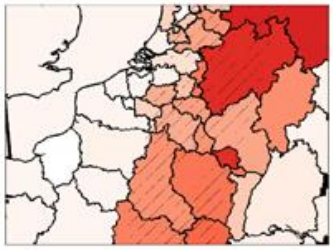	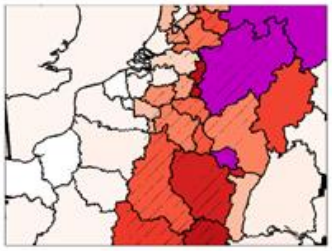	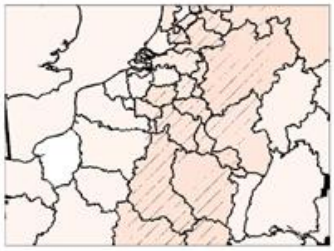
BF	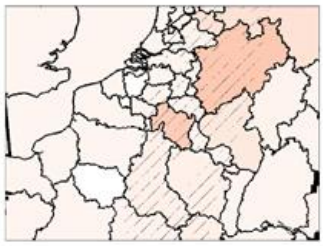	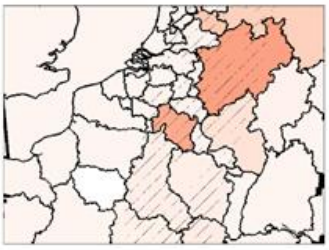	
FF + BF	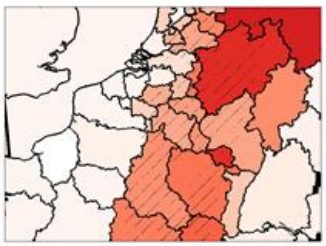	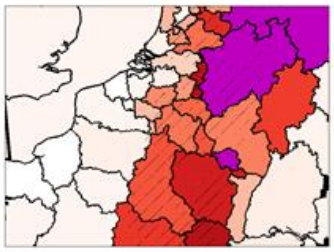	
NEE	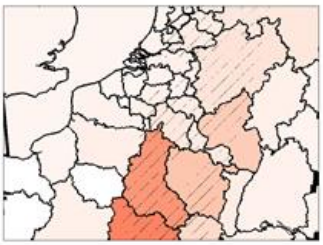	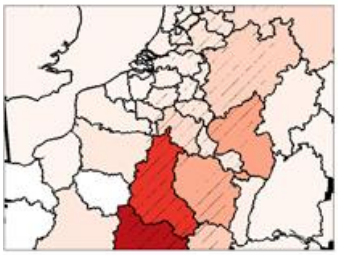	
			

Figure 2-4: Uncertainty reduction in EUR-Sat inversion: for 24-h (a), morning (b) or afternoon (c) budgets of FF, BF, anth. emissions (FF+BF) and biogenic fluxes (NEE). Stripes indicate the satellite coverage.

	Uncertainty reductions on FF budget %	24-hour	Morning	Afternoon
EUR-Sat	mean	10.9	17.6	2.8
	max	33.7	65.9	5.8

Table 2-2: Statistics of the uncertainty reductions in EUR-Sat for regional 24-h, morning and afternoon FF emission budgets in the main area of interest (these budgets combine emissions from urban areas, large plants and the more diffuse regional sources).

The UR for Net Ecosystem Exchange (NEE) and biofuel emissions (BF) is generally much smaller than for the FF emissions (Figure 2-4). The much weaker level of emissions related to BF combustion easily explains the lack of UR for this type of fluxes. However, the NEE is relatively large in July and the weaker UR for NEE can be explained by its diffuse nature compared to FF emissions.

The problem of the attribution of inferred fluxes to FF emissions, NEE or BF emissions is investigated by conducting sensitivity tests in which the NEE or BF emissions are ignored (setting the prior uncertainty in NEE and/or BF emissions to 0).

The EUR-Sat experiment with prior uncertainties in the NEE set to 0 (Figure 2-5 and Table 2-3) shows significantly larger UR for the regional budgets of morning FF emissions with a range from 0 to 75% in the satellite coverage. However, this increase of the UR is moderate and still yields posterior uncertainties in 24-h regional budgets ranging from 6% to 30% in the satellite coverage. The differences in terms of spatial distribution between the NEE and the FF emissions explains the moderate impact of uncertainty in NEE in the UR for FF emissions.

Setting prior uncertainties in BF emissions to 0 has a very weak impact on the UR for FF emissions (Figure 2-5) even though the spatial distribution of these two types of emissions are strongly correlated. This weak impact is directly attributed to the weak amplitude of BF emissions compared to FF emissions: the posterior uncertainties in FF emissions (6 to 30 % of the 24-h BF + FF emission budget) remain much larger than the uncertainty in BF emissions (0 to 7% of the 24-h BF + FF emission budget).

	UR on 24-hour budgets of FF emissions
No BF	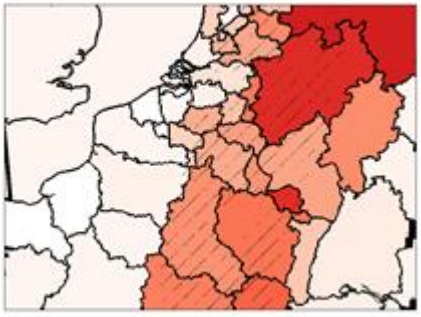
No NEE	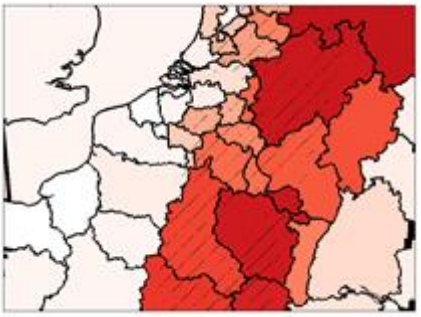
No BF No NEE	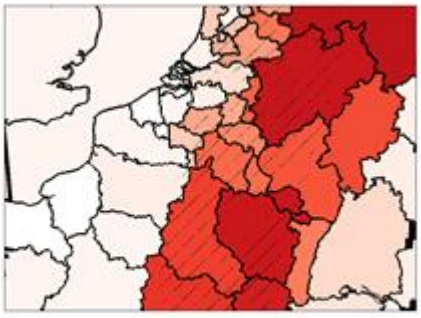

Figure 2-5: Uncertainty reduction in EUR-Sat inversion where the prior uncertainty in NEE or/and BF is set to zero, for 24-h budgets of FF emissions. Stripes indicate the satellite coverage.

EUR-Sat NEE set to 0	Uncertainty reductions on FF budget %	24-h	Morning	Afternoon
Main area of interest	mean	13.7	22.4	3.0
	max	37.5	74.6	5.8
Satellite coverage	mean	17.2	27.5	3.2
	max	38.9	74.6	5.8

Table 2-3: Statistics of the uncertainty reductions in EUR-Sat inversion where the prior uncertainty in NEE is set to zero, for regional 24-h, morning and afternoon FF emission budgets. In the main area of interest, these budgets combine emissions from urban areas, large plants and the more diffuse regional sources.

2.3.2 Assessing the complementarity with the ground-based CO_2 network

This section evaluates the impact of (co-)assimilating data from the ground-based CO_2 network and the potential complementarities between the satellite and CO_2 ground-based observations focusing on inversions with the high dimensional $^{14}CO_2$-CO_2 inversion configuration: we analyse experiments EUR-CO_2 and EUR-Sat-CO_2, and comparisons with the results from EUR-Sat.

2.3.2.1 General results for the FF emissions

EUR-CO_2 reveals, again, the limited role of the horizontal atmospheric transport to propagate UR from regions where we have several measurement stations to the other ones. UR of more than 15% for 24-h budgets can be achieved in regions with 3 stations in the main area of interest (like Île-de-France 16.7%, and North Rhine-Westphalia 17.2%), or in regions with more stations outside this area (like southeast England and Baden-Württemberg, 31% which have 5 stations). However, UR can also be much lower in regions with many stations, e.g. for Lower-Saxony-and-Bremen which has 5 stations but a 6% UR. UR in regions with 1 or 2 stations range between 1% and 10%. The UR are generally below 1% for other regions (Figure 2-6 and Table 2-4).

Of note is that the highest UR in the whole inversion domain (40% for 24-hour budgets and 47% for morning budgets) correspond to large regions of the coarse resolution area of the transport model (not represented in Figure 2-6). This result is primarily driven by the optimistic extrapolation of information from the sites to the coarse model grid cells and further to the whole extent of the control areas in which they stand. This optimistic bias from the inversion configuration actually results in representation and aggregation errors when working with real data (Kaminski et al. 2001; Wang et al. 2017). It justifies and supports the use of the finer resolution control vector in the main area of interest, and the focus of our analysis on the 2 km resolution model subdomain.

Only one region of the 2 km resolution model subdomain with 3 stations is located in the satellite coverage (the region North Rhine-Westphalia). When comparing the UR for the 24-h regional budgets of FF emissions from EUR-Sat-CO_2 to that from EUR-Sat (Figure 2-4 and Table 2-2), it appears that the only significant changes are

- ð the increase of UR for this region by 4 percentage point (34 to 38%), i.e. less than the UR for this region in EUR-CO2 (17%)

- ð the increase of UR for the regions outside the satellite coverage with more than 3 ground-based stations from nearly 0% to values that are nearly the same as in EUR-CO_2.

This indicates that the URs at 24-h scale in EUR-Sat-CO_2 are smaller than the addition of URs in EUR-Sat and EUR-CO_2 experiments.

UR on 24-h budgets	a EUR-CO_2	b EUR-Sat-CO_2
FF		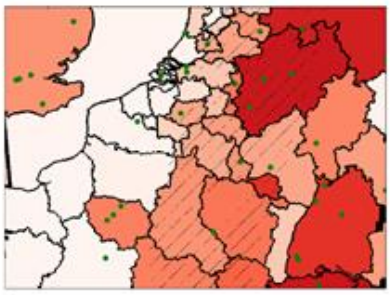
BF		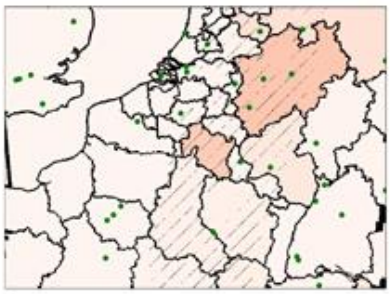
FF+ BF	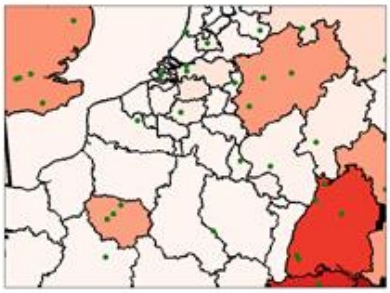	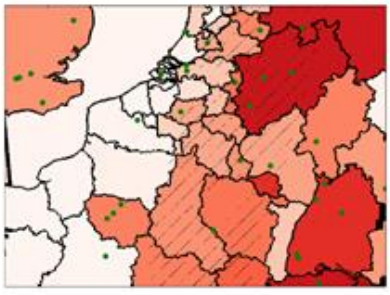
NEE		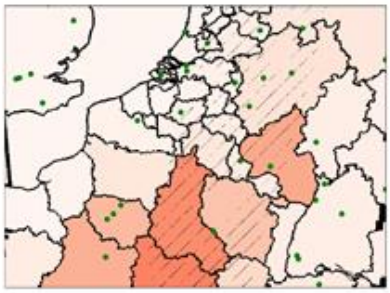
		

Figure 2-6: Uncertainty reduction in EUR-CO_2 (a) and EUR-Sat-CO_2 (b) inversions: for 24-h budgets of FF, BF, anth (FF+BF) emissions and biogenic fluxes (NEE). Stripes indicate the satellite coverage. Green dots indicate the ground stations.

		Uncertainty reductions on FF budget %	24-h	Morning	Afternoon
EUR-CO_2	Main area of interest	mean	2.5	2.9	1.9
		max	17.2	22.5	23.2
EUR-Sat-CO_2	Satellite coverage	mean	16.5	24.0	6.1
		max	40.0	67.0	29.7
	Main area of interest	mean	12.8	19.5	4.7
		max	37.8	67.0	25.5

Table 2-4: Statistics of the uncertainty reductions in EUR-CO_2 and EUR-Sat-CO_2 inversions, for regional 24-hour, morning and afternoon FF emission budgets. In the main area of interest, these budgets combine emissions from urban areas, large plants and the more diffuse regional sources.

The ground-based CO_2 data constrain both afternoon and morning emission estimates, with UR of 6 to 38% and of 3 to 29% respectively for morning and afternoon regional budgets of FF emissions in the regions with 3 or more stations (Figure 2-7 8). The comparison between results for afternoon budgets of the FF emissions from EUR-Sat-CO_2 and EUR-Sat shows, again, in EUR-Sat-CO_2, an increased UR that is smaller than the sum of the URs obtained in EUR-Sat and EUR-CO_2. Crossing the satellite data with the afternoon data from the ground network does not increase the ability to extrapolate the spatially widely spread information from these satellite data to the afternoon.

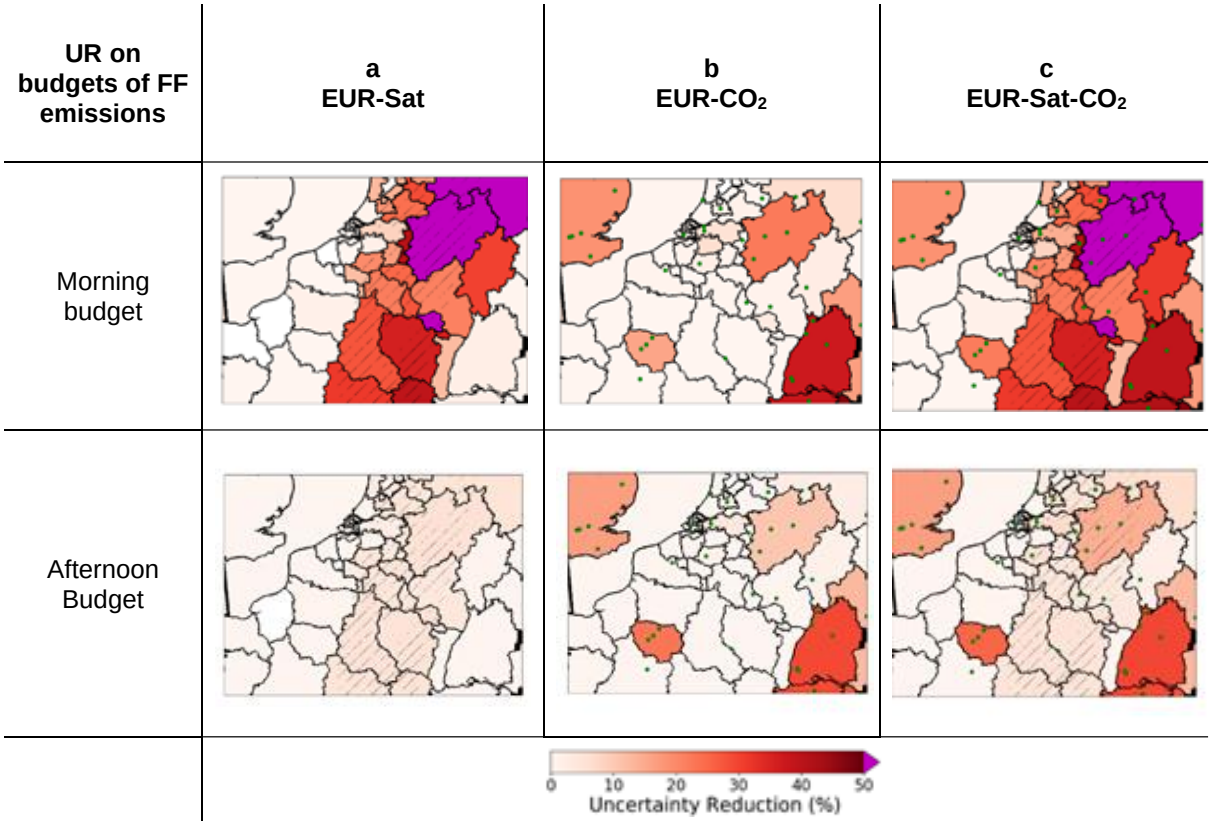

Figure 2.7: Uncertainty reductions in EUR-Sat (a), EUR-CO_2 (b) and EUR-Sat-CO_2 (c) inversions: for morning (upper panel) and afternoon (lower panel) budgets of FF emission. Stripes indicate the satellite coverage. Green dots indicate the ground stations.

2.3.2.2 Impact of NEE and BF emissions

EUR-CO_2 and the results of EUR-Sat-CO_2 outside the coverage of the satellite show different situations regarding the comparison between UR for NEE and FF emissions (Figure 2-6). In regions with large cities and industrial plants (like the Paris area and Baden-Württemberg), the URs for NEE are smaller than that for FF as in EUR-Sat. However, in other regions, the signal at the surface stations is dominated by the signature of the natural fluxes and URs for NEE are larger than that for FF emissions. Due to the relatively weak signal from BF emissions, the UR for these emissions are much smaller than that for FF emissions (close to 0%) in EUR-CO_2.

The impact of the attribution problem when using the surface CO_2 network is quantified, here again, by conducting sensitivity tests in which the prior uncertainty in NEE and/or BF emissions is set to 0 (Figure 2-8 and Table 2-5). The surface network having many stations mostly sensitive to the NEE signal, it is expected to support the distinction between NEE and FF emissions in the inversion, even if the stations measure CO_2 only.

In inversions EUR-CO_2, the UR for FF emissions in the regions with more than 3 stations are higher when ignoring the NEE and BF emissions, reaching a range between 12 and 43% for 24-h budgets. The impact of ignoring these fluxes for these regions is higher than for regions

in the satellite coverage in EUR-Sat. However, the impact is negligible for the other regions for which the UR keeps on being very low.

The comparison between results from EUR-Sat-CO_2 and EUR-Sat when ignoring these fluxes hardly demonstrates a potential of the surface CO_2 network to reduce the problem of attribution between FF emissions and other fluxes. Adding the CO_2 network when ignoring the NEE and BF emissions yields a larger increase of the UR than when accounting for NEE and BF emissions. This is linked to the smaller UR associated with CO_2 data when accounting for NEE and BF and to the lack of indirect feedback on the UR for FF emissions of the lowering of uncertainties in NEE when complementing the satellite data with CO_2 data.

UR on 24-h budgets of FF emissions	a EUR-CO_2	b EUR-Sat-CO_2
No BF		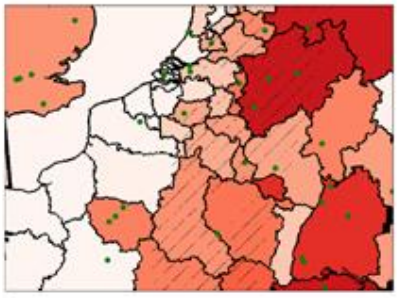
No NEE	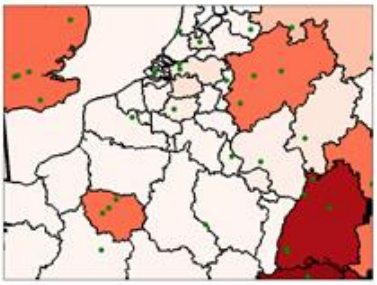	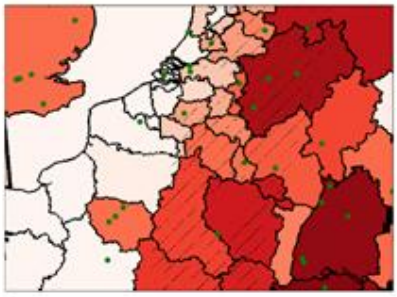
No BF No NEE	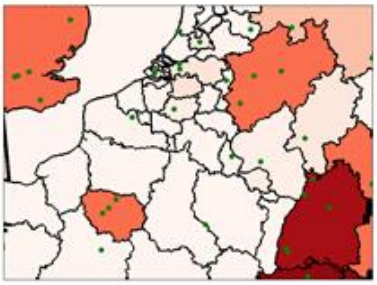	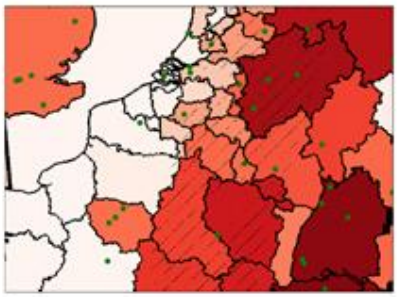
		

Figure 2-8: Uncertainty reduction in EUR-CO_2 (a) and EUR-Sat-CO_2 (b) inversions, where the prior uncertainty in NEE or/and BF is set to zero: for 24-h budgets of FF emissions. Stripes indicate the satellite coverage. Green dots indicate the ground stations.

NEE set to 0		Uncertainty reductions on FF budget %	24-h	Morning	Afternoon
EUR-CO_2	Main area of interest	mean	3.3	4.0	2.3
		max	24.3	30.9	27.4
EUR-Sat-CO_2	Main area of interest	mean	15.8	24.6	5.0
		max	43.0	76.2	27.4

Table 2-5: Statistics of the uncertainty reductions in EUR-CO_2 and EUR-Sat-CO_2 inversions, where the prior uncertainty in NEE is set to zero, for regional 24-h, morning and afternoon FF emission budgets. In the main area of interest, these budgets combine emissions from urban areas, large plants and the more diffuse regional sources.

2.3.3 Assessing the complementarity with the ground-based CO and $^{14}CO_2$ networks

This section evaluates the impact of (co-)assimilating data from ground-based CO and $^{14}CO_2$ networks and the potential complementarities between the satellite and CO_2, CO and/or $^{14}CO_2$ ground-based observations analysing both EUR (with conditions of the 1st of July 2015) and BE inversions (with conditions of the 5th of January 2015 and 11th of May 2015). In these cases, we analyze and compare experiments assimilating the CO or $^{14}CO_2$ data only, and some couples of experiments with similar networks in which one experiment in a couple assimilates the CO or $^{14}CO_2$ data while the other does not.

2.3.3.1 Impact of surface CO network

Results from BE-CO, the comparison between BE-CO and BE-CO_2 (BE-CO not shown), and the comparison between BE-Sat-CO and BE-Sat or BE-Sat-CO_2-CO and BE-Sat-CO reveal a very low UR provided by the surface CO network on the regional estimates of FF CO_2 emissions (Figure 2-9 and Table 2-6). This applies to tests in both winter and spring (only spring is shown here for illustration, note that the uncertainty on NEE drives the inversion assimilating CO_2 data). The UR for afternoon and regional budgets of CO FF emissions can be high (e.g. 20% on Limburg budget, not shown) when using the surface CO network only. However, even though the strong correlation between prior uncertainties FF CO_2 and FF CO should propagate corrections from FF CO emissions to FF CO_2 emissions, this propagation is highly uncertain and does not significantly lower the uncertainty in FF CO_2 emissions. These results imply a lack of support from the CO surface data to the “attribution problem”.

	Uncertainty reductions on FF budget %	24-h	Morning	Afternoon
BE-Sat-winter	min	1.5	2.7	0.2
	max	11.6	20.9	2.2
BE-Sat-spring	min	0.7	1.1	0.1
	max	3.3	5.0	1.1
BE-Sat-CO_2-winter	min	1.6	2.7	0.3
	max	20.6	30.2	13.3
BE-Sat-CO_2-spring	min	0.7	1.2	0.1
	max	7.2	10.3	3.0
BE-Sat-CO_2-CO-winter	min	1.6	2.7	0.3
	max	20.7	30.3	13.5
BE-Sat-CO_2-CO-spring	min	0.7	1.2	0.1
	max	7.7	11.0	3.3

Table 2-6: Statistics of the uncertainty reductions in BE-Sat, BE-Sat-CO_2 and BE-Sat-CO_2-CO inversions, in winter and spring, for regional 24-hour, morning and afternoon CO_2 FF emission budgets.

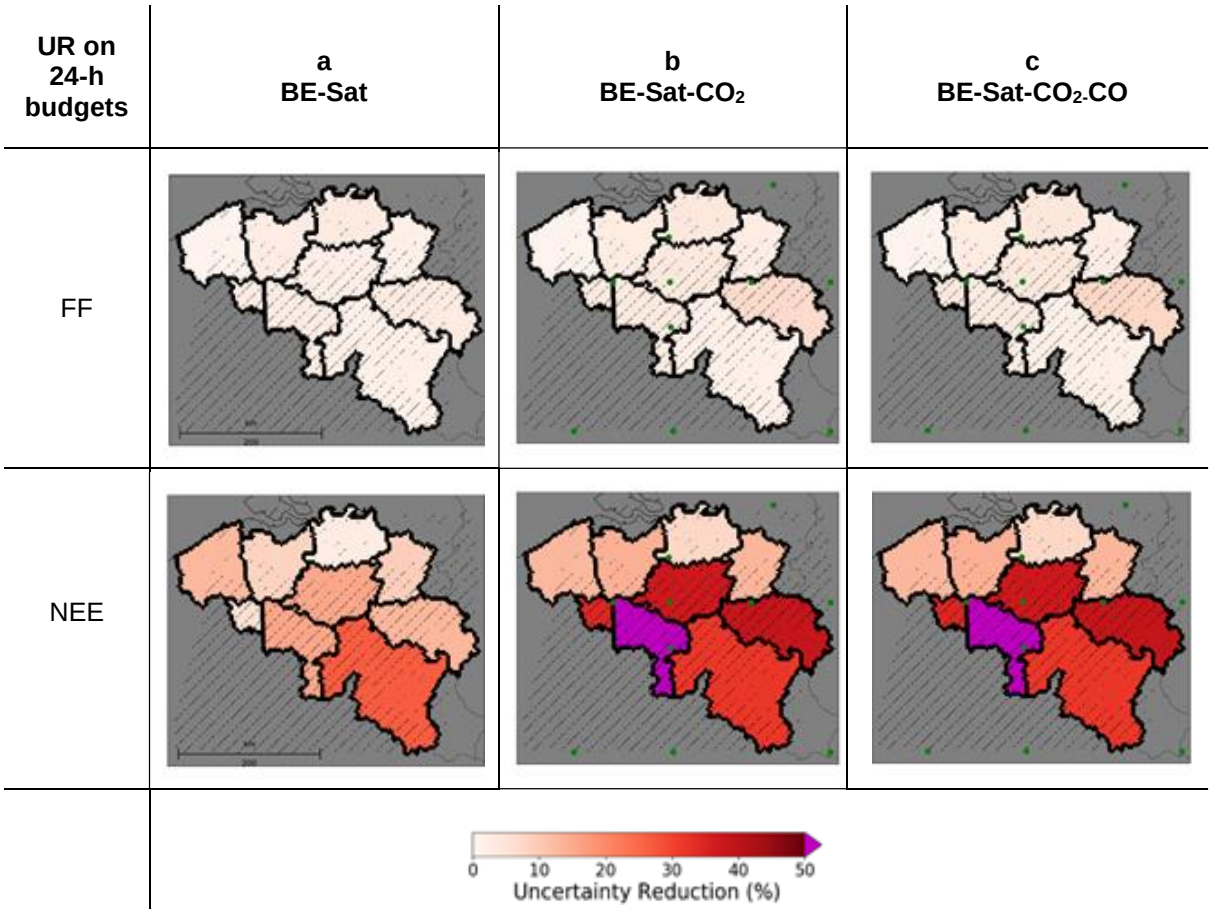

Figure 2-9: Uncertainty reduction in BE-Sat (a), BE-Sat-CO_2 (b) and BE-Sat-CO_2-CO (c) inversions in Spring: for 24-h budgets of CO_2 FF emissions and biogenic fluxes (NEE). Stripes indicate the satellite coverage. Green dots indicate the ground stations.

2.3.3.2 Impact of the surface $^{14}CO_2$ network

The spatial distribution of the regional UR for 24-h, morning or afternoon budget when using surface $^{14}CO_2$ data alone is similar to that when using CO_2 surface data only. These URs are very low for regions with less than 2 stations (<5%) and range between 8 to 31% (morning budget) and 2 to 16% (afternoon budget) for regions with more than 3 sites (Figure 2-10 and Table 2-7). The URs are only slightly larger (and sometimes smaller) in EUR-$^{14}CO_2$ (Table 2-7), i.e. when using the sampling of $^{14}CO_2$ representative of 7-h averages of the concentrations, than in EUR-CO_2, when using 7 hourly CO_2 data at each site. The higher potential of $^{14}CO_2$ data than CO_2 data to filter signal from FF emissions (if both were measured at the same temporal resolution) is balanced by the finer temporal resolution of the CO_2 continuous measurements (since $^{14}CO_2$ has to be sampled with a relatively low frequency), which helps catching the high frequency patterns of the signal from FF emissions.

The result of URs when combining two networks smaller than the sum of URs when using each of these networks shown when comparing EUR-Sat, EUR-CO_2 and EUR-Sat-CO_2 also applies when adding the surface $^{14}CO_2$ network i.e. i.e. when comparing e.g. EUR-Sat-$^{14}CO_2$ to EUR-Sat and EUR-$^{14}CO_2$ or EUR-Sat-CO_2-$^{14}CO_2$ to EUR-Sat-CO_2 and EUR-$^{14}CO_2$. The combination of $^{14}CO_2$ data with other types of data does not lead to further synergies of the advantages for each network: the spatial extent of the satellite observation, the temporal

coverage of the ground-based networks, the temporal resolution of the CO_2 surface network, and the higher sensitivity to FF emissions of the $^{14}CO_2$ network.

The comparison of the experiments EUR-$^{14}CO_2$ with and without NEE and BF emissions shows a much smaller impact of these fluxes on the UR for FF emissions than in experiments EUR-CO_2 or EUR-Sat, which confirms the much smaller sensitivity of $^{14}CO_2$ data to NEE than CO_2 data. An interesting consequence is that the increase of UR from EUR-Sat to EUR-Sat-$^{14}CO_2$ or from EUR-Sat-CO_2 to EUR-Sat-CO_2-$^{14}CO_2$ is slightly larger when accounting for the NEE and the BF emissions than when ignoring them (Figure 2-11 and Table 2-8). In other words, the potential of the $^{14}CO_2$ network to complement the satellite observation is higher when NEE is accounted for, while section 3.3.1 showed the opposite for the surface CO_2 network. This increase of the impact of the $^{14}CO_2$ network when accounting for NEE is however relatively small, reaching its maximum in the region North Rhine-Westphalia, which has 3 stations, and where the increase of UR for the 24-h regional budgets of FF emissions from EUR-Sat to EUR-Sat-$^{14}CO_2$ is of 3 percentage point (from 34 to 37%) when accounting for the NEE. In a general way, it is difficult to demonstrate a potential of the surface $^{14}CO_2$ network to reduce the problem of attribution between FF emissions and other fluxes as for the surface CO_2 network.

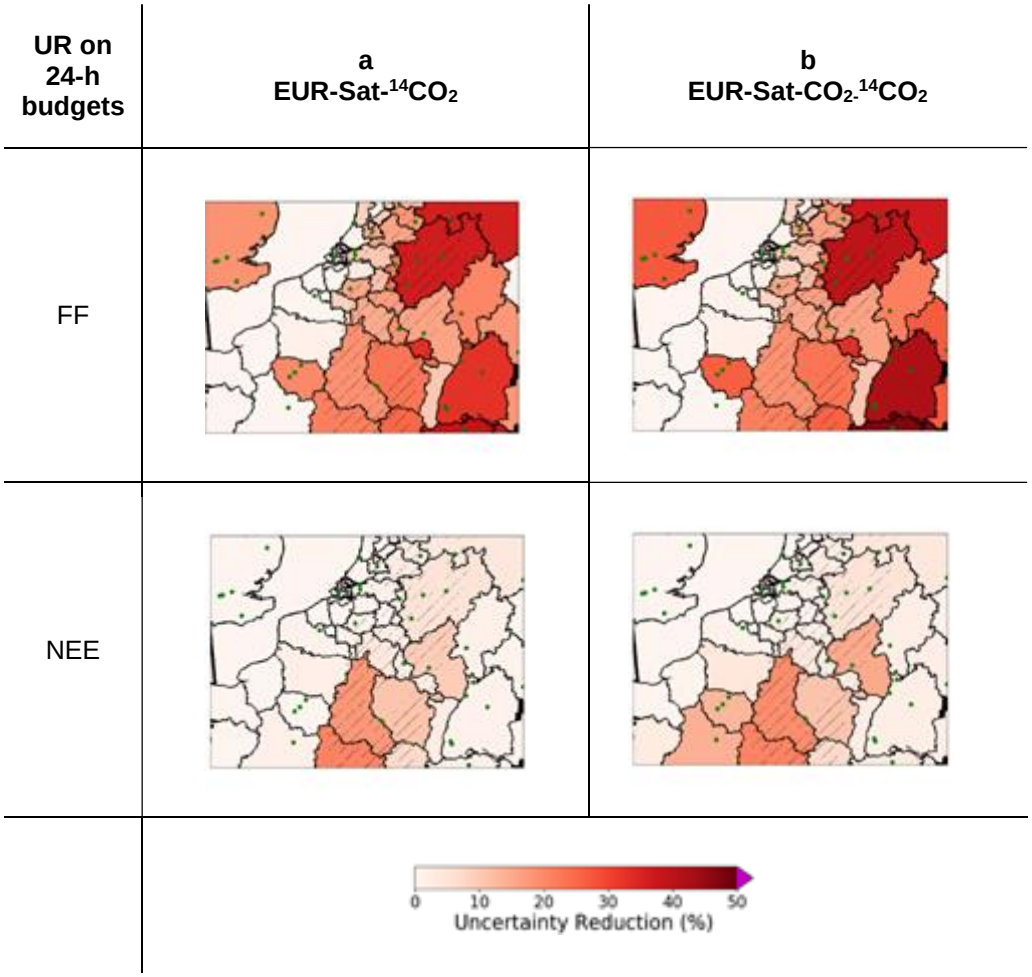

Figure 2-10: Uncertainty reduction in EUR-Sat-$^{14}CO_2$ (a) and EUR-Sat-CO_2-$^{14}CO_2$ (b) inversions: for 24-h budgets of FF emissions and biogenic fluxes (NEE). Stripes indicate the satellite coverage. Green dots indicate the ground stations.

		Uncertainty reductions on FF budget %	24-h	Morning	Afternoon
EUR- $^{14}CO_2$	Main area of interest	mean	2.4	2.6	1.2
		max	20.0	25.1	15.5
EUR-Sat-$^{14}CO_2$	Main area of interest	mean	12.4		
		max	36.6		
EUR-Sat-CO_2-$^{14}CO_2$	Main area of interest	mean	13.3	20.0	5.0
		max	39.7	68.0	28.8
	satellite coverage	mean	17.7	25.2	6.6
		max	48.0	68.0	33.6

Table 2-7: Statistics of the uncertainty reductions in EUR-$^{14}CO_2$ and EUR-Sat-CO_2-$^{14}CO_2$ inversions, for regional 24-hour, morning and afternoon FF emission budgets. In the main area of interest, these budgets combine emissions from urban areas, large plants and the more diffuse regional sources.

UR on 24-h budgets of FF emissions	a EUR-Sat-$^{14}CO_2$	b EUR-Sat-CO_2-$^{14}CO_2$
no BF	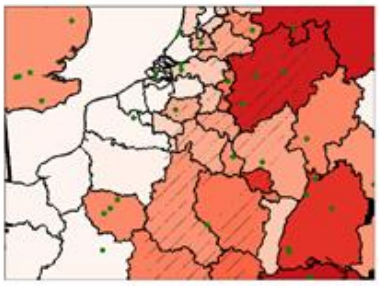	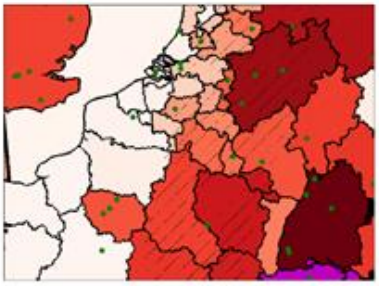
No NEE	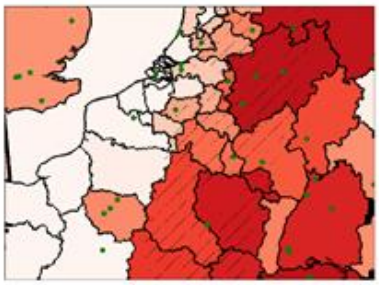	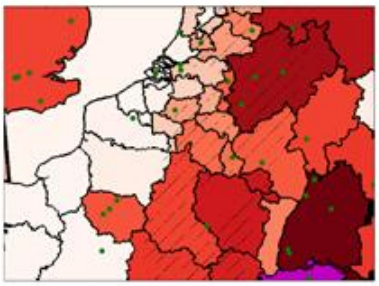
no BF no NEE	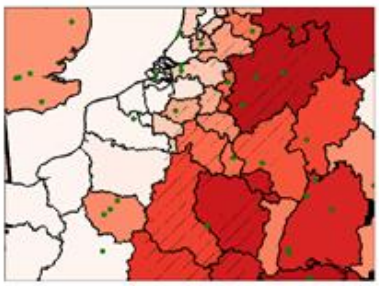	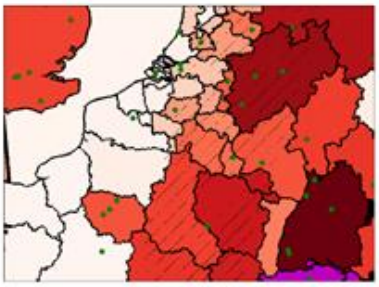
		

Figure 2-11: Uncertainty reduction in EUR-Sat-14CO2 (a) and EUR-Sat-CO_2-$^{14}CO_2$ (b) inversions, where the prior uncertainty in NEE or/and BF is set to zero: for 24-h budgets of FF emissions. Stripes indicate the satellite coverage. Green dots indicate the ground stations.

No NEE Main area of interest	Uncertainty reductions on FF budget %	24-h	Morning	Afternoon
EUR- $^{14}CO_2$	mean	2.4		
	max	20.1		
EUR-Sat-$^{14}CO_2$	mean	15.1		
	max	39.9		
EUR-Sat-CO_2-$^{14}CO_2$	mean	16.2	25.0	5.3
	max	44.0	76.6	30.0

Table 2-8: Statistics of the uncertainty reductions in EUR-Sat-$^{14}CO_2$ inversion where the prior uncertainty in NEE is set to zero, for regional 24-h, morning and afternoon FF emission budgets. In the main area of interest, these budgets combine emissions from urban areas, large plants and the more diffuse regional sources.

2.4 Conclusions

These results raise contrasted conclusions regarding the potential of the combination between the satellite observation and surface networks.

The satellite observation, as a stand-alone system, can yield estimates of the regional budgets of FF emissions in the morning corresponding to its days of overpass with precisions down to ~5% in its ground coverage. However, it does not provide direct information on emissions during the afternoon or during the night, and hardly provides information on plants, cities and regions outside its coverage. Furthermore, previous publications (Broquet et al., 2018, Wang et al., 2020, Lespinas et al. 2020, Kuhlman et al. 2020) have shown that even with a CO2M constellation of three or more satellites, the number of overpasses producing local images with low cloud cover is limited each year, which hampers the estimation of annual budgets or of anomalies in annual budgets (Chevallier et al., 2020). The need for complementary sources of information to derive daily to annual budgets is thus critical.

The “attribution problem” in itself appears to be nearly secondary compared to that of the observation precision but our results confirm that there is a significant impact of the uncertainties in the NEE for the estimate of FF emissions. The uncertainties in BF do not appear to have a large impact on the estimate of FF emissions but this is related to the fact that the posterior uncertainties in FF emissions remain larger than the prior uncertainties in BF emissions i.e. to the relatively low level of BF emissions compared to the typical uncertainties in FF emissions at regional to local scales. If willing to reach very high precision estimates of the FF emissions with higher precision spaceborne instruments, and if the share of BF emissions increases in the future, the uncertainties in BF emissions would probably become a major problem due to the strong correlation between the spatial distributions of FF

and BF emissions. The problem of attribution to NEE fluxes would also increase if targeting very high precision estimates of the FF emissions in the future.

Surface CO_2/$^{14}CO_2$ networks can help further decrease the uncertainty in the FF emissions estimates when combined with satellite observations. In North Rhine-Westphalia, the addition of CO_2 and $^{14}CO_2$ stations decreases the posterior uncertainty in daily regional emissions from 6.5% with the satellite alone to 5.9%. However, relatively dense networks close to highly emitting areas are needed to support such a decrease. The isolated rural stations do not provide a direct strong constraint for the estimate of the FF emissions, nor a significant indirect constraint for this estimate by solving for “the attribution problem”. Our results suggest that surface CO_2 and/or $^{14}CO_2$ measurements in support of the FF emission monitoring should be targeting FF emission areas directly rather than the surrounding NEE. Both hourly CO_2 and daily $^{14}CO_2$ data can provide useful information on the FF emissions, the former catching the signature of these emissions at high frequency and the latter being much less sensitive to the uncertainties in the NEE.

Overall, the results illustrate a decrease of the potential from each observation subsystem rather than an amplification of these potentials when combining them into a large observation system with satellite and surface data. This is the natural consequence of the asymptotic convergence of the precision of inversions towards low values when adding observations. The attribution problem and that of the temporal extrapolation of the results are not such in our experiments that the synergy between the spatial extent of the satellite observation, the temporal coverage of the ground-based networks, the temporal resolution of the CO_2 surface network, and the higher sensitivity to FF emissions of the $^{14}CO_2$ network allows for a wide spatio-temporal coverage of the FF emissions at high resolution. There is a lack of new extrapolation of information from the combination of observation subsystems.

The results also indicate the lack of potential in adding information from sparse CO surface networks to CO_2 satellite and surface observations for the inversion of FF CO_2 emissions, despite an optimistic assumption regarding the correlation between uncertainties in FF CO and FF CO_2 emissions, and even though we ignored the natural sources of CO in our tests. The level of independence between the FF CO and FF CO_2 emissions appears to be too high to reach finer precision in the FF CO_2 estimates when adding CO data compared to those reached with CO_2 data only, or even to those from state-of-the-art prior inventories.

Therefore, these results support the deployment of very dense CO_2/$^{14}CO_2$ surface networks to support the satellite observation, with at least 3 sites per European administrative regions. The large-scale deployment of such dense networks is probably unaffordable for the coming decade, but some regions are now equipped with many stations and in some locations, the complementarity between satellite and surface networks could thus be demonstrated. Frequent (up to daily) samplings of $^{14}CO_2$ would be needed to ensure $^{14}CO_2$ data can bring information on FF emissions more precise than that of hourly CO_2 stations.

Several warnings should be raised for the interpretation of these results and conclusions. Part of the lack of amplification of the impact from the different observation subsystems when combining them could be due to our set-up of the prior uncertainties in which we ignore spatial correlations and assume that the temporal correlations are relatively low. These assumptions are conservative and, we believe, safer, in a context where the correlations of uncertainties in current inventories are still poorly characterized and, since they are probably highly complex and far from isotropic, homogeneous, decreasing with distance or time. For instance, distant plants or cities can have more similar processes than close ones, and the emissions and their underlying processes can vary rapidly depending on the time, weather, or socio-economic drivers... Inversions assuming large temporal and spatial correlations in the prior uncertainties in inventories would indicate a stronger ability to extrapolate the information from atmospheric data but could be too optimistic.

Furthermore, our study tested surface networks roughly corresponding to the extension of a continental network like ICOS for the monitoring of regional FF emission budgets. The deployment of networks dedicated to specific cities with stations around and within the urban areas (Wu et al. 2016) would correspond to a different strategy and could result in different conclusions for the monitoring of city emissions. CO data might play a stronger role in such urban networks, and the complementarity between satellite and surface data might be better highlighted at city scale. However, the advantage of this strategy locally would be balanced by the lack of constraint on larger scale budget of the FF emissions and would favour the monitoring of large cities with some capabilities to equip local networks.

Finally, our modelling of the errors from the atmospheric transport model is relatively simple here. This uncertainty is summarized into a Gaussian noise without any spatial and temporal correlations, as traditionally done in atmospheric inversions (Santaren et al., 2020). Complex modelling errors could actually shift or modify the patterns of the atmospheric signature of the FF emissions, which could increase the weight of the attribution problem, and thus the potential of the combination between satellite and surface data. However, very dense surface networks would be needed to support the identification and adjustment of transport errors.

3 Assessment from EMPA

Empa performed simulations with the Eulerian atmospheric transport model COSMO-GHG, which is an extended version of the regional numerical weather prediction model COSMO for the simulation of greenhouse gases (GHGs). Empa simulated the tracers CO_2, CO and ^{14}C but not APO. In order to attribute variations in these compounds to different sources and regions, each compound was simulated as a superposition of multiple tagged tracers representing specific combinations of source process (e.g. fossil fuel versus biofuel, anthropogenic versus natural fluxes) and geographical region. To keep the total number of tracers in a computationally manageable range, only a coarse spatial division into large European subregions was possible.

3.1 Simulation setup

3.1.1 Domain

Forward simulations were conducted for a domain covering Europe. Since COSMO-GHG operates on rotated-pole coordinates, the domain covers a slightly smaller area compared to the domain covered by MPG's simulations. The grid spacing over the whole domain approximates to 5.5 km. All grid parameters are listed in Table 3-1.

Table 3-1: Parameters of the COSMO-GHG European domain

Parameter	Longitudinal direction	Latitudinal direction
Rotated north pole coordinates	-170.00°	43.00°
Rotated start coordinates	-17.00°	-11.00°
Rotated end coordinates	20.95°	19.45°
Geographical start coordinates	-26.58°	32.71°
Geographical end coordinates	53.36°	66.45°
Grid spacing	0.05°	0.05°
Number of grid cells	760	610

3.1.2 Tracers

The trace compounds considered in the simulations of EMPA are CO_2, $^{14}CO_2$ and CO. The simulation of APO had to be discarded due to the limited resources in this project and the extensive data pre-processing for the other tracers. Europe was divided along country borders into six large regions representing Central, Northern, Western, Southern, South-eastern and Eastern European countries, as shown in Figure 3-1.

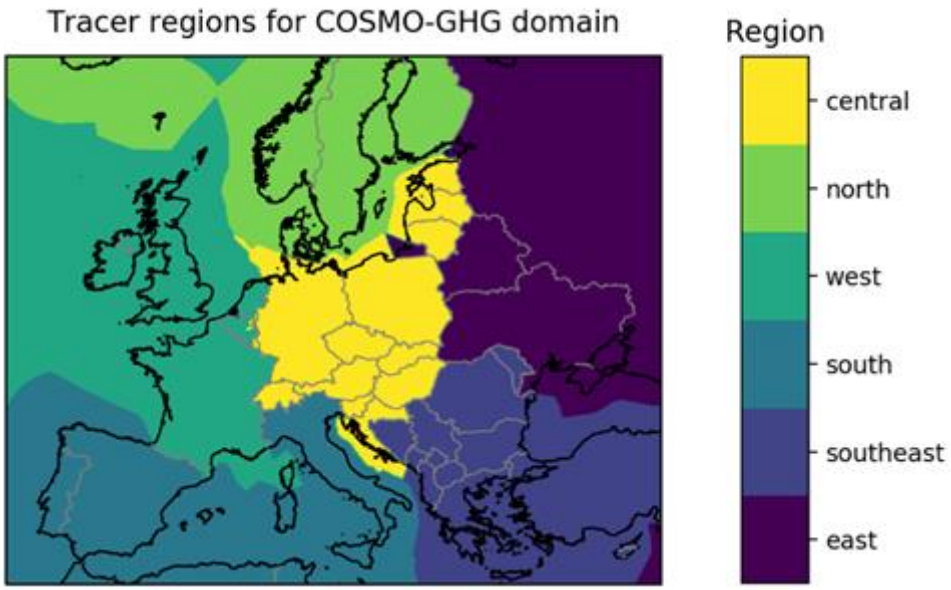

Figure 3-1: European regions for anthropogenic and biosphere tracers in COSMO-GHG.

For every tagged tracer a corresponding flux field was pre-processed and stored into hourly input files for the transport model. Table 3-2 lists all 75 tracers, including their underlying source processes and the number of tracers used for the regional split. No regional split was applied to the ocean tracers. For all three compounds an additional background tracer was simulated, which is constrained at the lateral boundaries by the output of a global model and transported passively throughout the model domain. For CO_2, CO and ^{14}C, not only a division into different anthropogenic source categories was applied, but also into contributions from biospheric fluxes due to photosynthetic uptake and respiration.

Table 3-2: Processes for CO_2, $^{14}CO_2$ and CO sources/sinks and their corresponding tracer names in COSMO-GHG.

Origin	Process	Tracer names	Region split	Number of tracers
Anthropogenic	Fossil fuels[1]	CO2_FF CO_FF	Yes	6 6
	Biofuels	CO2_BF C14_BF CO_BF	Yes	6 6 6
	Nuclear power plants	C14_NUC	Yes	6
Biosphere	GPP/NPP	CO2_GPP C14_NPP C14_NPN	Yes	6 6 6

	Respiration	CO2_RA C14_HR	Yes	6 6
Ocean	Sources (positive flux: "_P") and sinks (negative flux: "_N")	CO2_O_P CO2_O_N CO_O_P CO_O_N C14_O_P C14_O_N	No	1 1 1 1 1 1
IC/BC	Background concentration from outside of domain	CO2_BG C14_BG CO_BG	No	1 1 1
			SUM	**75**

[1] No C14_FF tracer is needed since $\delta^{14}CO_2$ = -1000 ‰ for those processes and the corresponding CO_2_FF-tracers can be used for the computation.

3.2 Results

3.2.1 Time periods and meteorological situation

COSMO-GHG simulations were performed for the months of January and July 2015. The first half of January 2015 was characterized by (south-)westerly flow for most parts of Europe, except for the British Isles and Scandinavia. Therefore, unusually mild temperatures and low wind speeds prevailed, especially after 8 January. On 16 and 17 January, a prominent interfering system of disturbances with heavy precipitation swept across central Europe, which led to variable weather until the end of the month.

The first week of July 2015 was dominated by a strong heat wave over central and southern Europe, which was interrupted by a cold front around 8 July 2015 over central Europe. After this short interruption, the weather returned to stable high-pressure conditions resulting in above-average temperatures, low wind speeds, and only little precipitation over most of Europe, especially the western, southern and south-eastern parts.

3.2.2 Concentration fields

To illustrate the contributions of different source processes to the total signal of a given tracer, Figure 3-2 shows the monthly mean concentration fields of ^{14}C at the lowest model level (i.e., approx. 10 m above ground). The total $^{14}CO_2$ field is the sum over all contributing processes and over all regions, including the background $^{14}CO_2$ field, which has a mean near-surface value of 20.2 (20.3) ppmv for January (July) 2015 over the whole simulation domain. The mean $^{14}CO_2$ value is considerably higher in January (-1.7 ppmv) than in July (-0.7 ppmv). It is dominated by fossil fuel emissions showing highest (negative) concentrations in the most densely populated and industrialized regions of Europe. Biospheric activity has a net positive contribution and is more pronounced in July. The stripe in the north-eastern part of the domain is due to missing input data and should be ignored. Tracer fields from ocean fluxes are not shown because they are approximately one order of magnitude lower than their biospheric counterpart.

As expected, the strongest signals (up to -20 ppm) in ^{14}C are due to fossil fuel sources, which do not contain any radiocarbon. The signals are much larger in January than in July, mainly due to less effective vertical mixing in the winter months, but also due to larger emissions. Signals from biofuels are more than an order of magnitude smaller. In contrast to the anthropogenic ^{14}C tracers, the signals due to biospheric fluxes are much larger in summer than winter. They reach levels of about 1 ppm in summer, and spread more evenly over larger regions compared to the anthropogenic signals. Signals from nuclear power plants are high close to the sources (several ppm), but rapidly decrease with distance.

For both months, there were several time periods with very low horizontal pressure gradients over large parts of Europe. Accumulation of trace gases and, therefore, high concentration peaks can be expected in these regions. This effect is somewhat compensated by vertical mixing within the deeper convective boundary layer in July, as displayed in Figure 3-3. The figure presents total ^{14}C for those days in January and July, where the highest daily mean concentration of $^{14}CO_2$ (without background) was simulated. The fields show a three times higher daily mean concentration in January than in July 2015.

a) Total

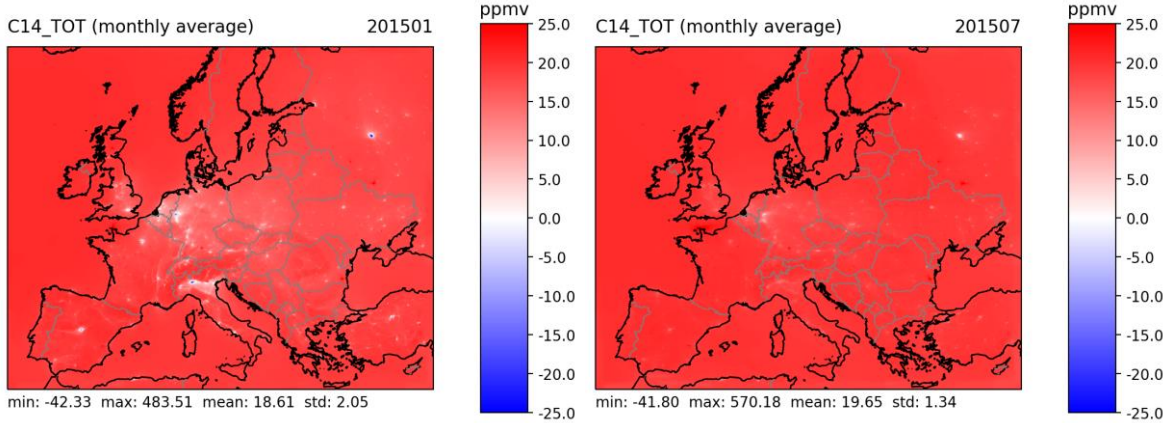

b) Fossil fuel

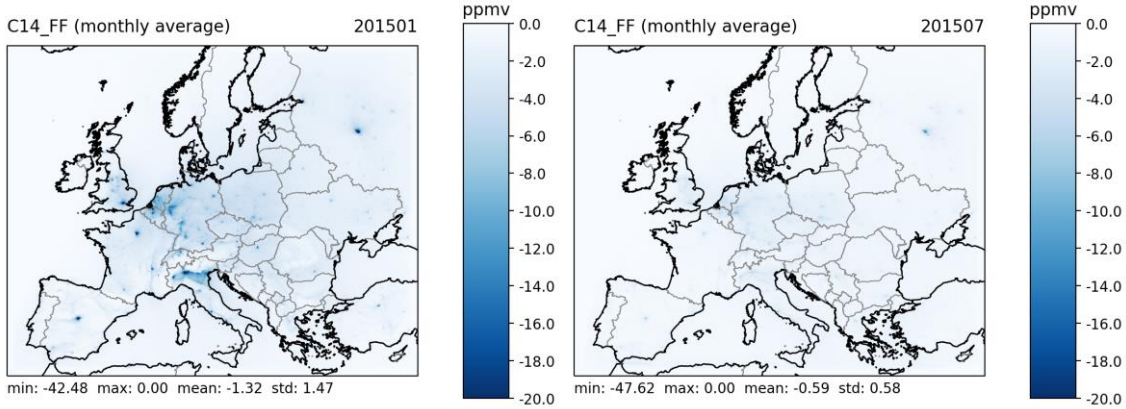

c) Biofuel

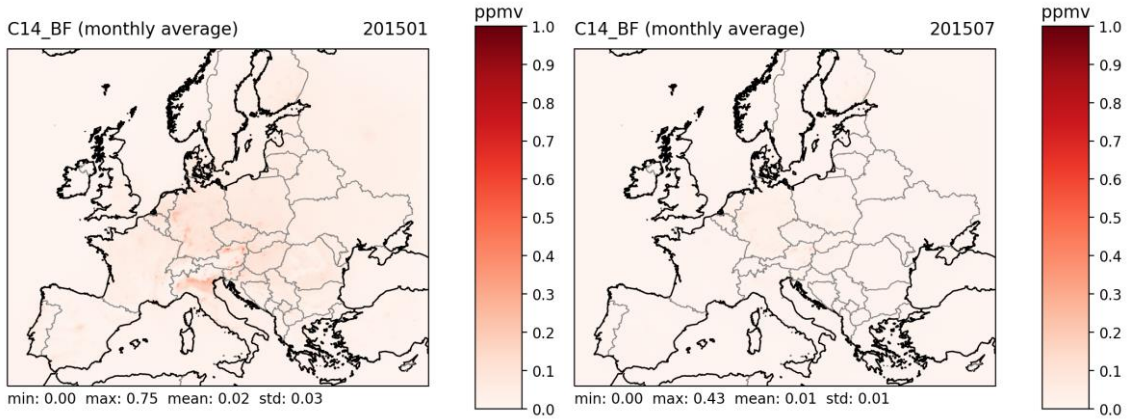

d) Nuclear power plants

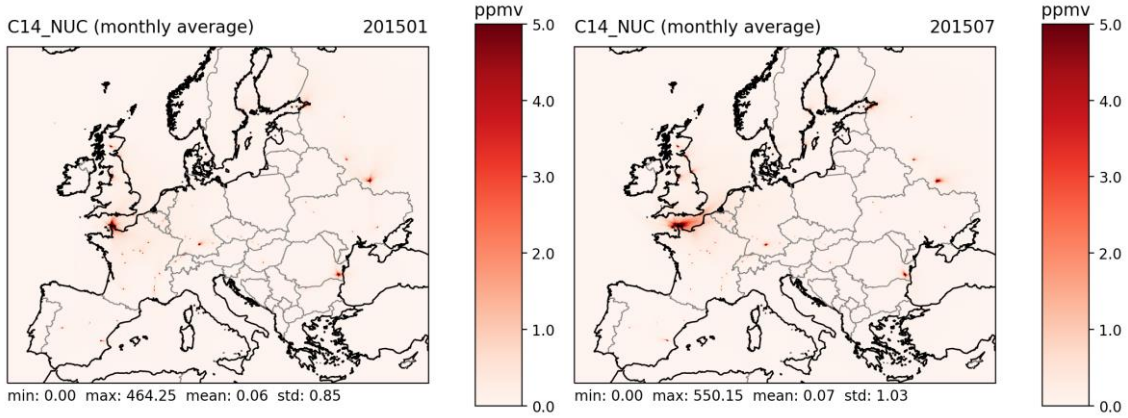

e) Natural

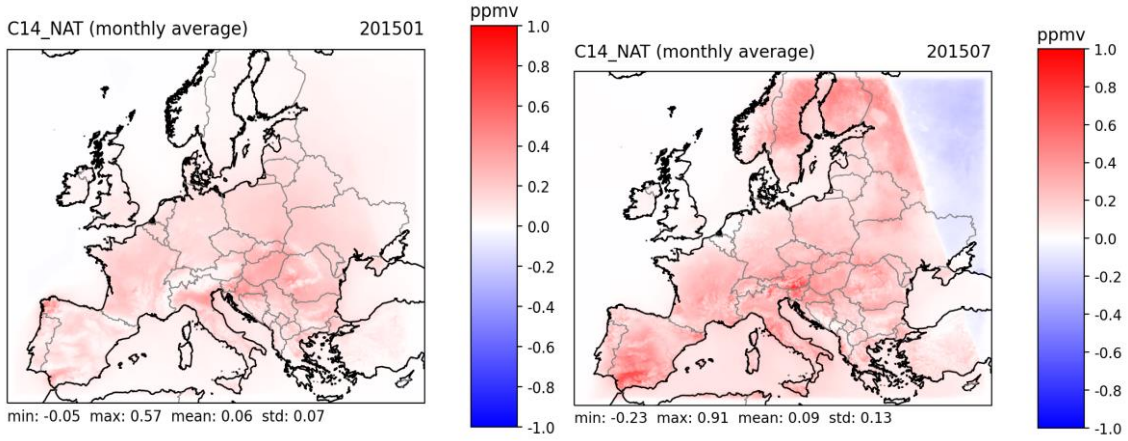

Figure 3-2: Monthly mean near-surface concentrations of a) total b) fossil fuel c) biofuel d) nuclear power plant and e) natural (biospheric and ocean) $^{14}CO_2$ for January (left) and July (right) 2015.

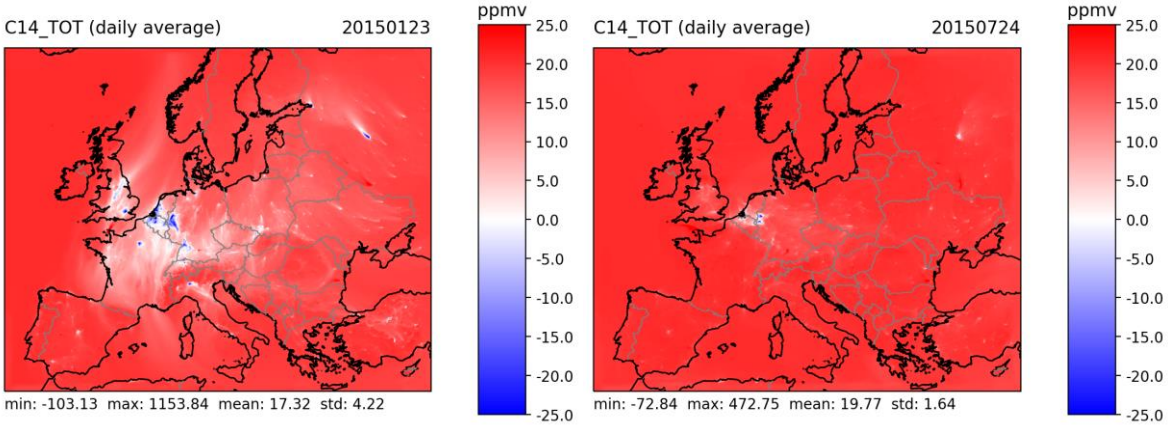

Figure 3-3: Daily mean near-surface concentrations of $^{14}CO_2$ on days with the highest averaged concentration for January (left) and July (right).

3.2.3 Fossil fuel variability

Whether a tracer like $^{14}CO_2$ or CO can be regarded as a suitable fossil fuel tracer depends on how much of its variability is explained by fossil fuel emissions. To illustrate this for the example of $^{14}CO_2$, Figure 3-4 shows maps of the temporal standard deviations (std) per grid cell of total $^{14}CO_2$ in January and July 2015, and Figure 3-5 (top row) the corresponding maps for the fossil fuel component, i.e. for the tagged fossil fuel CO_2 tracer. The variations for both tracers are approximately 2.5 to 3 times higher in January than in July. This again can be explained by stronger mixing within the PBL and dilution of trace gases in the summer months. Overall, the variabilities in the total and the fossil fuel tracer look very similar, suggesting that fossil fuel emissions are indeed the dominant factor contributing to atmospheric $^{14}CO_2$ variations over Europe.

This can be investigated in a more quantitative way by computing the ratio between std($CO_{2,fossil}$) and std($^{14}CO_{2,total}$) as shown in Figure 3-6. According to the COSMO-GHG simulations, the std-ratio for most terrestrial areas is close to 100% in January 2015. Distinctly lower values are located near nuclear power plants. The situation is more complex in July, where on top of the nuclear power plant signals the biospheric activity adds considerable variability. The domain-wide mean value of the std-ratio is 75% in this month (compared to 92% in January), while most countries in central and eastern Europe still have a value above 90%. For other regions, the contributions from fossil fuel emissions are much less prominent, since biospheric fluxes of $^{14}CO_2$ significantly add to the variability.

Figure 3-5 also shows the std of the fossil fuel CO component, and Figure 3-6 the ratio between std(CO_{fossil}) and std(CO_{total}). This ratio is high in densely populated and industrial areas, for example in western Germany and the Benelux countries. The fossil fuel contribution to variations in CO is much lower compared to $^{14}CO_2$. In winter, the mean ratio over the whole domain is only 44%, and in summer it further drops to 37%. One reason is that biofuels (notably wood burning) are an important source of CO, particularly in winter. Another reason is that variations in background concentrations are larger, because CO has a relatively short lifetime of a few months. This likely explains the lower ratio in summer, where fossil fuels only dominate close to the population and industrial centers, but contribute well below 50% over a large proportion of the European continent. It should be noted that CO could still be a valuable tracer of fossil fuels, if the signals from biofuels and fossil fuels are well correlated.

The contribution from fossil fuels to the variability in total CO is comparable to that for CO_2 in winter (see Figure 3-6), but is much larger in summer. In summer, CO_2 variations are largely dominated by biospheric activity except close to urban centers.

Figure 3-7 shows the monthly mean ratio between total CO and total CO_2. The spatial patterns look very similar in both months. However, the amplitude is higher in January, because of the higher background concentrations due to the longer lifetime of CO in winter and due to stronger CO emissions.

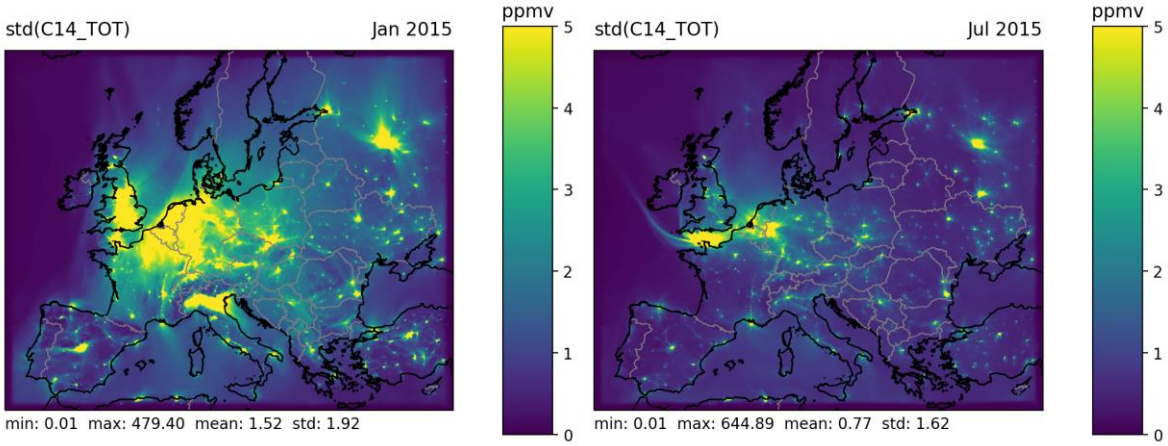

Figure 3-4: Near-surface standard deviations of total $^{14}CO_2$ for January (left) and July (right) 2015.

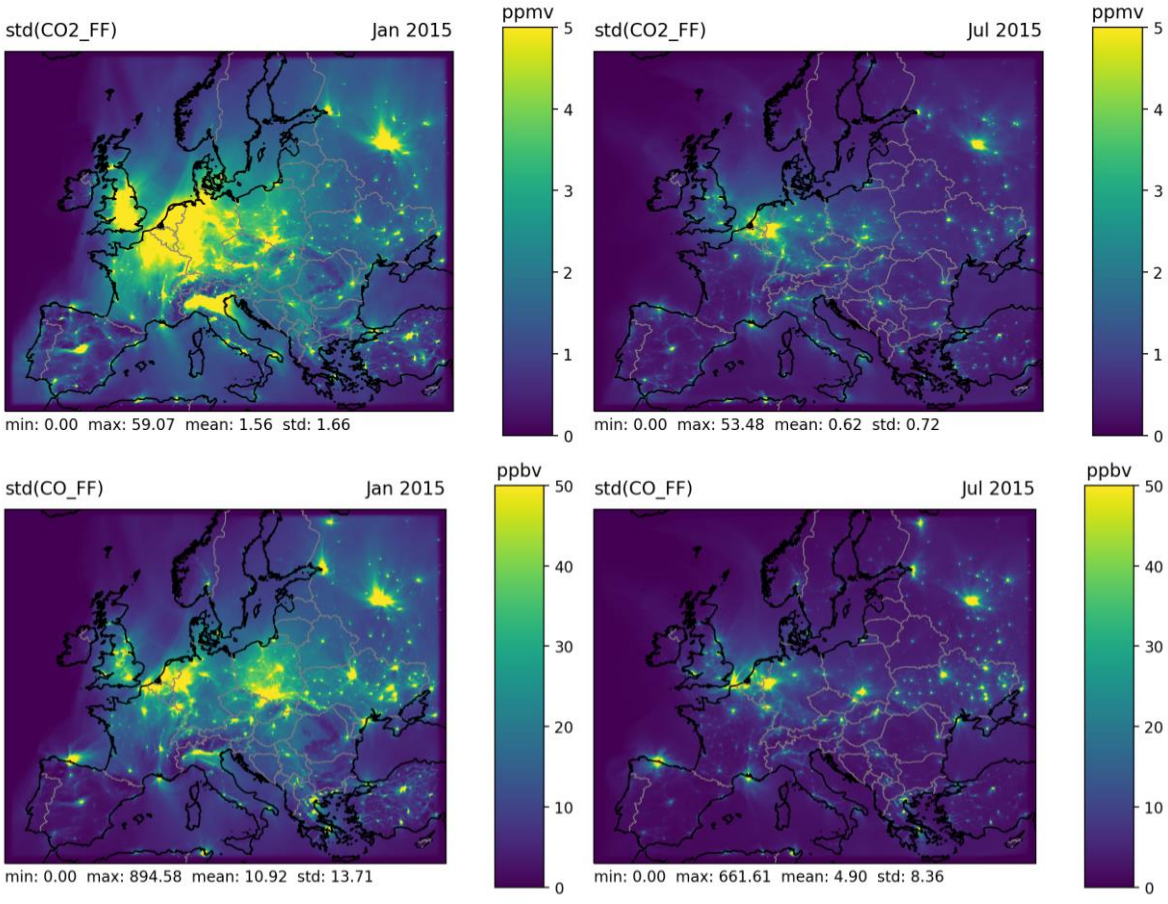

Figure 3-5: Near-surface standard deviations of fossil fuel CO_2 (middle), and CO (bottom) for January (left) and July (right) 2015.

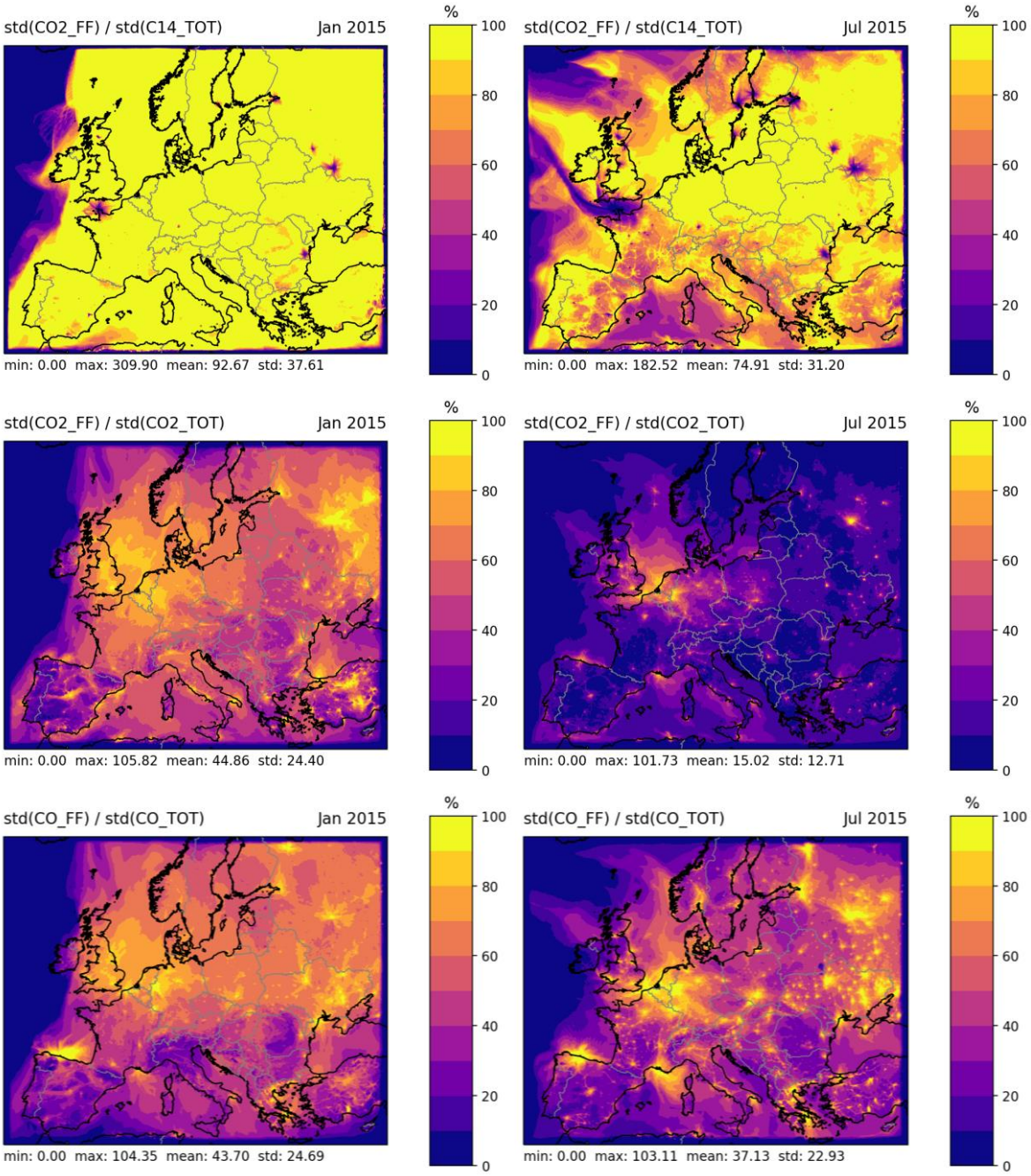

Figure 3-6: Near-surface standard deviation ratios between fossil fuel CO_2 and total $^{14}CO_2$ (top), fossil fuel CO_2, fossil fuel CO_2 and total CO_2 (middle), and fossil fuel CO and total CO (bottom) for January (left) and July (right) 2015.

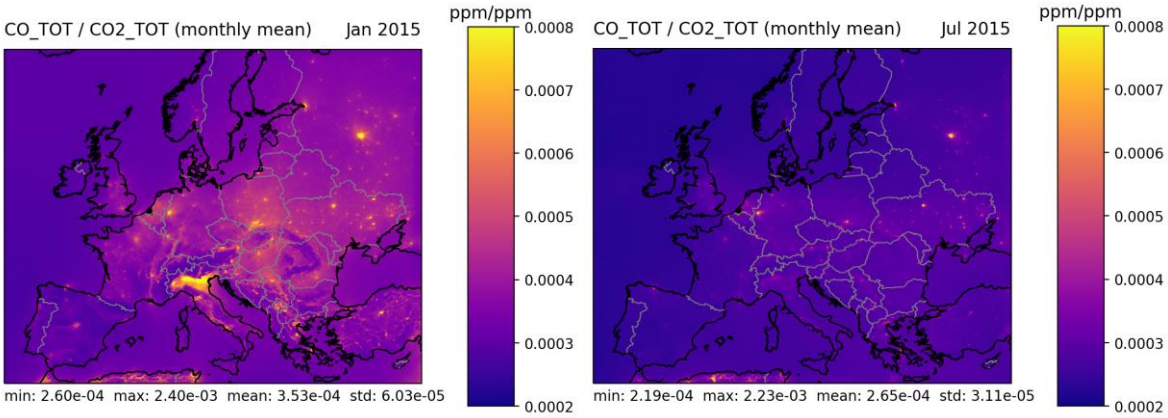

Figure 3-7: Mean ratio between total CO and total CO_2 for January (left) and July (right) 2015.

3.2.4 Station network analysis

An artificial station network was designed using a combination of the distribution of ICOS, NOAA and other GAW stations. If no GAW station was available, local meteorological or air quality sampling stations were taken. Additional urban stations were chosen to have a good coverage of the largest urban areas in Europe. This network design is based on the assumptions made in D4.3 (Section 5.3 Stations) and shown in Figure 3-8. All COSMO-GHG model output fields have been interpolated to all 237 stations.

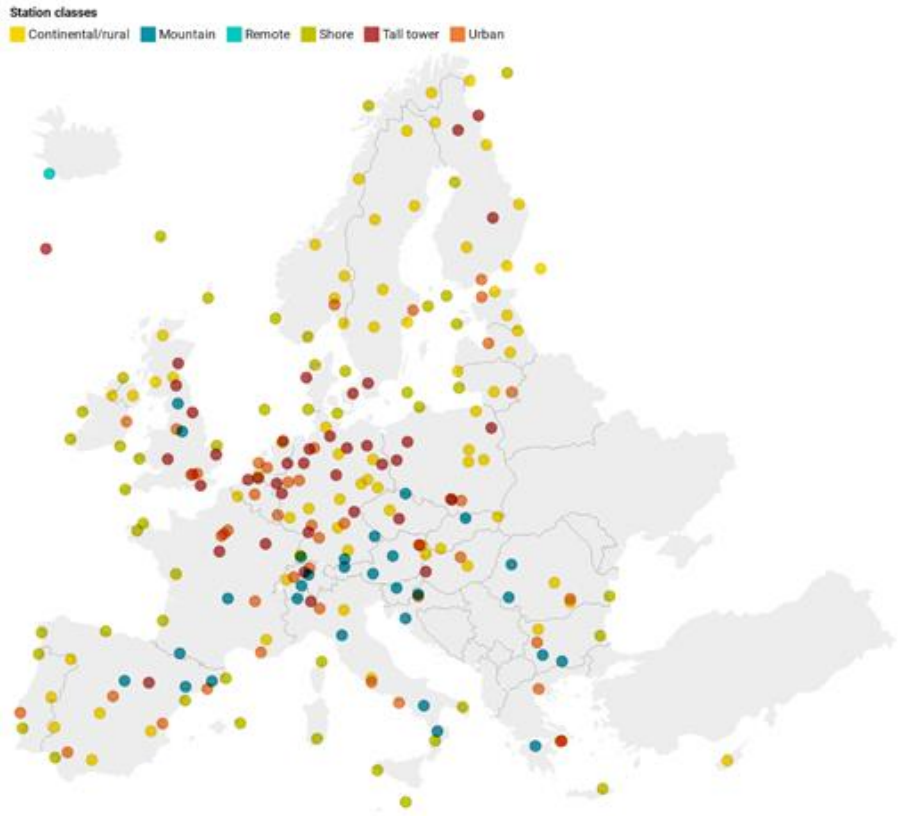

Figure 3-8: Station network proposal. Simulation data are extracted for all stations shown on the map, also considering the sampling height.

Two contrasting stations of this network are selected for the analysis shown here, one rural and one urban station, to illustrate how the tagged tracers help dividing variations in tracer concentrations measured in a specific location and environment into contributions from different source processes and regions.

Melpitz, the first station, is located in a rural area near Leipzig in the eastern part of Germany. The main wind sector for Melpitz is southwest. Air masses reaching Melpitz from this direction transport a mixture of maritime and continentally influenced air masses after crossing large parts of Western Europe. The second most frequent wind sector is east, and is characterized by continental air masses influenced by long-range transport of anthropogenic emissions from Poland, Slovakia, the Czech Republic, Belarus and Ukraine. Note that only the last two countries are assigned to the area "Eastern Europe", the others belong to "Central Europe" (cf. Figure 3-1).

The second station selected for the analysis is the city of Milan in the highly polluted Po Valley in Italy. High anthropogenic emissions in combination with a frequent occurrence of stable atmospheric conditions often lead to strong accumulation of anthropogenic tracers. The region around Milan is characterized by croplands, therefore a significant biospheric influence can be expected as well.

Figure 3-9 shows time series of regionally separated, daily-averaged concentrations of fossil fuel CO_2 (CO2_FF, where δ_{FF} = -1000 ‰) at the two sites in January and July 2015. For Melpitz, the fossil fuel signal mainly originates from central Europe with small contributions from western Europe (10-20%). The fossil fuel mole fractions are about three times higher in January compared to July (10 vs 3.5 ppm maximum).

In Milan, the fossil fuel signal is almost entirely attributed to southern Europe. On most days, less than 10% of the tracer originates from longer distances such as central and western Europe. Compared to Melpitz, the magnitude of the fossil fuel signals differs even more between seasons. In winter, daily averaged values can exceed 40 ppm while summer values are less than 6 ppm, which corresponds to a ratio of approximately 7 to 8.

Figure 3-10 - Figure 3-13 show time series of source-separated, daily-averaged concentrations of total $^{14}CO_2$, CO_2 and CO (without background fraction, respectively) at those sites. The signals in the city of Milan have an overall greater amplitude compared to those at the rural station Melpitz. In Milan, the relative fossil fuel contribution is more pronounced in all three tracers.

In winter, emissions from fossil fuels strongly dominate the $^{14}CO_2$ signal both in Melpitz and Milan, consistent with Figure 3-6. In July, heterotrophic respiration and biofuels add up to a non-negligible contribution, especially at Melpitz. On days with very strong biospheric activity, this can be up to 25% compared to the fossil fuel fraction. On other days during July, it is about 10-15%.

The CO_2 signal is also dominated by fossil fuel emissions in winter, but biofuels and especially heterotrophic respiration contribute as well. In Milan these contributions are relatively small, in the range of 10-20%, but in Melpitz they occasionally add up to 50% of the total CO_2 signal above background. In summer, the situation is very different. Even in Milan, the biospheric signals are significantly larger than the fossil fuel CO_2 signal, though positive contributions from respiration and negative contributions from GPP tend to offset each other, strongly reducing the net biospheric CO_2 signal and leaving the fossil fuel signal as the dominant component. Note, however, that this is only true for daily mean values. Respiration fluxes are significantly smaller than GPP in July, but because they occur at night in a shallow boundary layer, they contribute as much to the daily mean concentrations near the ground as GPP (known as the "rectifier effect"). For afternoon values, which are typically used in inversions,

the situation would likely be different with GPP being the dominant component. At Melpitz, the fossil fuel signals are only 10-30% of the gross biospheric signals, though GPP and respiration are largely compensating each other also at this station. Biofuels are much less important in summer than in winter since biofuels are primarily used for heating.

Interestingly and in contrast to $^{14}CO_2$ and CO_2, the contribution to CO from fossil fuels is larger in summer than in winter, because biofuels are an important source of CO emissions but are less used in summer. This could make CO an attractive fossil fuel tracer in summer. This finding seems to be in conflict with Figure 3-6, which suggests that variations in the tagged fossil fuel CO tracer contribute on average only 37% to variations in total CO during summer. However, the analysis presented here does not include background CO concentrations, which were included in Figure 3-6. Variations in background concentrations appear to make a large contribution to the overall variability in CO during summer. Since these variations are likely spatially smooth, it might be possible to separate them from fossil fuel signals.

Figure 3-9: Time series of simulated region-separated fossil fuel CO_2 concentrations for Melpitz (top) and Milan (bottom) for January and July 2015.

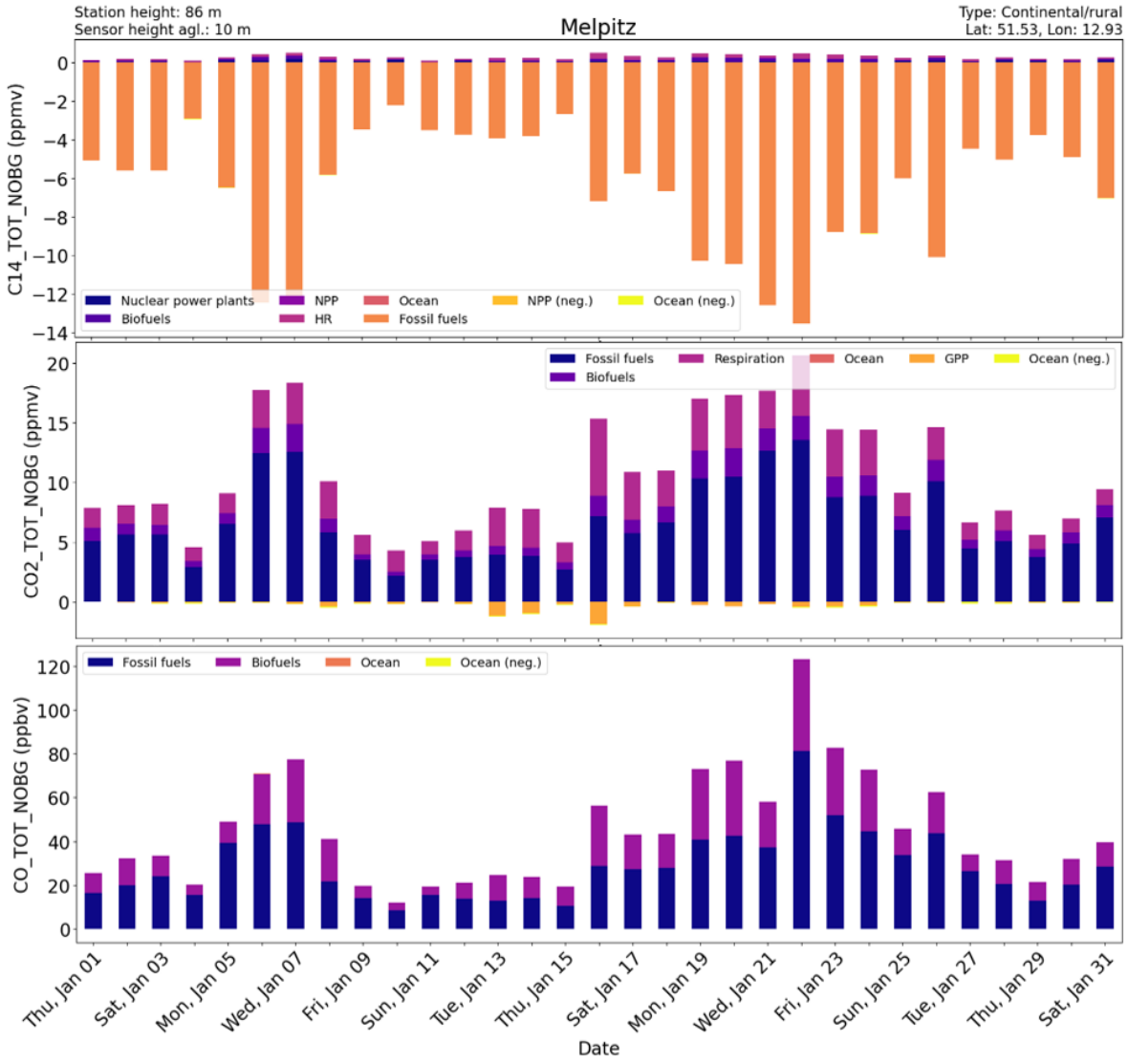

Figure 3-10: Time series of simulated source-separated $^{14}CO_2$, CO_2 and CO concentrations for Melpitz for January 2015.

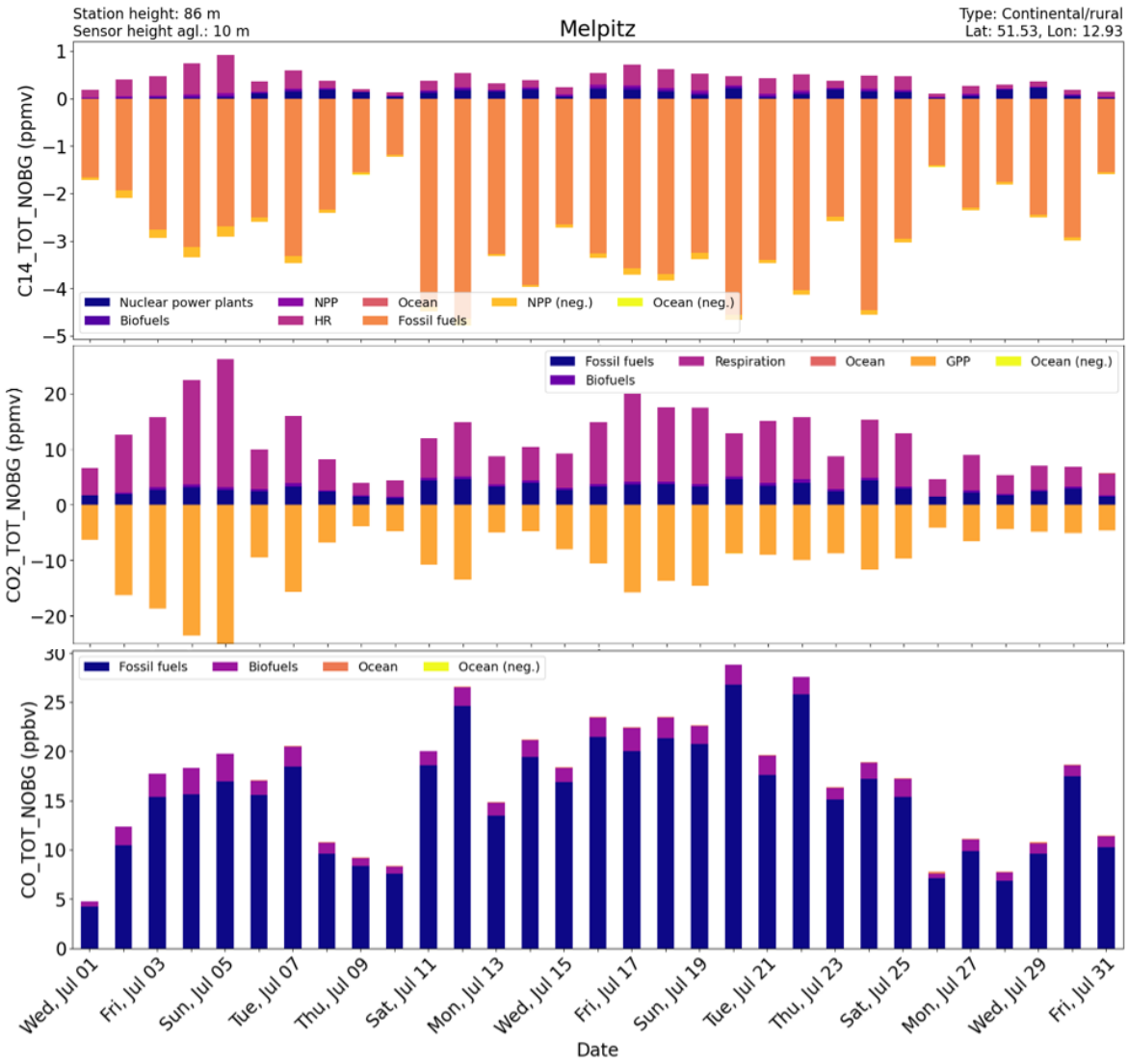

Figure 3-11: Time series of simulated source-separated $^{14}CO_2$, CO_2 and CO concentrations for Melpitz for July 2015.

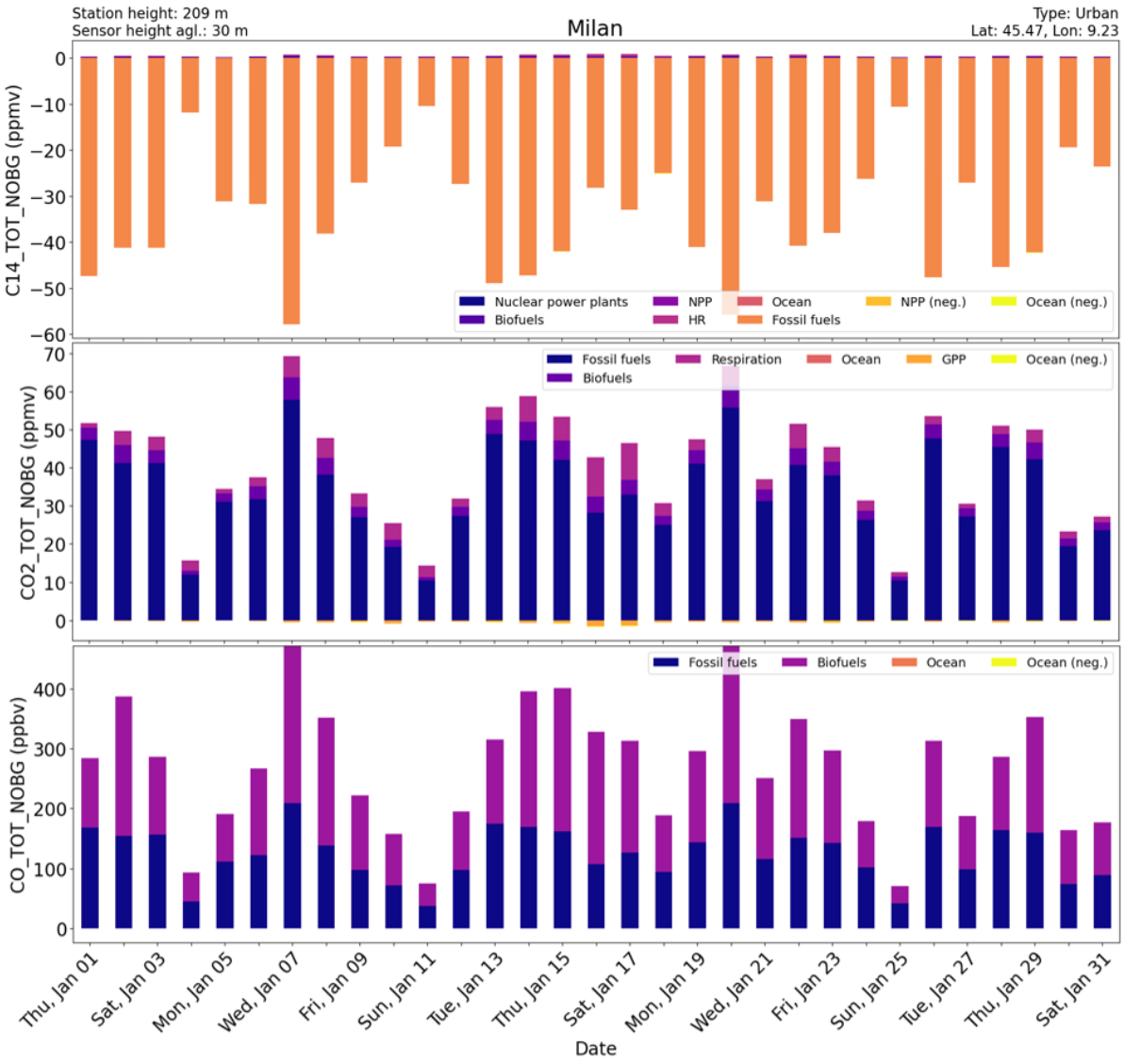

Figure 3-12: Time series of simulated source-separated (anthropogenic and natural) $^{14}CO_2$, CO_2 and CO concentrations for Milan for January 2015.

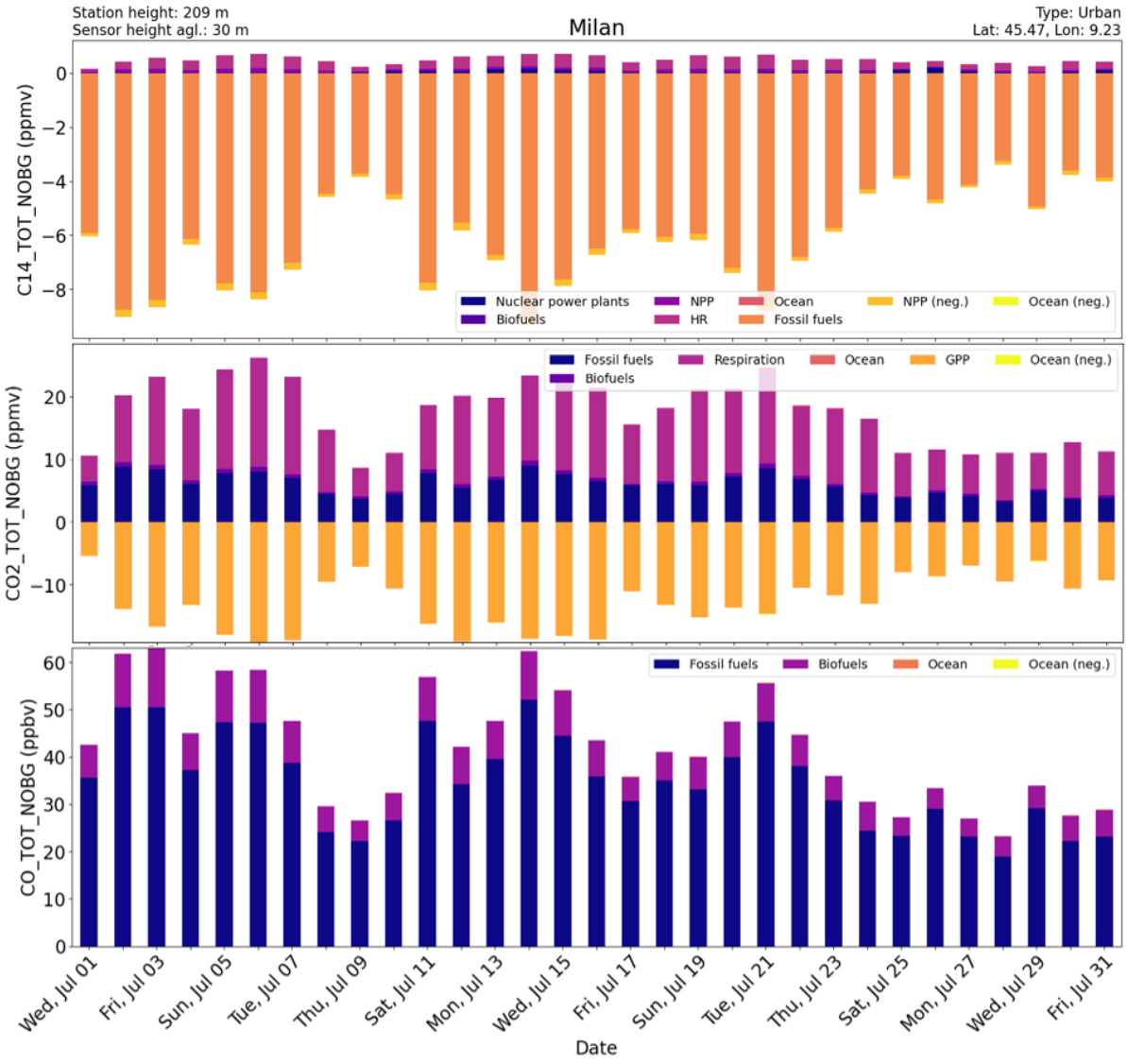

Figure 3-13: Time series of simulated source-separated (anthropogenic and natural) $^{14}CO_2$, CO_2 and CO concentrations for Milan for July 2015.

3.3 Recommendations for the surface network

Based on the analyses of the near-surface emission signals of $^{14}CO_2$, CO_2 and CO, we propose the following recommendations regarding the network design:

1. Fossil fuel signals are much larger and contribute more prominently to the variability in $^{14}CO_2$, CO_2 and CO during winter as compared to summer. Quantification of fossil fuel CO_2 emissions is therefore easier during winter in principle, but in practice only ground-based in-situ measurements are available continuously throughout the year, while satellite observations are more difficult during wintertime due to larger cloud coverage and due to larger solar zenith angles.
2. The emission signal registered at a certain station is mostly dominated by the region it is located in. Long-range transport from neighbouring regions plays an inferior role. This suggests that a single station cannot be representative of one of the large regions

defined in our analysis (see Figure 1). Many more stations per region are required, but our analysis is too limited to provide a good number.

3. Nuclear power plant emissions can have a significant effect on radiocarbon measurements. However, this only affects stations which are in close proximity (approx. 100 km) and only during periods when the plume reaches the station. Filtering out such periods should make it possible to minimize interferences from nuclear power point signals.
4. Radiocarbon is an extremely valuable tracer of fossil fuel CO_2 emissions. In winter, fossil fuel emissions strongly dominate $^{14}CO_2$ variability (90% - 100%) over most of Europe. However, in summer their contribution drops to 70%-80% due to a non-negligible contribution from biospheric fluxes.
5. CO could be a particularly valuable tracer of fossil fuel emissions during summer, when the use of biofuels is reduced. However, this would not be true during periods of biomass or agricultural waste burning. Further, since variations in background CO concentrations are relatively large in summer, it would be necessary to separate large-scale variations in background CO from smaller-scale variations in fossil fuel CO. With a sufficiently dense measurement network, such a separation should be feasible.
6. As shown in previous studies, CO could also be useful as a high-frequency tracer, that can be used to apply a time interpolation between (weekly) ^{14}C measurements. However, since CO has a large contribution from biofuels, this can only be successful if the signals from biofuels and fossil fuels are strongly correlated. Comparing the time series of biofuel and fossil fuel CO at Melpitz and Milan, the correlation appears to be quite high, but a more detailed analysis for whole Europe is required.

4 Assessment from MPG

In this study, we used the Jena Carboscope inversion system, to assess our ability of a potential air sampling network to separate the contribution of fossil fuel emissions to the atmospheric CO_2 mole fraction from the contribution of other processes, primarily biospheric fluxes, by using measurements of co-emitted species ($^{14}CO_2$, CO and APO) as a constraint. The setup is described in detail in D4.3.

4.1 Geospatial network configuration

The first step was to select the geospatial configuration of our hypothetical station network. The ICOS network was taken as base design. Additionally, we selected a more rural or more urban configuration or a mixture of both. The potential network configurations were also designed with varying station densities. In D4.3, we identified 237 potential stations – divided into rural and urban categories. The location of the rural stations was based on the ICOS network, from the Global Atmospheric Watch (GAW) and the National Oceanic and Atmospheric Administration (NOAA) global flask sampling network. The locations of urban stations were based on the ICOS and GAW networks, as well as local air quality networks, meteorological stations or universities (examples in Figure 4-1).

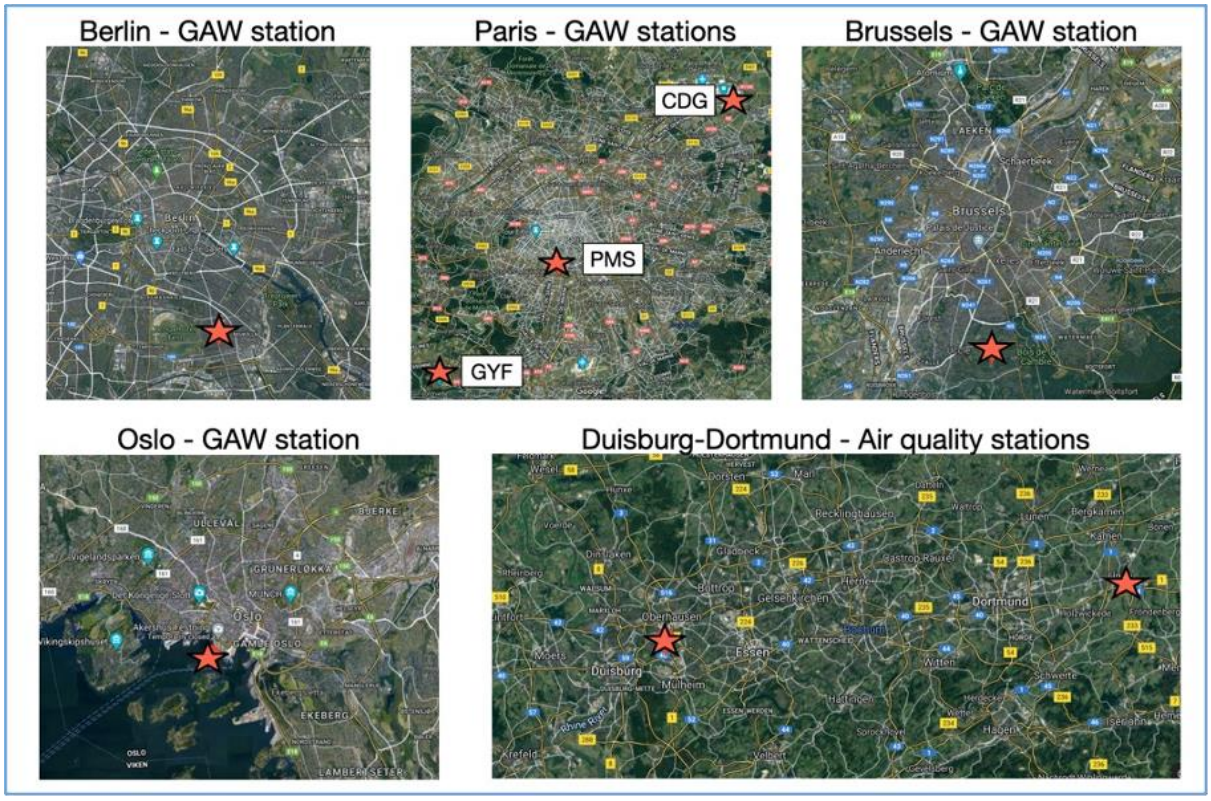

Figure 4-1 Examples of urban station locations from D4.3. Images from Google Maps.

We used the Stochastic Time-Inverted Lagrangian Transport (STILT) model (Lin et al., 2003, 2004, Gerbig et al., 2003) to derive the instantaneous footprints – upwind influence regions on atmospheric measurement locations – of over 237 stations in hourly time steps from 2014-12-31 00:00:00 to 2016-01-01 00:00:00. The STILT model was driven by ECMWF and WRF meteorology. Footprints were calculated with a resolution of 1/16˚ longitude and 1/24˚ latitude, which approximates 5 km over Central Europe. Because of the size of the data, we also calculated the footprints at 0.25˚ degrees resolution to make them manageable. Due to computational constraints, we reduced the domain to 15˚W-35˚E and 33˚N-73˚N (known as

STILT04 grid). The footprint analysis in this section was performed at this coarser resolution. To perform our analyses, we aggregated the instantaneous footprints into an annual footprint for each station.

A first hypothesis was that it should be possible to group the 237 stations based on their transport patterns. For this we calculated the correlations between the yearly aggregated footprints (Figure 4-2) and clustered them using hierarchical clustering analysis (R function *hclust* in package *stats*) using the Euclidean distances of the correlation matrix (R function *as.dist* in package *stats*). We grouped our stations into 18 geographically distinct clusters (Figure 4-3), which can be interpreted as stations which have a similar area of upwind influence.

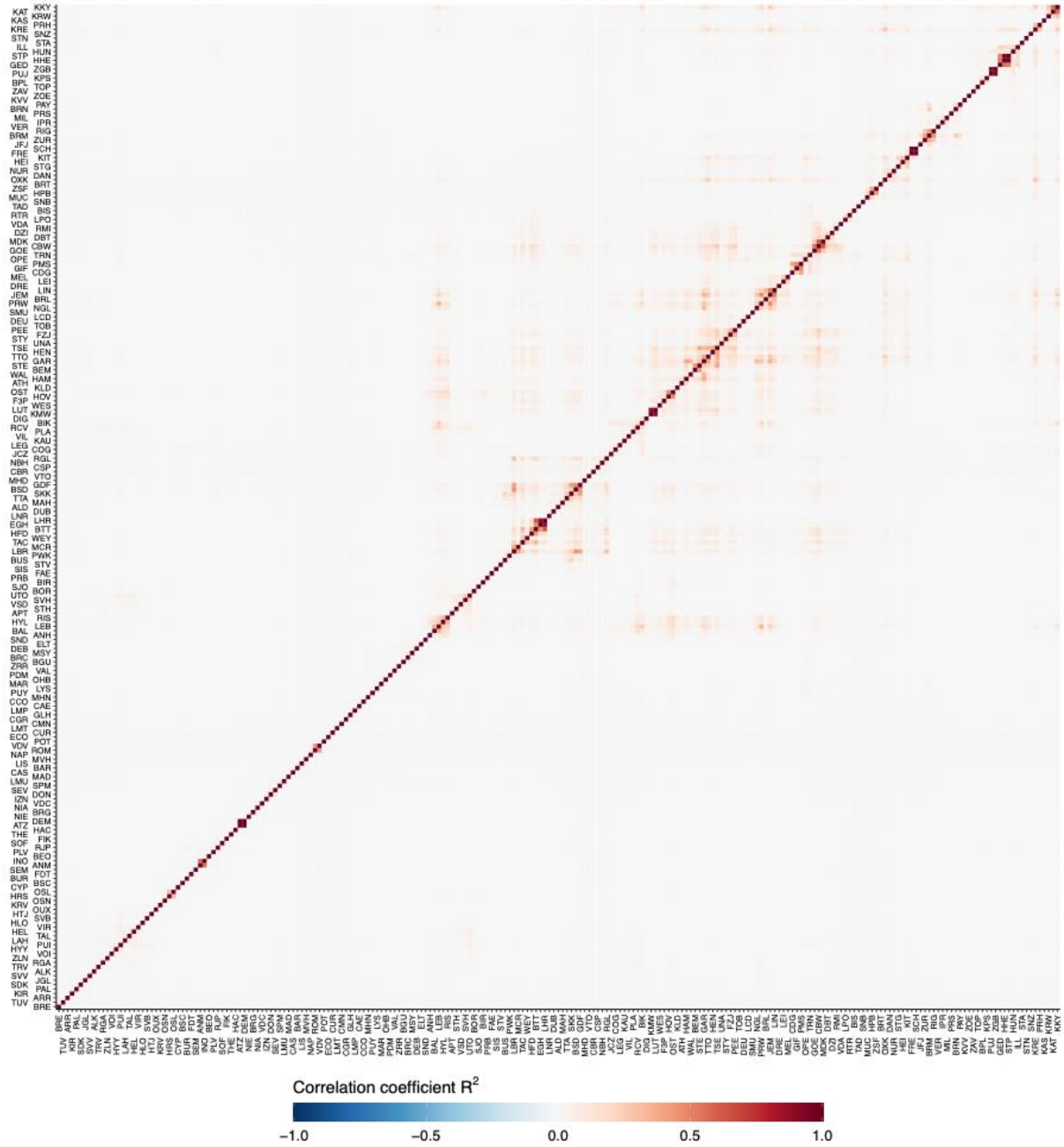

Figure 4-2 Correlation matrix between the yearly aggregated footprints of the 237 stations simulated.

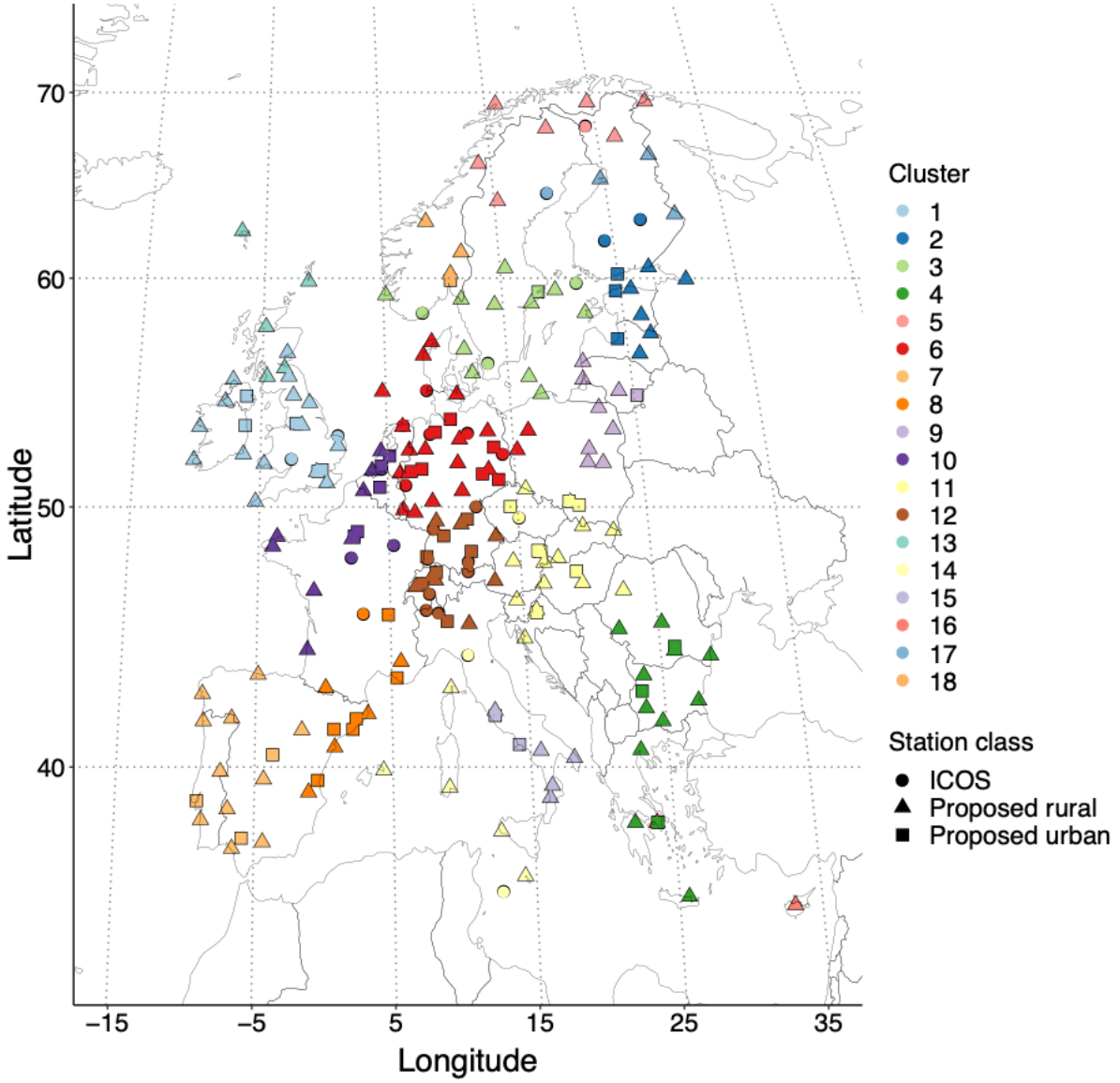

Figure 4-3 Clusters extracted from the correlation matrix of the annual footprints.

To choose stations from each cluster, we created a metric composed of three factors or rankings (normalized from 0 to 1):

1. how correlated is a station with other stations was represented as the sum in quadrature of the correlations along the correlation matrix. Stations with footprints only correlated to themselves would get the highest rank.
2. the average annual footprint weighted by the area covered by the footprint
3. the average annual footprint weighted by the fossil fuel emission density within the footprint.

The rankings correspond to their relative position in the graphs in Figures 4-4, 4-5, and 4-6. The first ranking tells us how unique or how redundant are the signals measured at a particular station with respect to those measured at other stations. In the second and third metrics, we aggregated the instantaneous footprints into an annual footprint (as already mentioned above) and calculated an average sensitivity value weighted either by the area covered by the footprint or by the fossil fuel emissions within the footprint. As expected, we found that urban stations are much more sensitive to fossil fuel emissions. In contrast, ICOS stations have a

low sensitivity to fossil fuel emissions particularly those located in remote areas of Scandinavia or Lampedusa, located in the Mediterranean Sea. This is because the ICOS network was designed to constrain biospheric CO_2 fluxes, which are the most uncertain component of the carbon cycle. To prevent interference, ICOS stations are located mostly far away from anthropogenic sources. Furthermore, we find that footprints of mountain stations tend to have a larger footprint area. However, the footprint magnitude weighted by the gridcell area may be skewed by the fact that grid cells have a larger area towards the equator.

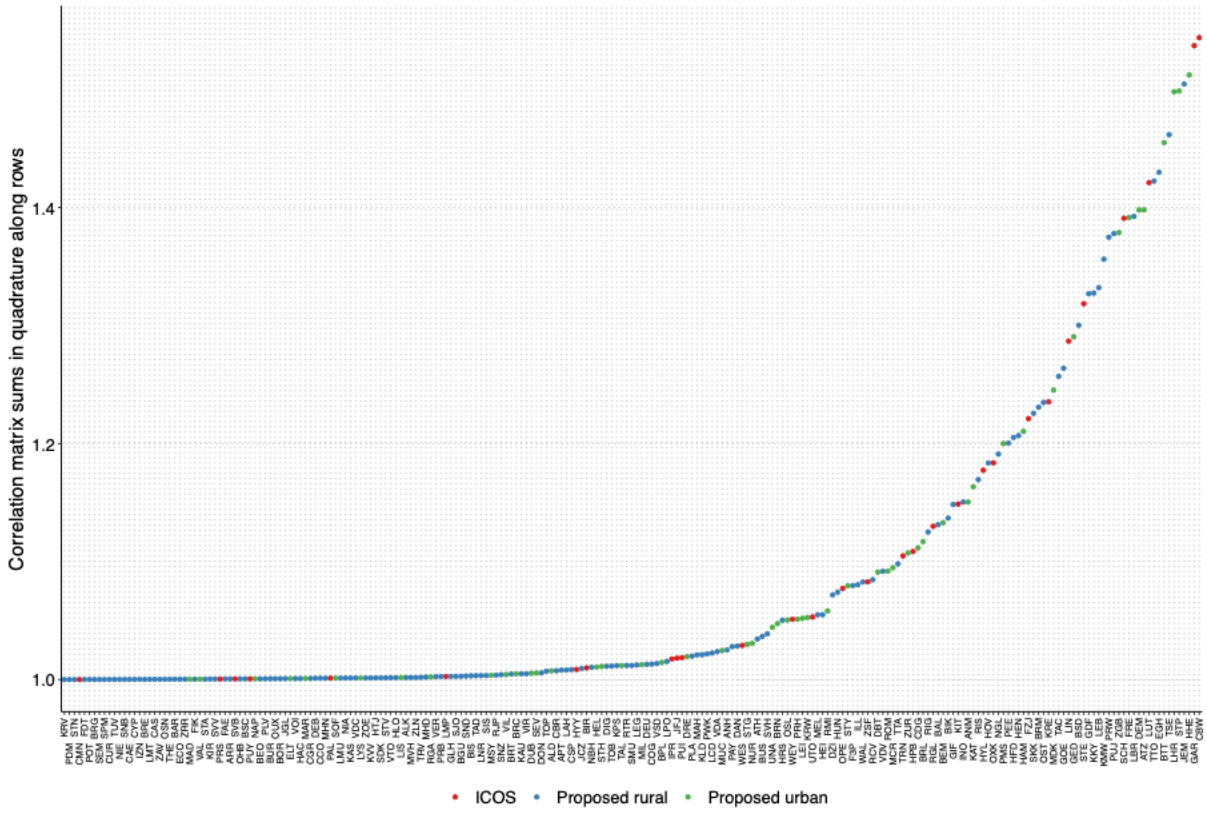

Figure 4-4 Sums in quadrature along the rows of the correlation matrix. Stations are ordered from least to greatest.

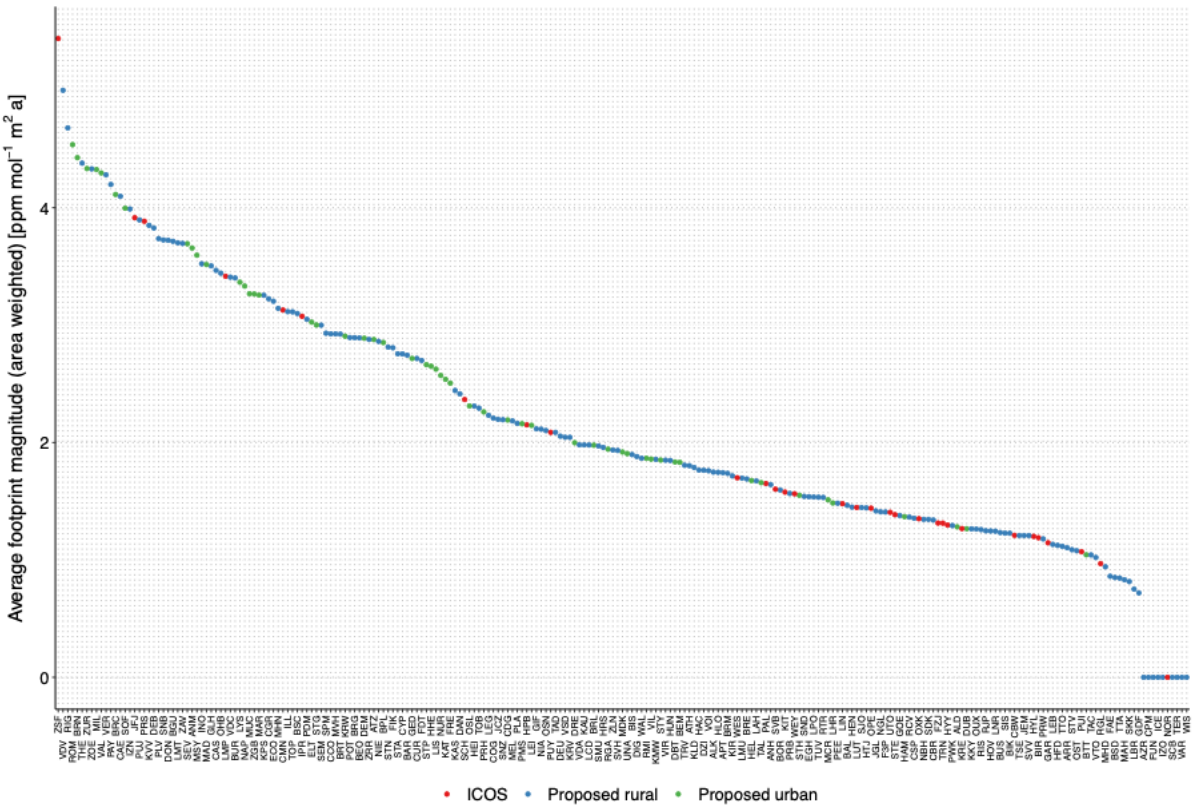

Figure 4-5 Station average footprint magnitude weighted by the area of the footprint. Stations are ordered by footprint magnitude.

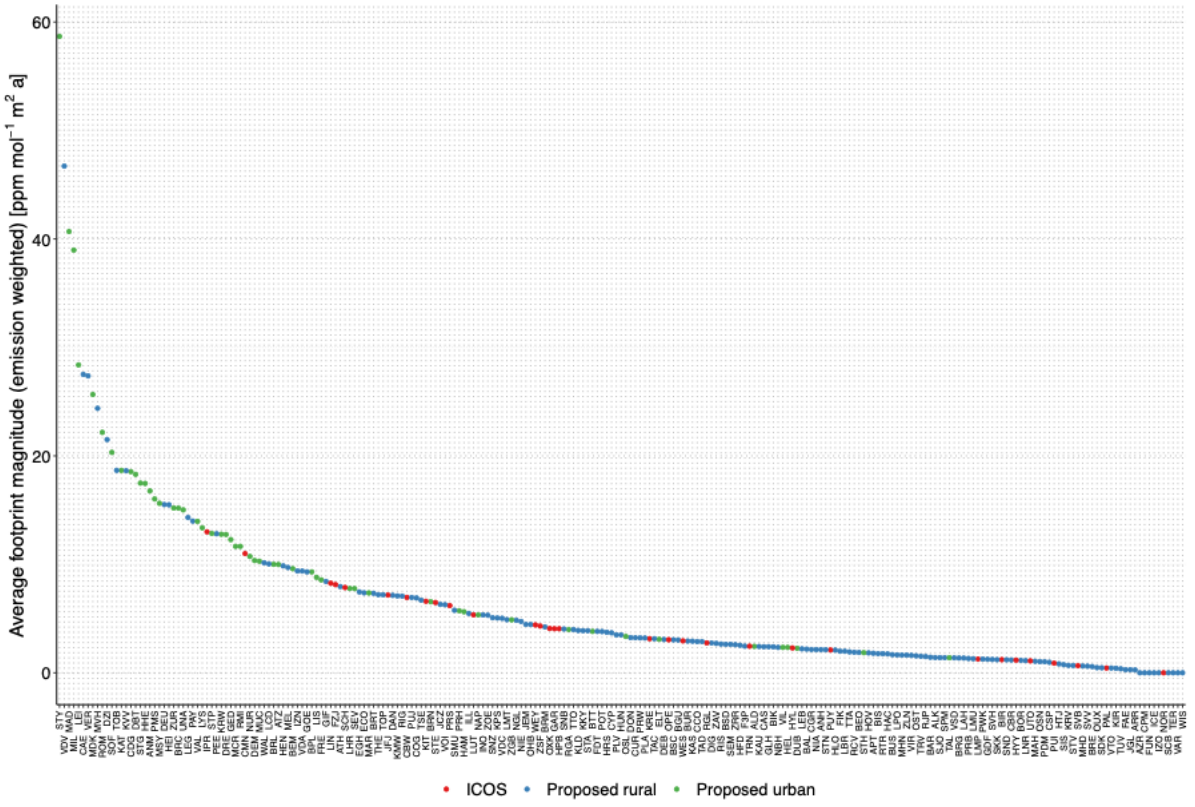

Figure 4-6 Station average footprint magnitude weighted by fossil fuel emission density. Stations are ordered by footprint magnitude.

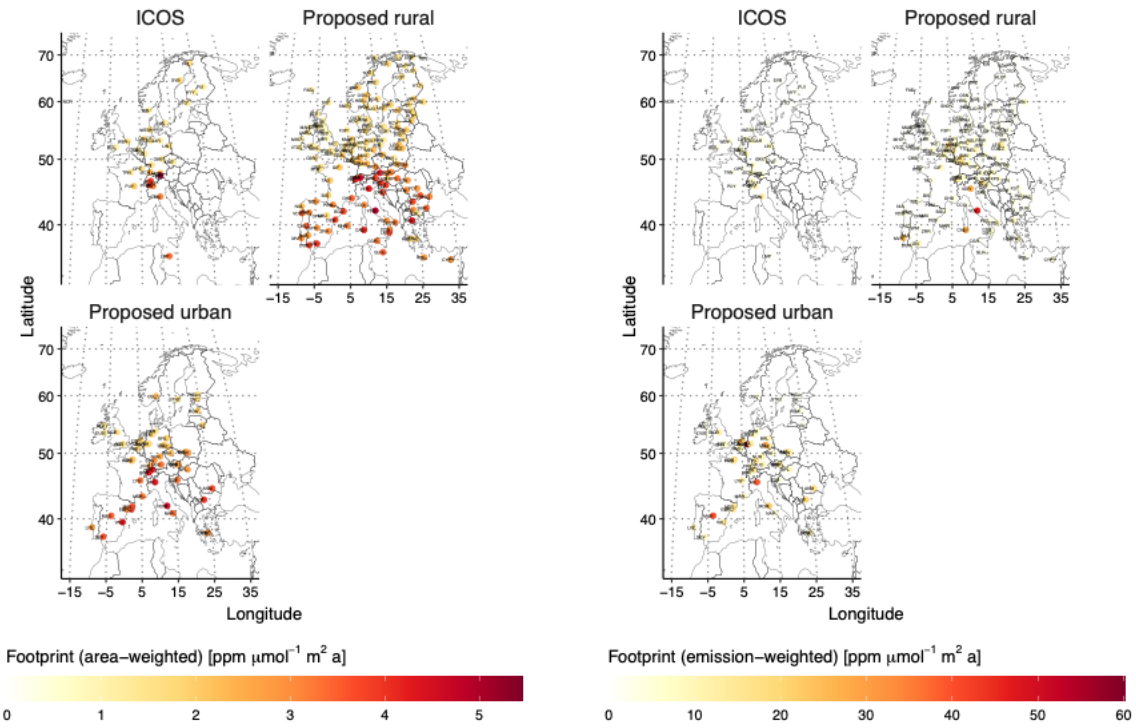

Figure 4-7 Geographical distribution of average footprint magnitude weighted by area (left) and by fossil fuel emission density (right).

We selected a set of stations from each cluster using the product of these rankings normalized as value from 0 to 1 (Figure 4-8). The selection was made with the following criteria:

- The base configuration is the ICOS network. The ICOS network is included in all setups.
- Sparse configuration: the highest-ranking station per cluster was added to the network.
- Median configuration: all stations with a ranking above the median of each cluster were added to the network.
- High density configuration: includes all stations.

Station networks were also classified as rural, urban or a mixture. The resulting network configurations can be observed in Figure 4-9

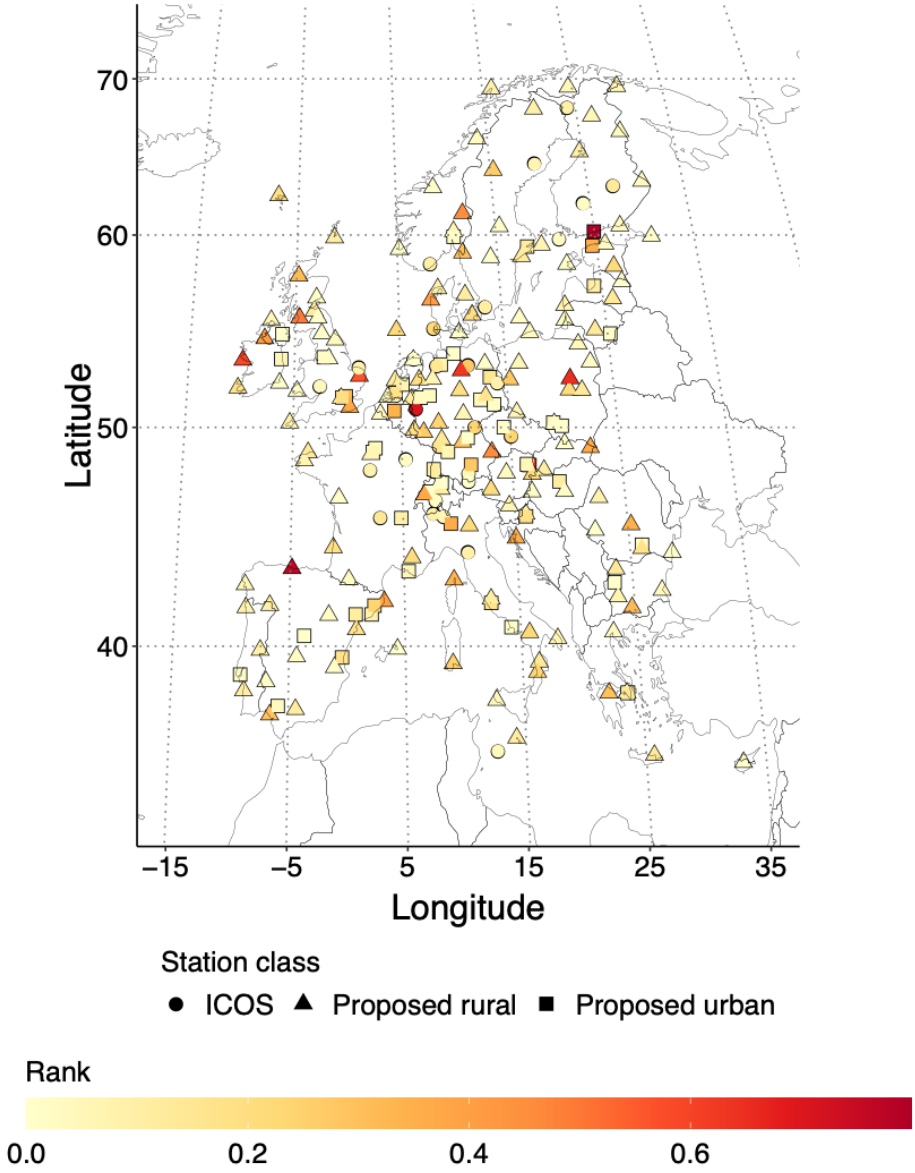

Figure 4-8 Final ranking of stations

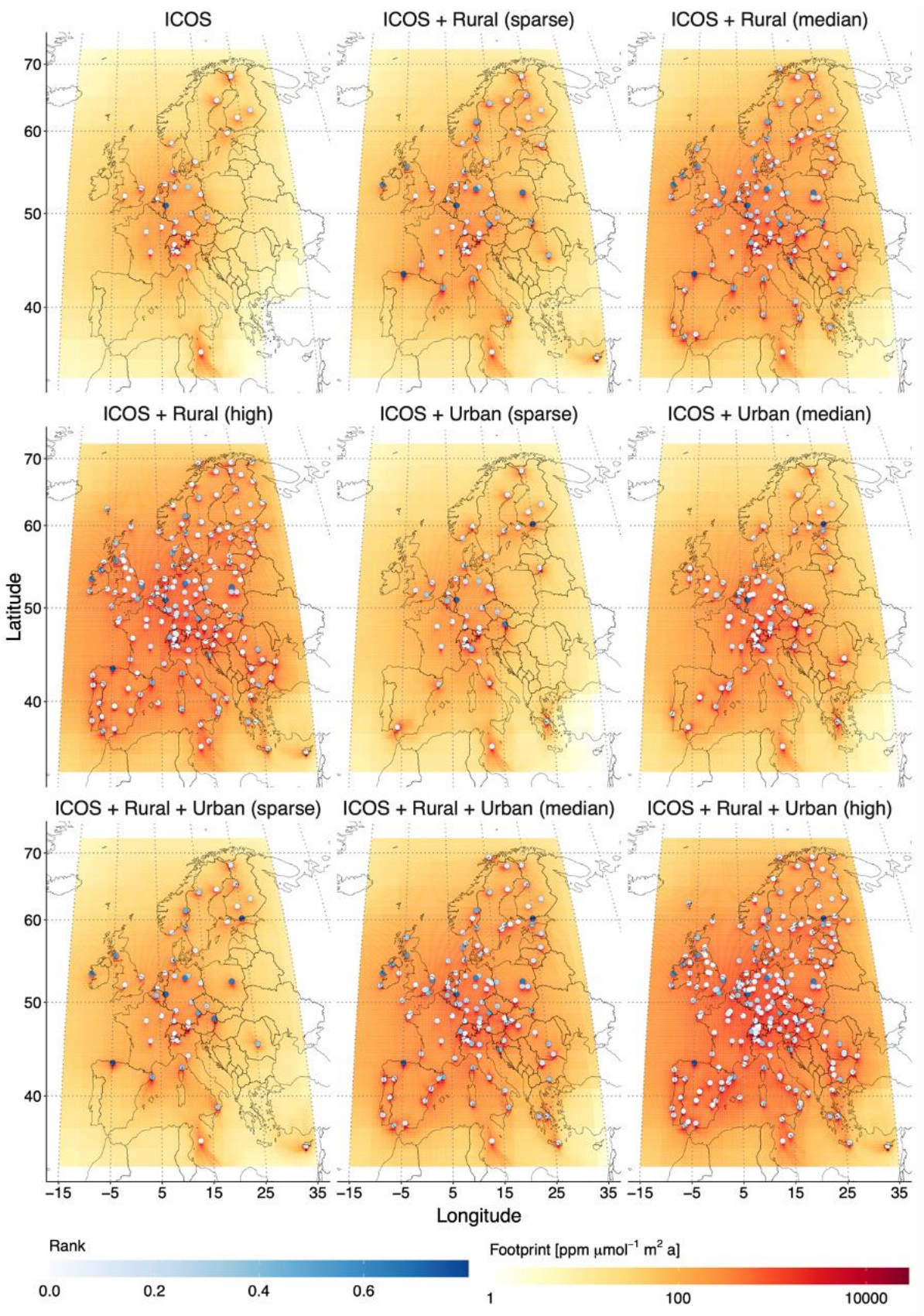

Figure 4-9 Geographic distribution of potential network configurations

4.2 Forward assessment

To date no dataset of simultaneous, high-frequency and high-precision CO_2, $\delta^{14}CO_2$, CO and APO which can be used to assess the ability of each tracer to estimate the fossil-fuel-derived CO_2 mole fraction ($ffCO_2$). Furthermore, in the case of $\delta^{14}CO_2$, measurements are taken only as weekly or biweekly samples because of their cost and complexity. In the Jena Carboscope inversion system, the (hourly) footprints calculated with the STILT model serve as transport operator to link the fluxes to atmospheric measurements. Therefore, we can use our emission inventories to produce a set of pseudo-observations at hourly time steps across our proposed network of 75 stations within the reduced domain[1] for all four tracers

4.2.1 Signal strengths

Because we are interested in the yearly budget, we first want to understand the overall magnitude of the signals of the different processes that we are considering in this study to determine which tracer is most sensitive to which process and at what relation with respect to the others and how this varies across the network (figures 4-10, 4-12 and 4-13). Here we use the term magnitude as the r.m.s. power of the tracer signal:

$$y_{rms} = \sqrt{\frac{\sum_{n=1}^{N} {y_n}^2}{N}} \qquad \text{(Eq. 4-1)}$$

where y_n is the hourly mole fraction of the tracer and N is the number of hourly samples in the time series.

For the Western European domain, fossil fuels emissions and biospheric fluxes produced the strongest CO_2 mole fraction signals with average magnitude of 13.46 ± 28.9 and 8.31 ± 4.78 ppm respectively. However, the sensitivity to fossil fuels concentrated near urban centers while sensitivity to biospheric fluxes is more evenly spread but is slightly larger away from urban centers (e.g., the Alps regions). Large biomass burning events may also create strong localized signals (average over the domain of 2.87 ± 8.88 ppm). Anthropogenic biofuel combustion emissions produced only a minor signal (0.83 ± 0.58 ppm) and the influence of oceanic fluxes was negligible (0.04 ± 0.05 ppm).

Biospheric fluxes are responsible for the largest $^{14}CO_2$ mole fraction signals, which mirror the spatial patterns of CO_2 biospheric fluxes. However, because of their weak isotopic leverage (the isotopic signature of the fluxes relatively similar to the isotopic signature of the atmosphere), the atmospheric signal $\delta^{14}CO_2$ is only increased by an average of 0.51 ± 0.33 ‰ (Figure 4-11). In contrast, fossil fuel emissions, which are void of $^{14}CO_2$ ($\delta^{14}CO_2$ = -1000 ‰), have a strong isotopic signature leverage. As a result, fossil fuel emissions cause the largest shift of the $\delta^{14}CO_2$ signal (on average -11.01 ± 12.01 ‰). However, while fossil fuel emissions are void of $^{14}CO_2$, $^{14}CO_2$ is emitted from gas-cooled nuclear power plants with no $^{12}CO_2$ counterpart. This means that the decrease $\delta^{14}CO_2$ signal caused by fossil fuel emissions is offset in regions downwind from areas with a high density of gas-cooled nuclear power plants, e.g., Benelux, Northern Germany or Southern England. Interestingly, we find that strong biomass burning events may also generate large $^{14}CO_2$ pulses because they liberate excess ^{14}C from the biosphere which had been assimilated after the nuclear tests. Therefore, it is important to also take biomass burning into account when using $\delta^{14}CO_2$ as a constraint of $ffCO_2$.

---

[1] Due to the structure of the Jena Carboscope and the computational resources available, we had to reduce the simulation domain from the whole European domain to 2˚W-16˚E, 47˚-55˚N in order to comply with the resolution requirements.

Surprisingly, even though Western Europe is not a region with strong biomass burning emissions (Europe as a whole only contributes with 0.2% of the global biomass burning emissions, van der Werf, et al., 2010), biomass burning dominates the CO signals across the Western European domain (171.41 ± 520.11 ppb). This overshadows the targeted fossil fuel combustion emissions (41.79 ± 79.22 ppb). Additionally, biofuel combustion emissions also produced non-negligible CO signals (10.44 ± 6.38 ppb). In contrast, biospheric and oceanic fluxes resulted in relatively minor signals over Western Europe (1.12 ± 0.72 and 0.003 ± 0.004 ppb respectively).

While at global scale, APO primarily reflects ocean biogeochemical processes and atmospheric transport processes, over the Western European domain, the atmospheric APO signals were derived from fossil fuel emissions (5.82 ± 14.37 ppm). Nevertheless, oceanic influences are not negligible near the coast (e.g. average signal magnitudes of 1.02, 0.84 and 0.79 ppm at DZI, WMS and ZWE respectively). Furthermore, although APO is a tracer that was designed to be conservative with respect biospheric fluxes, we observed that it has non-negligible contributions to the regional signal (average over the domain of 0.41 ± 0.22 ppm) because the oxidative ratios of photosynthesis and respiration (here from Clay and Worrall, 2015, see Tables 4-1 and 4-2 of D4.3) deviate from the -1.1 value that defines APO. In contrast, the biofuel and biomass burning APO signals are small (0.01 ± 0.01 and 0.2 ± 0.62 ppm respectively).

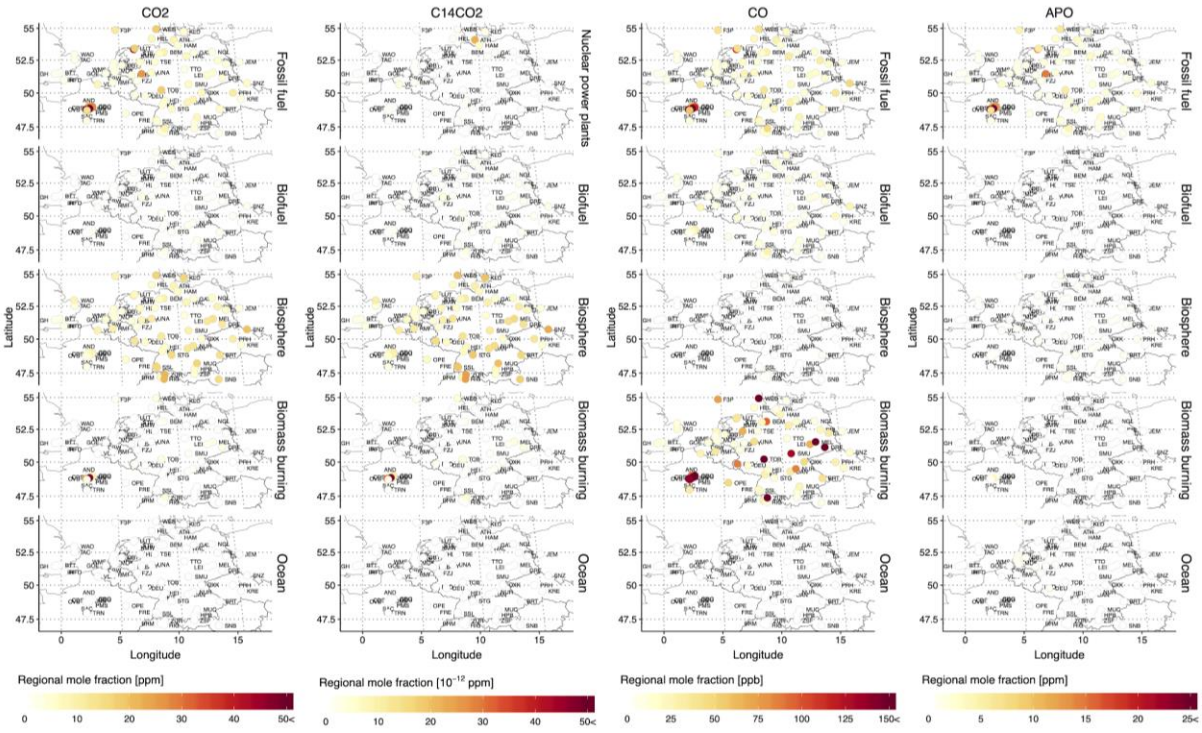

Figure 4-10 RMS amplitude of the tracer mole fraction at an hourly sampling site over the year 2015.

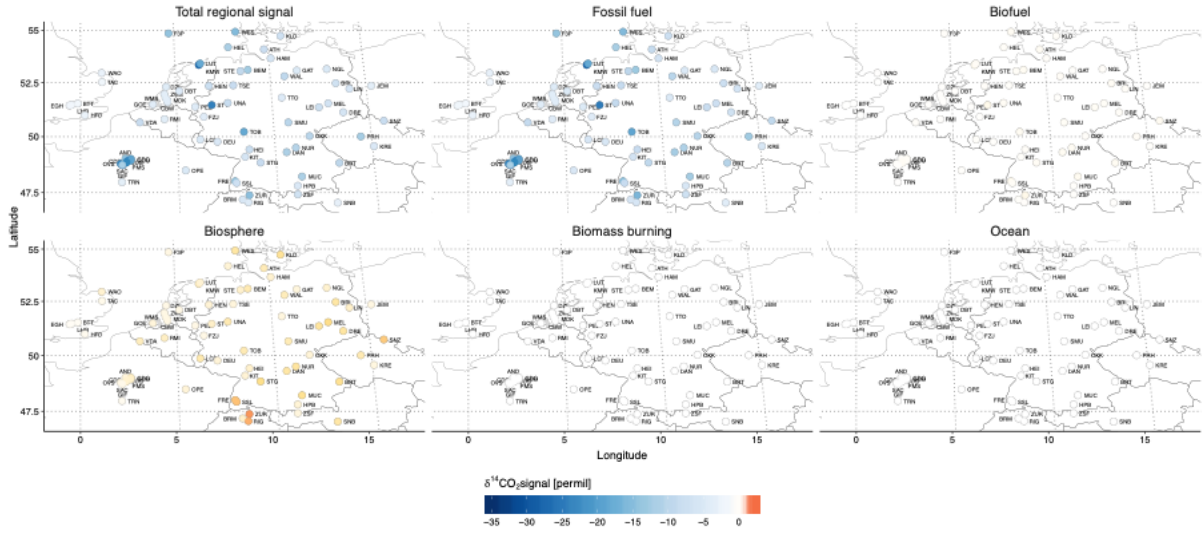

Figure 4-11 Average difference of the regional δ $^{14}CO_2$ signal with respect to the background δ$^{14}CO_2$ signal. The fossil fuel category includes both CO_2 emissions fossil fuel combustion and $^{14}CO_2$ emissions from nuclear power plants.

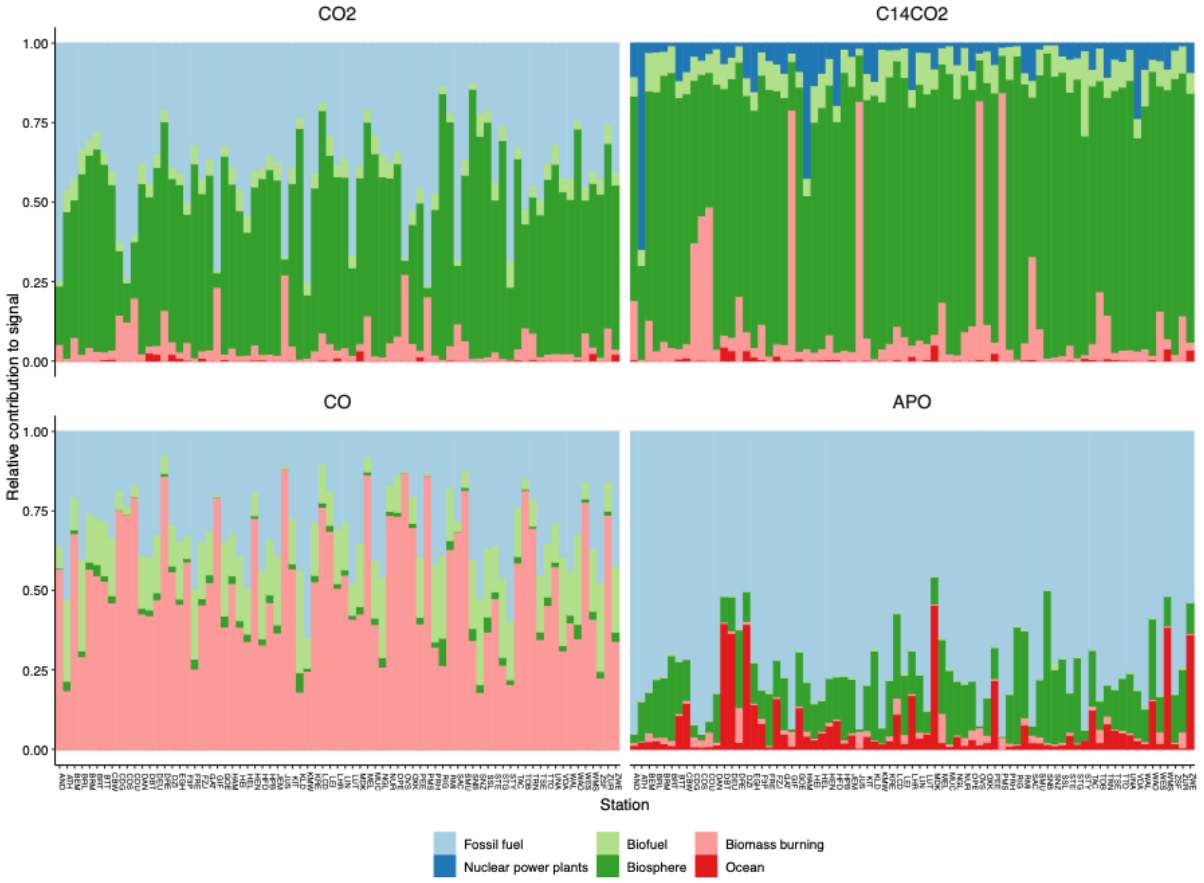

Figure 4-12 Relative of the tracer signal of each process at each station to the magnitude of the total regional signal in average over the year 2015.

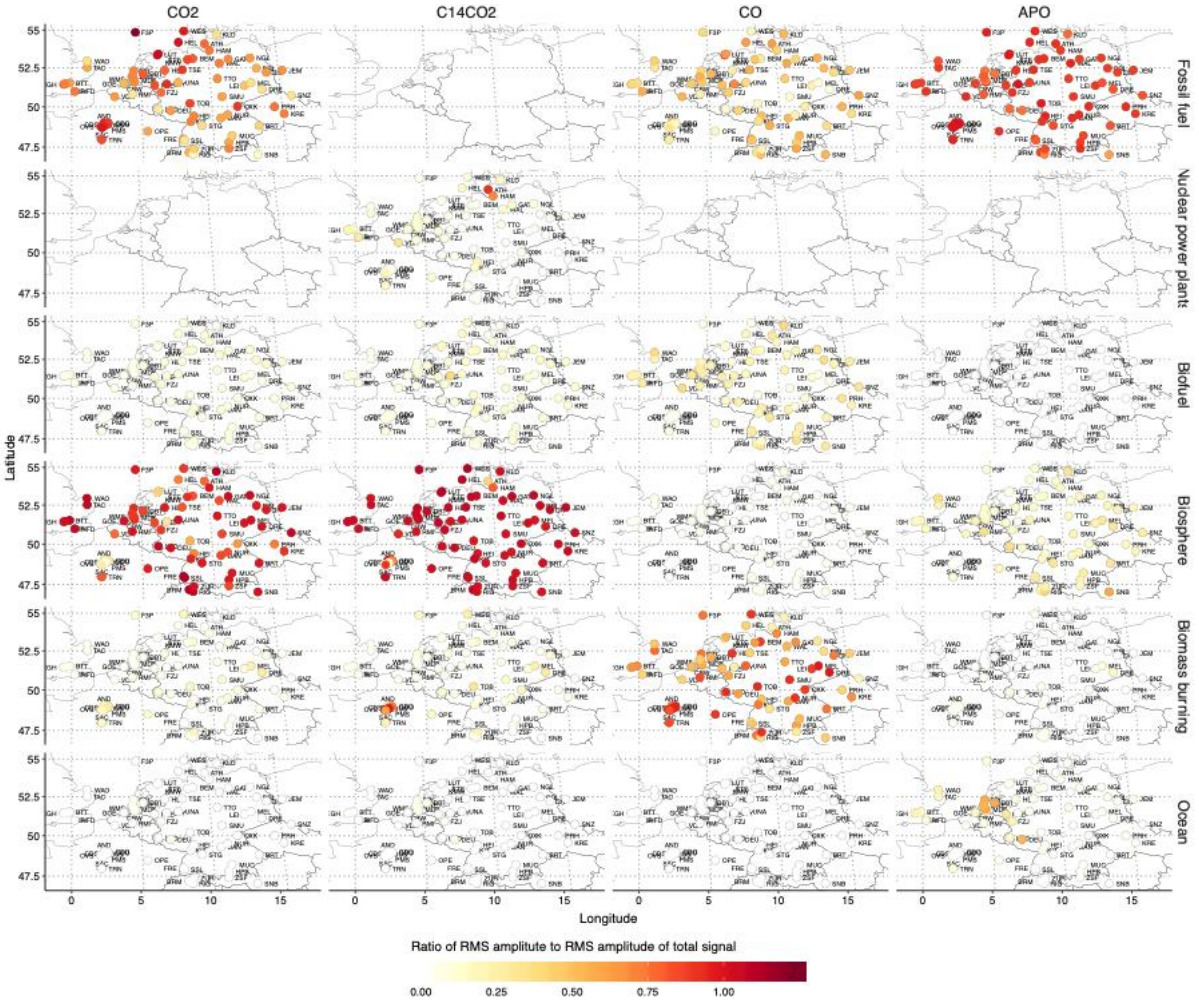

Figure 4-13 Geographical distribution of the ratio of the magnitude of signal each process *i* with respect to the total regional signal ($f = y_{rms,i}/y_{rms,tot}$).

4.2.2 Atmospheric fossil-fuel-derived CO_2 mole fraction

ffCO_2 has been estimated using the $\Delta^{14}CO_2$ signal (Levin and Karstens, 2007, Turnbull et al., 2006, 2009, Vogel et al., 2013, 2017), CO (Gamnitzer et al., 2006, Turnbull et al., 2006, Vogel et al., 2017, Levin et al. 2020), and APO data (Pickers, 2016). The ffCO_2 is calculated as:

$$ffCO_{2,\delta^{14}CO_2} = \frac{CO_{2,OBS}(\delta_{OBS}-\delta_{bg})}{\delta_{ff}-\delta_{bg}} - \frac{CO_{2,other}(\delta_{other}-\delta_{bg})}{\delta_{ff}-\delta_{bg}} \quad \text{(Eq. 4-2)}$$

$$ffCO_{2,CO} = \frac{CO_{OBS} - CO_{bg}}{R_{CO/CO_2}} \quad \text{(Eq. 4-3)}$$

$$ffCO_{2,APO} = \frac{APO_{OBS} - APO_{bg}}{R_{APO/CO_2}} \quad \text{(Eq. 4-4)}$$

where $R_{CO/CO2}$ and $R_{APO/CO2}$ are the fossil fuel combustion CO-to-CO_2 and APO-to-CO_2 ratios respectively, is the source signature of fossil fuel combustion (-1000 ‰) and *bg* refers to the background quantities (boundary conditions). In this study, we transport ffCO_2 as a separate tracer in one of our simulations. This includes fossil fuel combustion as well as non-

combustion emissions (e.g. cement production). Because of the use of a Lagrangian model, we can directly link a footprint to a measurement and directly link the fossil fuel CO, APO and CO_2 mole fraction to derive $R_{CO/CO2}$, $R_{APO/CO2,}$, and . Then, we directly tested how well the additional constraints of $\delta^{14}CO_2$, CO and APO may be used to reproduce the $ffCO_2$ tracer estimated by the STILT model (here referred to as $ffCO_{2,STILT}$, Figure 4-14).

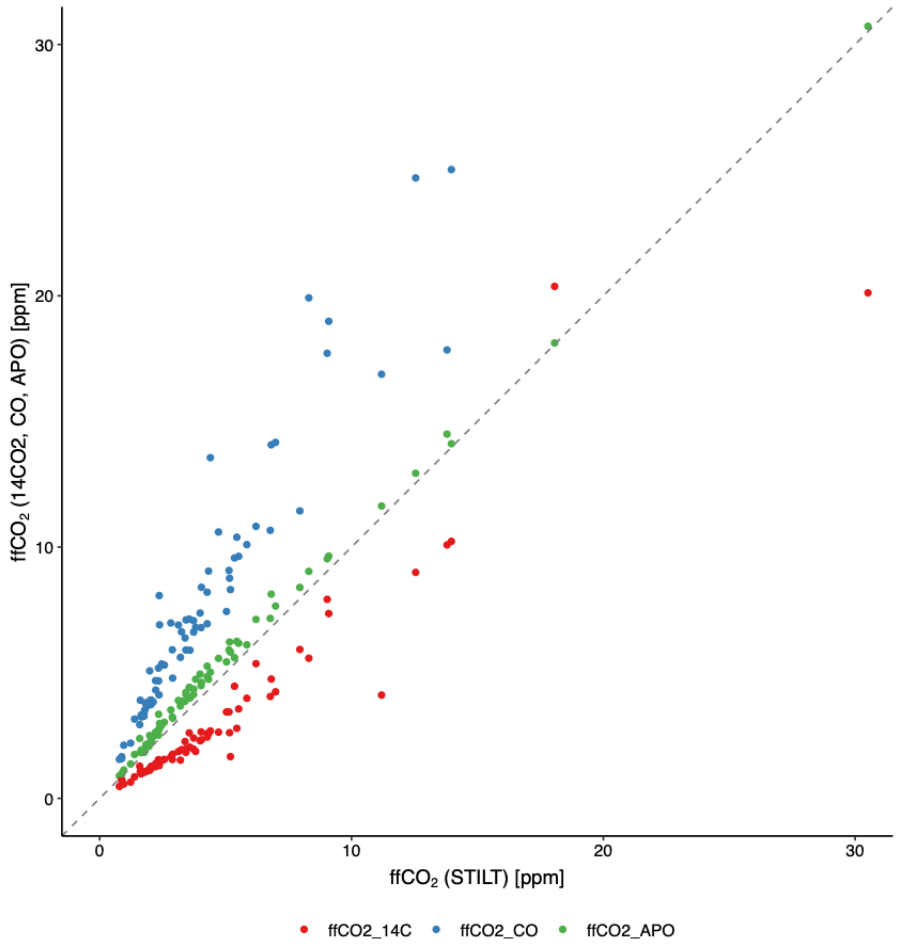

Figure 4-14 ffCO2 as estimated by STILT vs ffCO2 estimated by the additional tracers.

In Figure 4-15, the scenarios with the APO constraint ($ffCO_{2,APO}$) have the strongest correlation with $ffCO_{2,STILT}$ (R^2 = 0.98 ± 0.64) followed by the scenarios with the $\delta^{14}CO_2$ constraint ($ffCO_{2,\delta14CO2}$, R^2 = 0.89 ± 0.39). In contrast, the scenarios with the CO constraint show a much lower correlation (in average R^2 = 0.66 ± 0.36) because of the strong influence of the biomass mass burning emissions. In general, the correlation between $ffCO_{2,\delta14CO2}$, $ffCO_{2,CO}$ and $ffCO_{2,APO}$ with $ffCO_{2,STILT}$ decreases when other sources are present. For example, the correlation between $ffCO_{2,\delta14CO2}$ and $ffCO_{2,STILT}$ is lower at stations with a strong influence from nuclear power plants (e.g., R^2 = 0.11 and 0.35 at ATH and HAM respectively) or biomass burning (e.g., R^2 = 0.53 at PMS). As well, the correlation between $ffCO_{2,APO}$ and $ffCO_{2,STILT}$ decreases at stations near the shore, where ocean signals are important (e.g. R^2 = 0.79 and 0.82 at DZI and ZWE respectively).

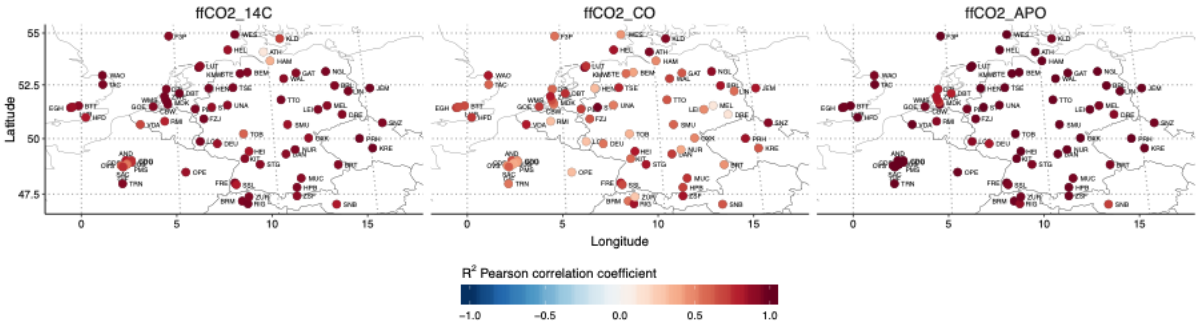

Figure 4-15: Pearson correlation of the $ffCO_2$ mole fraction calculated based on $^{14}CO_2$, CO or APO and different reference ratios against the $ffCO_2$ mole fraction estimated by the STILT model as an independent tracer.

Looking at the mismatch between $ffCO_{2,STILT}$ and $ffCO_{2,\delta14CO2}$, $ffCO_{2,CO}$ and $ffCO_{2,APO}$ (Figure 4-16 and 4-17), $ffCO_{2,APO}$ has the smallest error (in average an RMSE of 1.57 ± 1.50 ppm and a bias of 0.47 ± 0.29 ppm) followed by $ffCO_{2,\delta14CO2}$ (in average an RMSE of 8.94 ± 23.23 ppm and a bias of 1.93 ± 3.60 ppm). In contrast, $ffCO_{2,CO}$ has very large errors (on average an RMSE of 43.13 ± 118.89 ppm and a bias of -4.79 ± 6.62 ppm) because of the strong influence of the biomass mass burning emissions. As in the case of the correlations, $ffCO_{2,\delta14CO2}$, $ffCO_{2,CO}$ and $ffCO_{2,APO}$ had larger errors with respect to $ffCO_{2,STILT}$ if there were strong signals from other processes. For example, the error between $ffCO_{2,\ \delta14CO2}$ and $ffCO_{2,STILT}$ is much higher at stations with a strong influence from nuclear power plants (at ATH there is an RMSE of 19.02 ppm and a bias of 3.53 ppm) or biomass burning (at PMS there is an RMS of 176 ppm and a bias of 29.75). As well, the error between $ffCO_{2,APO}$ and $ffCO_{2,STILT}$ increases at stations near the shore, where ocean signals are important (at DZI there is a RMSE of 2.72 ppm).

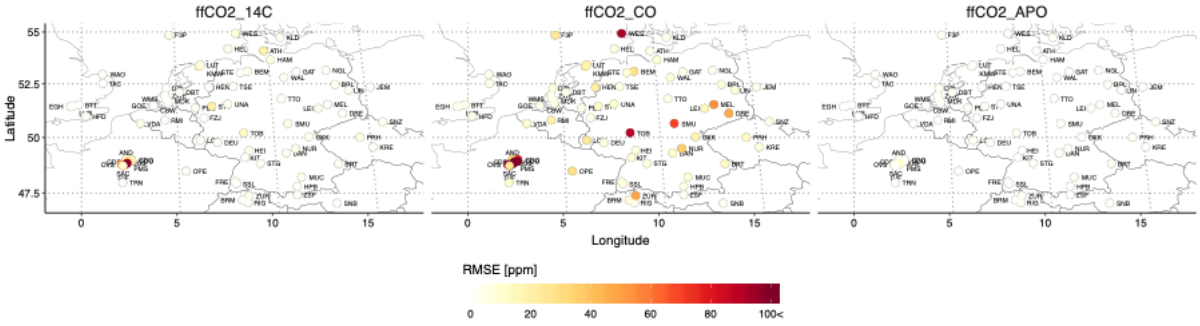

Figure 4-16 RMSE between $ffCO_2$ mole fraction calculated based on $\delta^{14}CO_2$, CO or APO and different reference ratios against the $ffCO_2$ mole fraction estimated by the STILT model as an independent tracer.

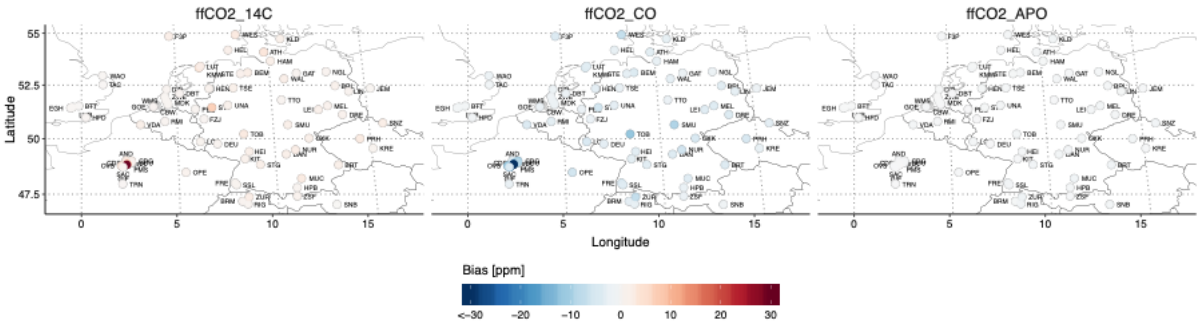

Figure 4-17 Mean error (bias) between ffCO2 mole fraction calculated based on δ^{14}CO2, CO or APO and different reference ratios against the ffCO2 mole fraction estimated by the STILT model as an independent tracer.

4.2.3 Rural-urban atmospheric gradients

Given that 70% of fossil fuel CO_2 emissions occur in cities and that the atmospheric inverse modelling technique exploits the spatial and temporal gradients between measurements to estimate spatiotemporal flux patterns, in this section, we explore the size of these atmospheric gradients at two locations, which had been analysed in previous studies, in more detail.

4.2.3.1 Paris region

To analyse the atmospheric gradients around the Paris urban area, we shall focus on the stations CDS and SAC which have been identified as lying often upwind/downwind from each other (Breon et al., 2015, Staufer et al., 2016 and Lian et al., 2020). SAC is located in a semi-urban area with a mixture of crops and forest in the periphery of Paris, while CDS is in the centre of the city. Due to the larger contribution of anthropogenic emissions at CDS, the average magnitude of the fossil fuel signal increased from 13.88 ppm to 40.09 ppm (Figure 4-18), the $\delta^{14}CO_2$ signal decreased from an average -12.10 to -25.87 ‰, the magnitude of the CO fossil fuel signal increased from 56.44 to 124.29 ppb and the APO fossil fuel signal decreased from an average of -6.50 to -19.55 ppm.

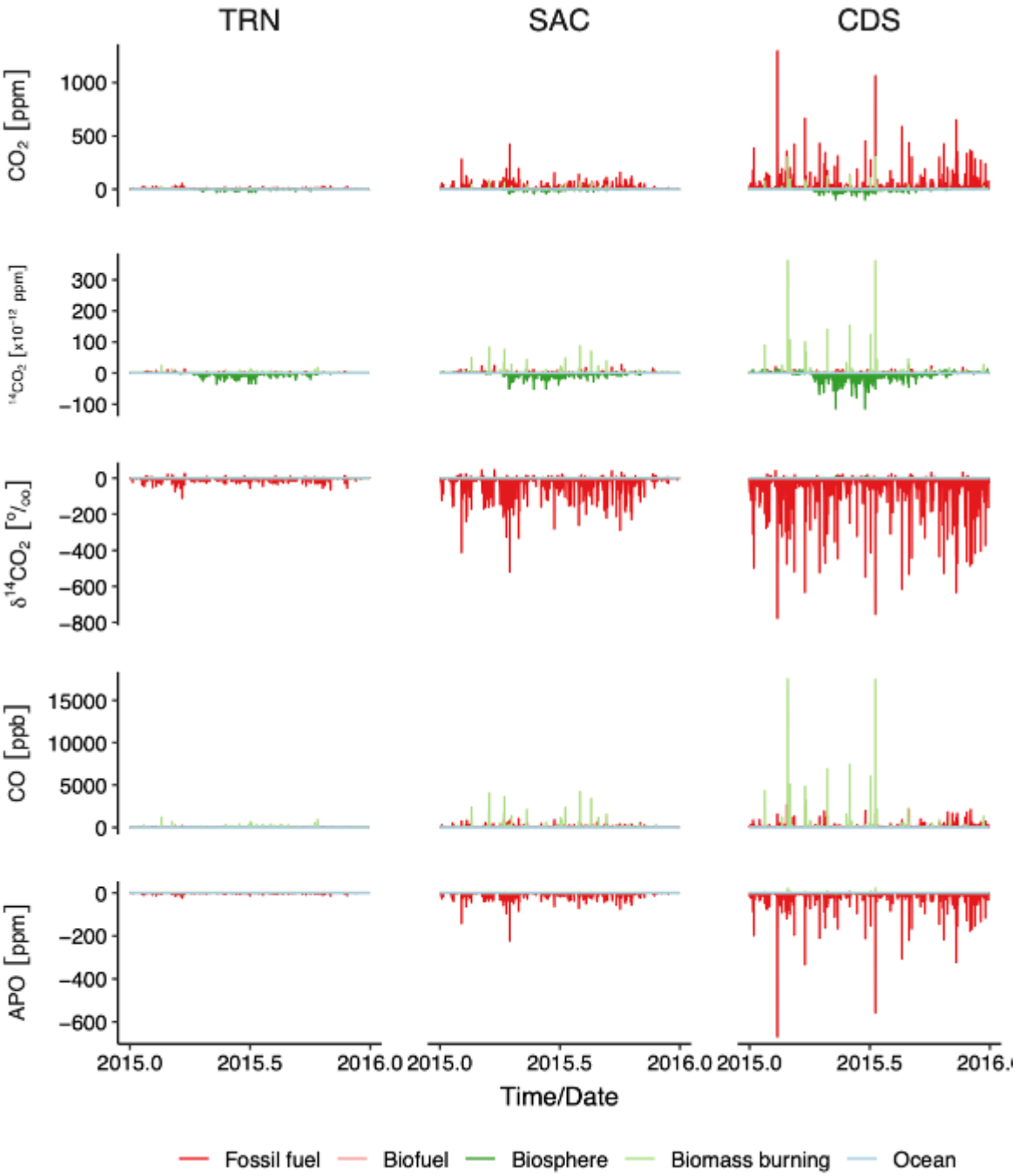

Figure 4-18 Contribution of flux processes to regional signal sampled at stations TRN (Trainou, 47.96˚N, 2.11˚E), SAC (Saclay, 48.72˚N, 2.14˚E) and CDS (Cité des Sciences et de l'Industrie, 49.00˚N, 2.39˚E) of the different tracers. The fossil fuel process includes $^{14}CO_2$ emissions from nuclear power plants. TRN is not directly upwind-downwind from Paris but represents more background conditions.

Calculating the fossil fraction at the stations around Paris we find that $ffCO_2$ increases from TRN to SAC to CDS similarly to the tagged tracer from STILT (figure 4-19). The strongest correlation at all three stations was achieved when using the APO measurements (all R^2 > 0.98, figure 4-15). The $ffCO_2$ obtained from the $\delta^{14}CO_2$ measurements did not achieve such a strong correlation because of the interference of emissions from nuclear power plants, biosphere and biomass burning (on average 0.84, 5.23 and 3.85 $x10^{-12}$ ppm $^{14}CO_2$ respectively). The $ffCO_2$ obtained based on CO measurements only achieved a moderate correlation (R^2 = 0.41).

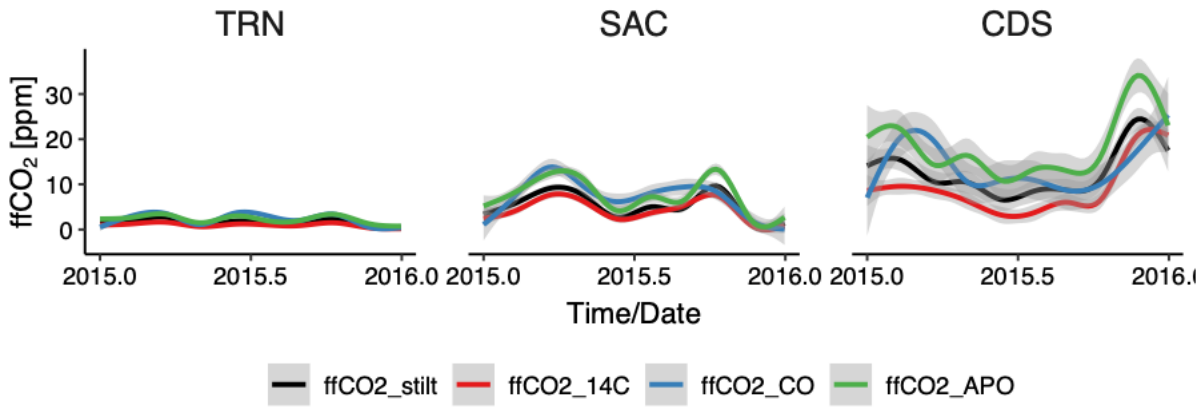

Figure 4-19 Smoothed yearly variations of $ffCO_2$ observed at TRN, SAC and CDS as calculated by the STILT modelled (tagged tracer) or with the use of the δ14CO2, CO or APO signal (only median ratio shown).

Looking at the hourly gradients between CDS and SAC (figure 4-20), we found a higher CO_2 mole fraction (in average by 6.63 ± 43.38 ppm), a more negative of the $\delta^{14}CO_2$ signal (in average -by 13.53 ± 60.45 ‰), a higher in CO mole fraction (in average by 35.13 ± 456.03 ppb) and a more negative in the APO signal (in average by -3.37 ± 19.85 ppm). For CO, we observed a relatively more important contribution from biomass burning (in average 12.13 ± 411.48 ppb). Furthermore, although SAC is located near crops and forest, the contribution of the plant uptake is negligible during the daytime even during the growing season compared to fossil fuels (-0.35 ± 2.53 ppm in comparison to 1.15 ± 4.83 ppm respectively).

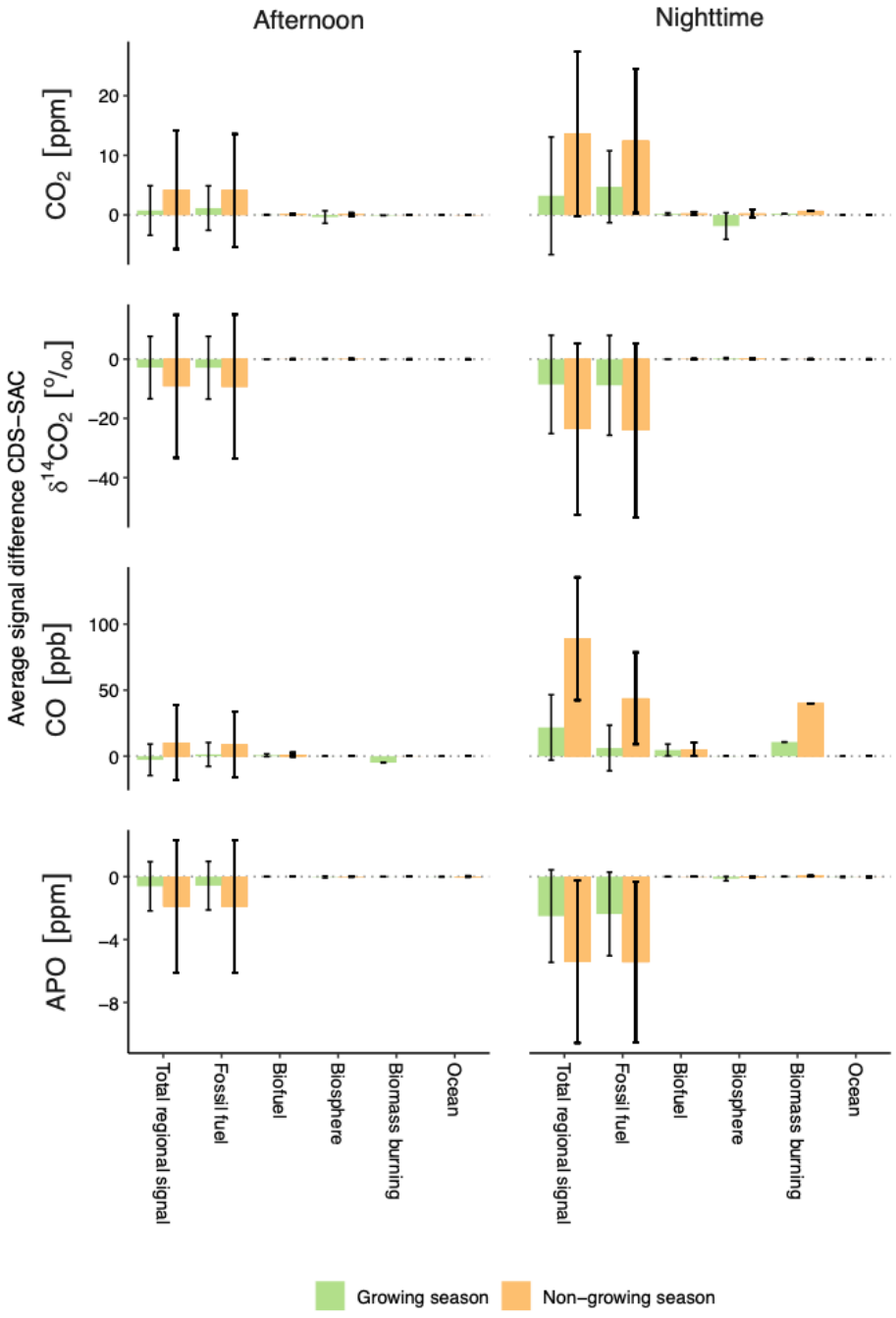

Figure 4-20 Contribution of the different flux processes to the tracer gradient between CDS and SAC. Error bars represent the interquartile range.

We use the gradient between CDS and SAC, to evaluate the $ffCO_2$ calculated using the additional tracers against the $ffCO_2$ estimated as an independent tracer in the STILT model (Figure 4-21 and Table 4-1). The $ffCO_2$ gradient CDS and SAC determined by $\delta^{14}CO_2$ had a strong correlation with $ffCO_2$ gradient estimated by the STILT model (average R^2 = 0.8064) and relatively low error (RMSE = 13.31 ppm). Nevertheless, while $\delta^{14}CO_2$ observations are considered the standard to determine $ffCO_2$, $ffCO_2$ derived from APO had the best performance correlating strongly with the $ffCO_2$ estimated by STILT (R^2 = 0.9924) and having a relatively low error (RMSE = 10.47 ppm). Interestingly, $ffCO_2$derived from $\delta^{14}CO_2$ tends to have a positive bias (average of 2.14 ppm), while $ffCO_2$ derived from APO tends to have a negative bias (average of -2.89 ppm). Therefore, it is important to have accurate oxidative

ratios to avoid biases. $ffCO_2$ derived from CO has the worst performance with a low correlation (average R^2 = 0.41) and high errors (RMSE = 44.01 ppm). $ffCO_2$ derived from CO measurements has strong deviations at the time of biomass burning events. The ability to estimate $ffCO_2$ is also strongly affected by meteorological conditions, with less error in case of a well-mixed boundary layer found during the afternoon particularly during the growing season.

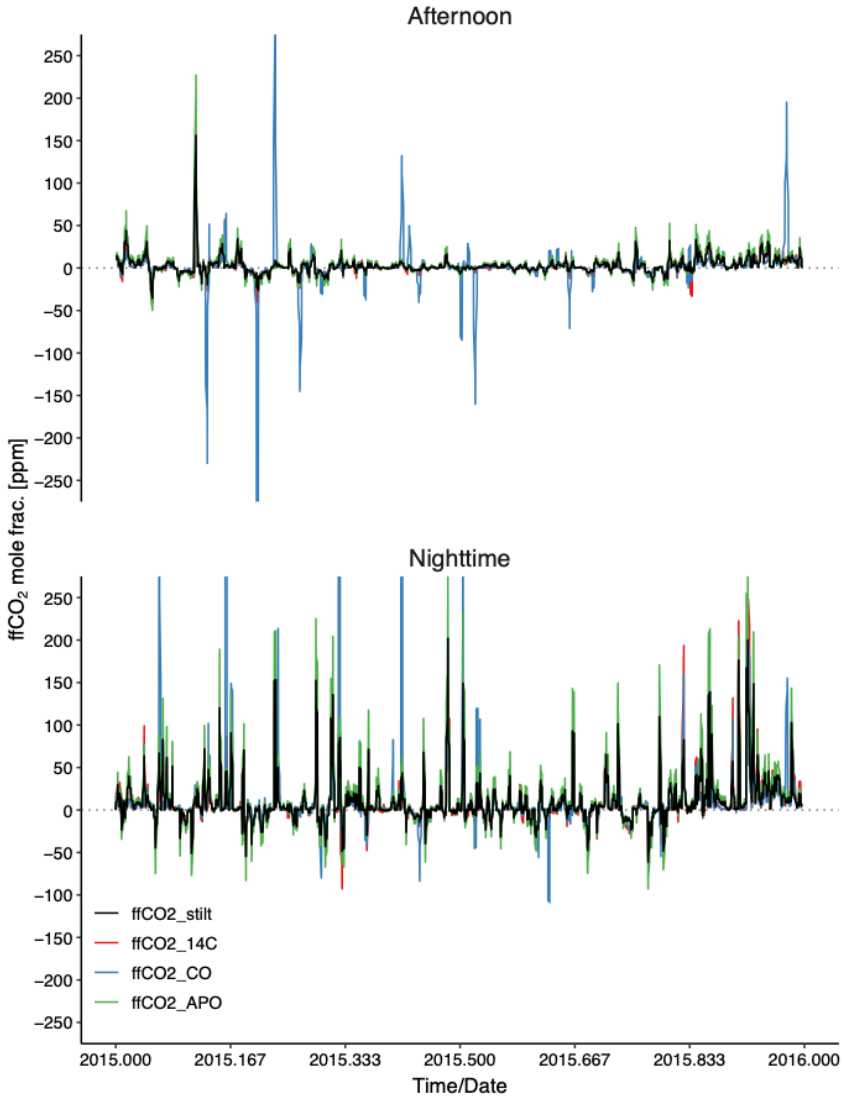

Figure 4-21 ffCO2 daily afternoon (11:00 – 16:00) and night time (23:00 – 5:00) averages the difference between CDS-SAC as calculated by the different tracers in comparison to STILT tracer.

Table 4-1 Summary of metrics for the ffCO2 gradient between CDS-SAC

Case	Season	Time of the day	Correlation R^2	RMSE [ppm]	Bias [ppm]

$^{14}CO_2$	Growing	Afternoon	0.8086	2.35	0.97
	Growing	Nighttime	0.8172	13.03	3.79
	Non-growing	Afternoon	0.8791	6.65	2.02
	Non-growing	Nighttime	0.7948	18.82	1.59
	Overall		0.8064	13.31	2.14
CO	Growing	Afternoon	0.3333	17.72	1.67
	Growing	Nighttime	0.5627	26.86	0.70
	Non-growing	Afternoon	0.3702	32.47	2.21
	Non-growing	Nighttime	0.3745	64.75	-4.06
	Overall		0.4149	44.01	-0.44
APO	Growing	Afternoon	0.9875	1.84	-0.78
	Growing	Nighttime	0.9962	11.28	-3.10
	Non-growing	Afternoon	0.9954	6.21	-1.77
	Non-growing	Nighttime	0.9911	13.98	-4.51
	Overall		0.9924	10.47	-2.89
Summary	Growing	Afternoon	0.8704	7.31	0.62
	Growing	Nighttime	0.9274	17.06	0.46

	Non-growing	**Afternoon**	**0.9213**	**15.11**	**0.82**
	Non-growing	**Nighttime**	**0.8839**	**32.52**	**-2.33**

4.2.3.2 Rotterdam region

Super et al. (2017) tested the use CO_2 and CO mole fraction continuous measurements in a simple network to constrain the fossil fuel emissions from the city of Rotterdam, Netherlands. This network consisted of an upwind station (Westmaas, WMS, 51.78˚N, 4.45˚E) and a downwind station (Zweth, ZWE, 51.96˚N, 4.39˚E). We expand here the analyses of Super et al. (2017) with our simulation to determine the signal strength and gradients between the stations.

In contrast to Paris, the regional signal observed at WMS and ZWE is much smaller (regional signal magnitude of 4.41 and 4.54 ppm respectively, see figure 4-22). The regional CO_2 signal is dominated by biosphere fluxes and anthropogenic emissions (average ratio of the magnitude of the process signal with respect to the total signal was 0.9 and 0.705 respectively). The additional tracers have significant interference from processes besides fossil fuel emissions and biospheric fluxes. Due to the location, the $^{14}CO_2$ signal had a non-negligible contribution from nuclear power plant emissions (magnitudes of 0.48 and ppm at WMS and ZWE respectively). When looking at the CO signal, there are strong fossil and biofuel signals (5.26 and 10.20 ppb respectively) year-round but also strong intermittent biomass burning signals (magnitude of 9.76 ppb). In the case of APO, there was a strong contribution from oceanic fluxes which more than offset the oxygen consumption from fossil fuel emissions during the summer. Due to this interference, the $ffCO_2$ derived from APO had unrealistic seasonal patterns (figure 4-23).

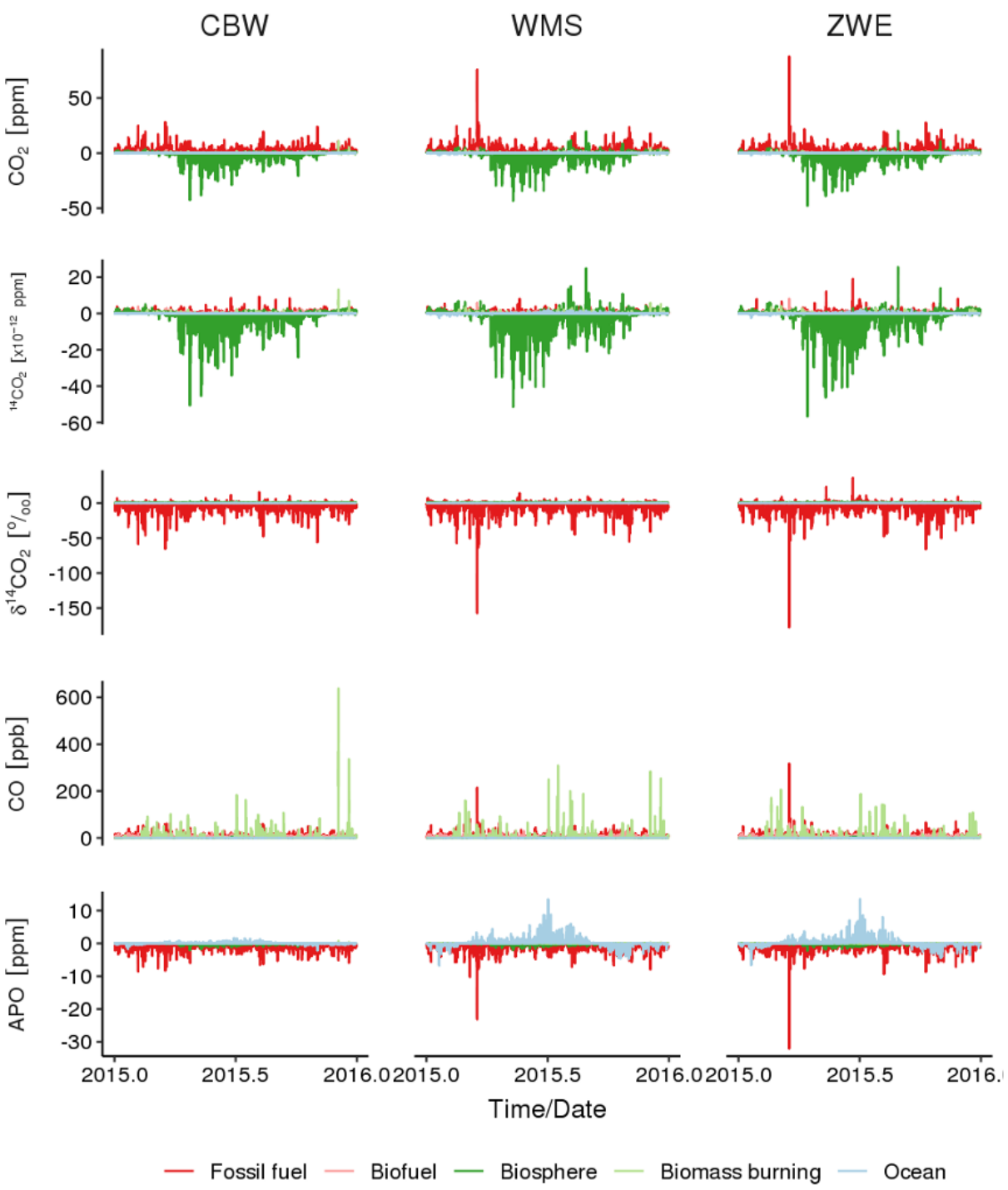

Figure 4-22 Contribution of flux processes to regional signal sampled at stations CBW (Cabauw, 51.58˚N, 4.55˚E), ZWE (Zweth, 51.96˚N, 4.39˚E) and WMS (Westmaas, 51.78˚N, 4.45˚E) of the different tracers. The fossil fuel process includes $^{14}CO_2$emissions from nuclear power plants.

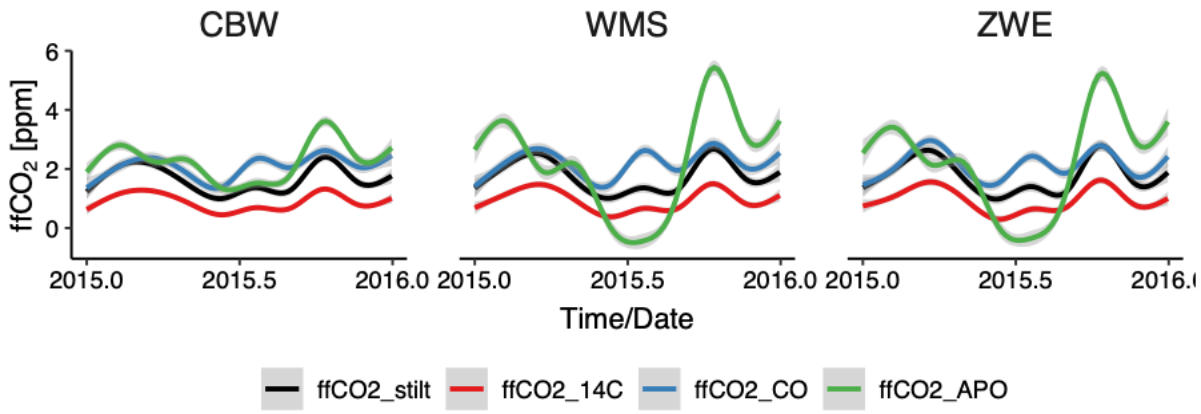

Figure 4-23 Smoothed yearly variations of $ffCO_2$ observed at CBW, WMS and ZWE as calculated by the STILT modelled (tagged tracer) or with the use of the $\delta^{14}CO_2$, CO or APO signal.

In contrast to CDS and SAC in Paris, ZWE and WMS alternated their role as upwind and downwind stations rather equally. This means that the mean gradient was close to zero and the spread around this mean was relatively symmetric (Figure 4-24). When we observed the gradient in $ffCO_2$ (Figure 4-25), the size of the gradient estimated by STILT was of 0.06 ± 1.05 and -0.07 ± 1.62 ppm in the growing and non-growing seasons respectively, which would be difficult to detect given the measurement and modelling uncertainty assumed in this study (0.1 and 1 ppm respectively). During the summer, there was a stronger oceanic APO signal at WMS primarily during the night-time (up to -0.08 ± 0.79 ppm). This oceanic signal very clearly interfered with the estimation of $ffCO_2$ and the correlation of the $ffCO_{2,stilt}$ with $ffCO_{2,APO}$ decreased from R^2 = 0.8952 to 0.5357 between the afternoon and the night-time (Table 4-2).

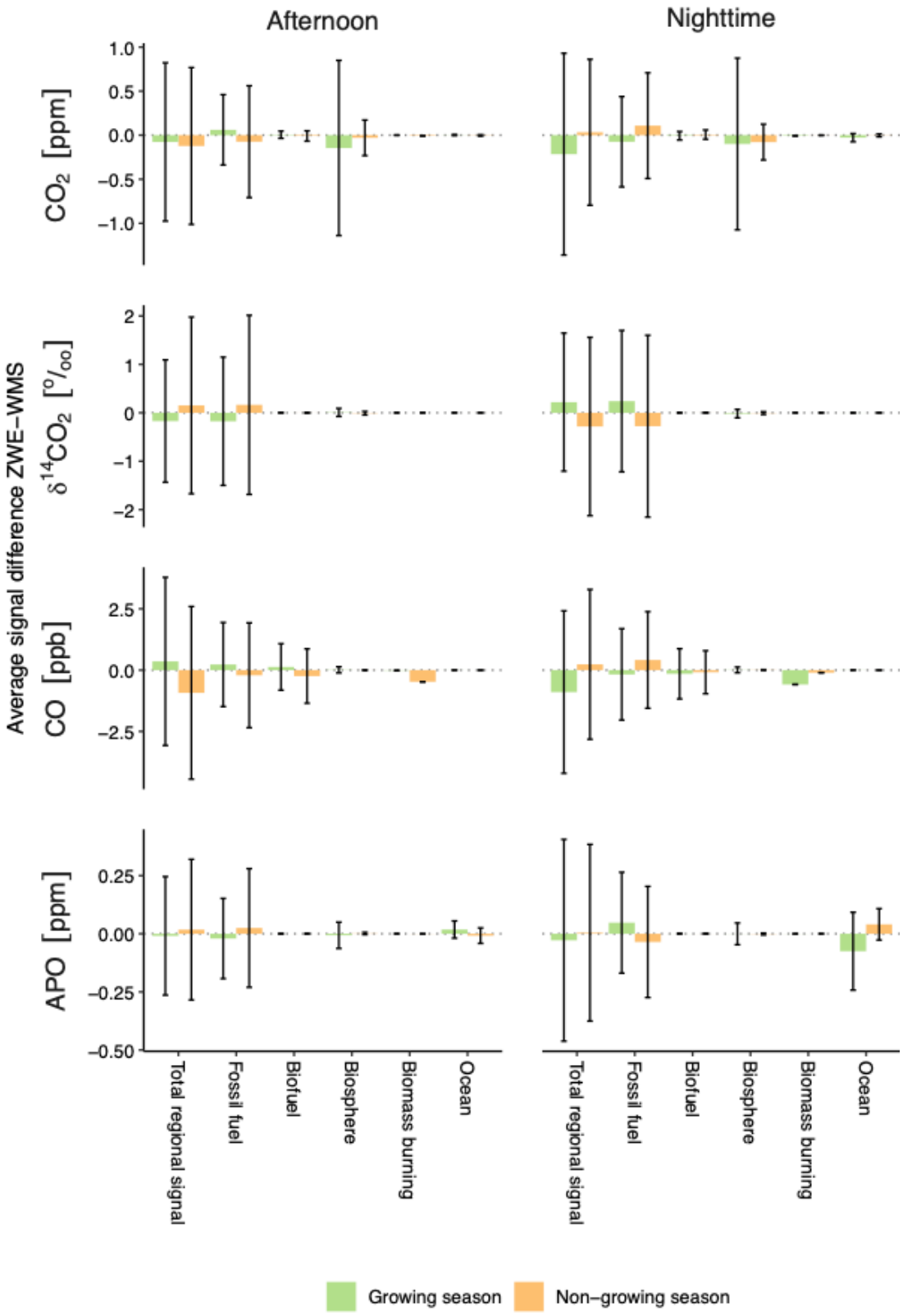

Figure 4-24 Mean gradient between ZWE and WMS for the different tracers and processes.

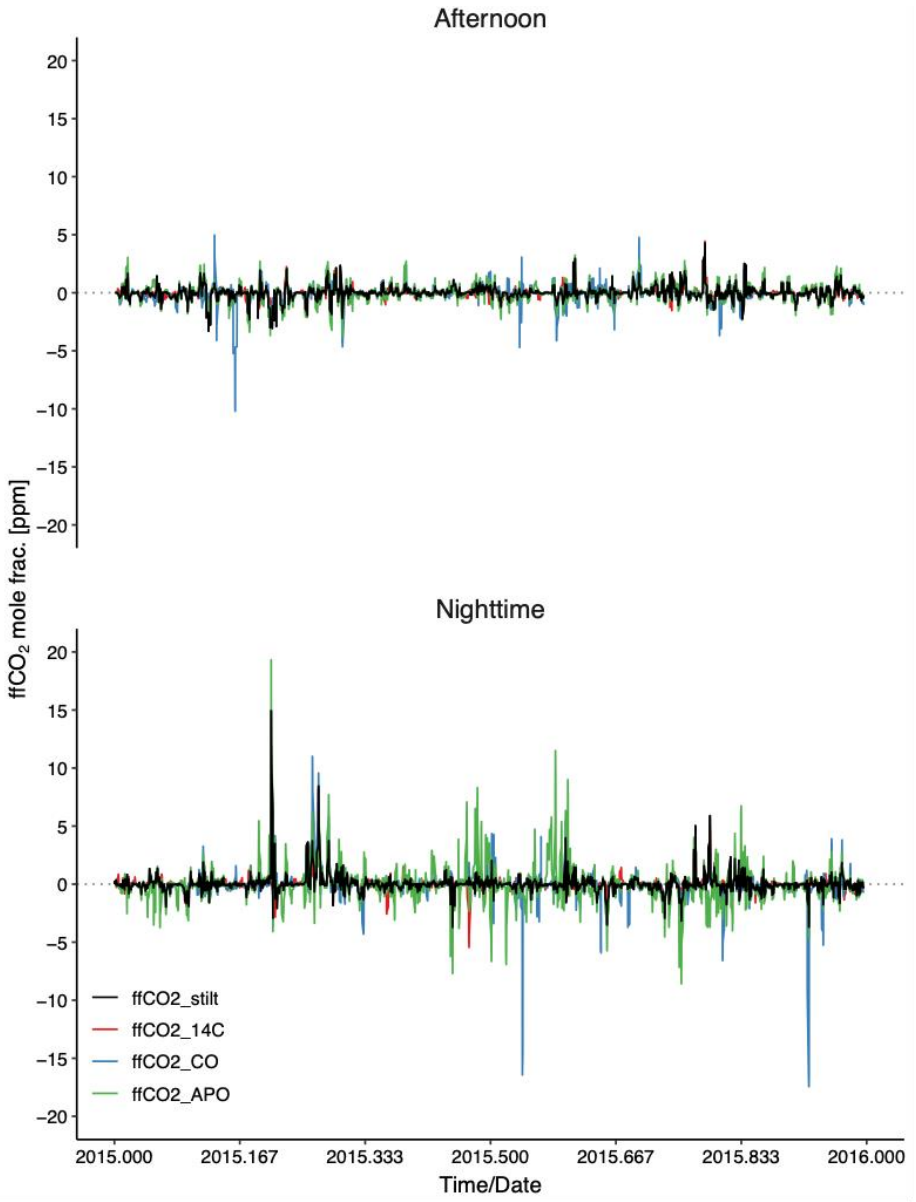

Figure 4-25 Afternoon (11-16 h, *top*) and night time (23-05 h, *bottom*) $ffCO_2$ gradient between ZWE and WMS.

Table 4-2 Summary of metrics for the $ffCO_2$ gradient between ZWE-WMS

Case	Season	Time of the day	Correlation R^2	RMSE [ppm]	Bias [ppm]
$^{14}CO_2$	Growing	Afternoon	0.6758	0.31	0.02
	Growing	Nighttime	0.5578	0.52	-0.02

	Non-growing	Afternoon	0.8737	0.38	-0.06
	Non-growing	Nighttime	0.9320	0.44	0.01
	Overall		0.8527	0.43	-0.01
CO	Growing	Afternoon	0.5890	0.58	-0.01
	Growing	Nighttime	0.4916	1.18	0.09
	Non-growing	Afternoon	0.6031	0.78	0.10
	Non-growing	Nighttime	0.7019	1.09	0.06
	Overall		0.6265	0.98	0.07
APO	Growing	Afternoon	0.8952	0.34	0.03
	Growing	Nighttime	0.5357	1.64	-0.16
	Non-growing	Afternoon	0.8957	0.40	-0.02
	Non-growing	Nighttime	0.7349	1.13	0.12
	Overall		0.6659	1.09	0.01
Summary	Growing	Afternoon	0.7538	0.41	0.02
	Growing	Nighttime	0.5290	1.11	0.03
	Non-growing	Afternoon	0.8228	0.52	0.01
	Non-growing	Nighttime	0.8214	0.89	0.07

4.3 Inverse assessment

4.3.1 Uncertainty reduction

To evaluate the ability of our inverse model to constrain the fluxes in a particular location by the observations, we analysed the reduction of uncertainty between *a priori* and *a posteriori* fluxes for an inversion driven only by CO_2 measurements, CO_2 and $^{14}CO_2$ measurements, CO_2 and CO measurements and CO_2 and APO measurement. Due to the fact that the *a priori* flux uncertainty as well as the measurement and model uncertainties are rather arbitrary, the *a posteriori* uncertainty only has a meaning in relation to the corresponding *a priori* uncertainties. The uncertainty reduction $\Delta\sigma$ is expressed as

$$\Delta\sigma = 1 - \frac{\sigma_{post}}{\sigma_{prior}} \qquad \text{(Eq. 4-5)}$$

where σ_{prior} and σ_{post} are the *a priori* and *a posteriori* uncertainty respectively. A value of zero indicates that a location is only determined by the *a priori* flux, while a value of one would correspond to a hypothetical complete constraining of the result by the data (Rödenbeck et al. 2003).

Here we calculated the integrated uncertainty reduction of hourly fluxes over the year 2015 for a set of regions described in D4.3. Before proceeding, we must make it clear that due to computational resources and time much of the original plans described in D4.3 could not be realized. Since the STILT model is Lagrangian, the computational requirements increase with the number of measurement points. Therefore, we only performed simulations with the actual ICOS network distribution. Furthermore, it was only possible to use a maximum of two tracers at a time. Additionally, we were not able to optimize the measurements on a gridcell basis with a certain spatial correlation length to its neighbours but we were forced to optimize the fluxes on the scale of the uncertainty integration regions. Finally, in contrast to the previous section, where we sampled the $^{14}CO_2$ mole fraction at hourly time steps to understand the variability of the signals, in this section, only one $^{14}CO_2$ sample per week is taken to simulate a flask measurement. This is done at 14 h UTC for low altitude stations and 23 h UTC for high altitude mountain stations (when the station is above the planetary boundary layer). The other tracers are sampled at hourly time steps. To harmonize the contribution of hourly and weekly samples to the cost function, the Jena Carboscope de-weights the hourly samples, such that they have the same weight as a weekly sample but maintain the temporal information.

The reduction of uncertainty analysis indicates that CO_2 fluxes over the Western European domain are reasonably well constrained with overall reduction over 88% (Table 4-3). This is mainly driven by the other flux processes, while the uncertainty of fossil fuel emissions was reduced by over 84%. At the level of the entire Western European domain the use of the additional constraints only increased the uncertainty reduction marginally.

Table 4-3 Overall uncertainty reduction for the entire Western European domain (obtained by a weighted sum of squares, where the weights were the fluxes).

Constraints	Fossil fuel emissions	Other fluxes	Overall reduction
CO_2 only	0.8427	0.8810	0.8808

CO_2 +$^{14}CO_2$	0.8450	0.8970	0.8968
CO_2 +CO	0.8443	0.8813	0.8812
CO_2 +APO	0.8438	0.8812	0.8810

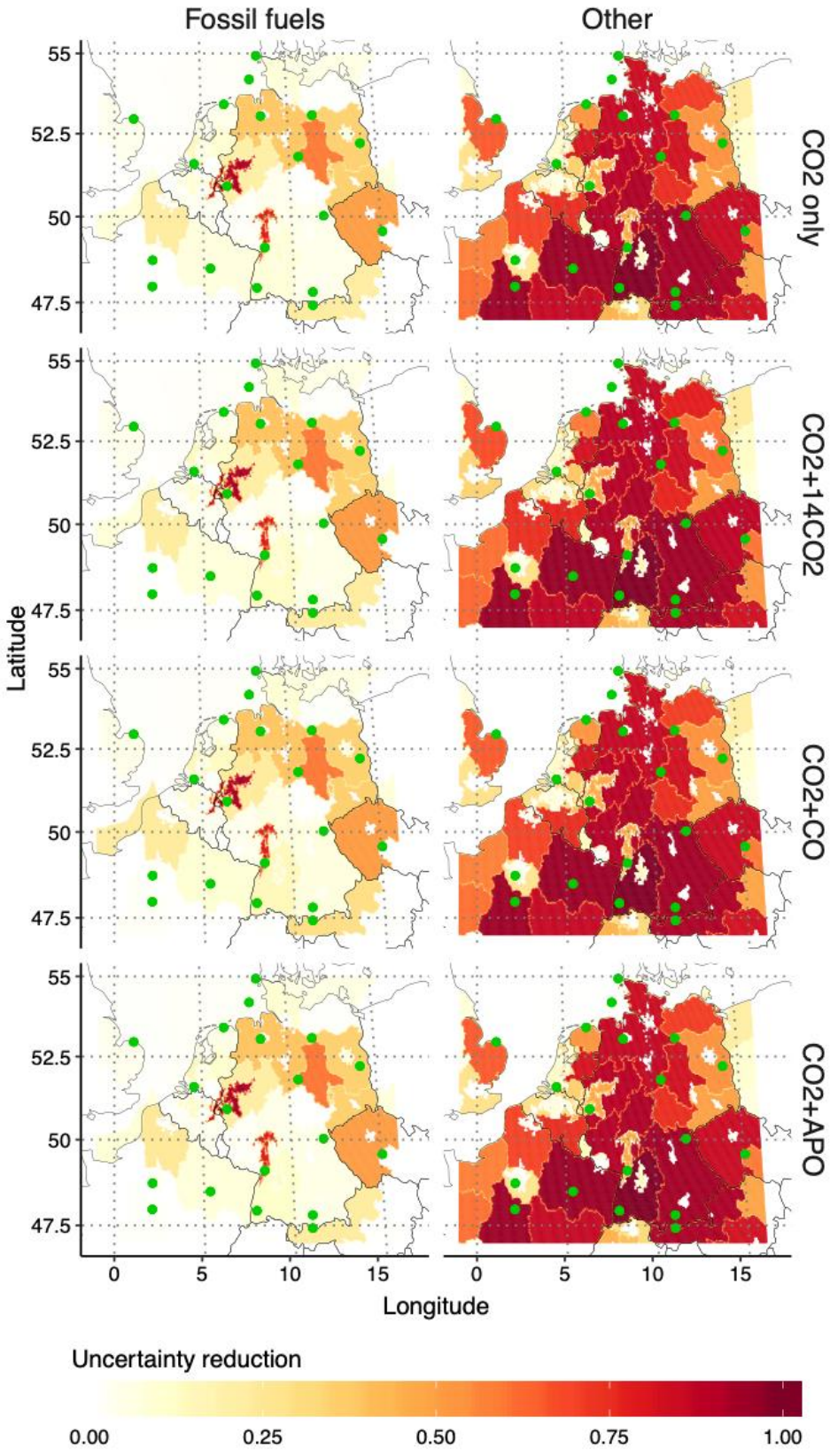

Figure 4-26 Uncertainty reduction in the yearly fluxes per integration region for each scenario. Green dots represent measurement stations.

For fossil fuels, the uncertainty reduction is concentrated over the Rhine-Ruhr and the Frankfurt-Rhein-Main urban areas (92.5 and 79.2 % respectively), which are constrained by the nearby FZJ (Forschungszentrum Jülich, 50.91˚N, 6.41˚E) and KIT (Karlsruhe Institute of technology, 49.09˚N, 8.43˚E) stations respectively (Figures 4-26 and 4-28). Medium uncertainty reduction is reached across Northern Germany up to Bohemia in the Czech Republic. Strikingly for most urban areas, except those mentioned above and Leipzig (41% reduction), the uncertainty reduction of fossil fuel emissions is rather low, e.g., 12, 11, 9, 2.8, 1, and 0.4 % for Stuttgart, the Flemish diamond, Berlin, Paris, Hamburg and Prague respectively.

For the category “other fluxes", the uncertainty reduction is higher across Central France (Centre and Grand-Est regions, 94.6 and 94.3 % respectively), Southern Germany (Baden Wurttemberg, Bavaria, 99.2 and 93 % respectively), Eastern Austria (91.4 %) up to Northern Germany (Lower Saxony and Schleswig-Holstein, with 86.4 and 84.2 % respectively) and Bohemia in the Czech Republic (85 %), Strikingly, for the urban areas, even within the regions mentioned above, the uncertainty reduction was only 13.88 ± 0.13 % in average. Peripheral regions also have lower uncertainty reduction because they are not constrained by gradients between upwind and downwind stations.

The use of additional tracer only marginally increased the uncertainty reduction. The strongest increase was by $^{14}CO_2$ (over the whole domain only by 1.6 percentage points). Strikingly, the uncertainty reduction increased more for the other fluxes than for the fossil fuel emissions with the $^{14}CO_2$ constraint (increase of 1.6 in contrast to 0.23 percentage points, Figure 4-27). However, looking back at Figures 4-18 and 4-22, we can observe that biospheric fluxes were a very dominant contributor to the $^{14}CO_2$ mole fraction, which is what we actually are optimizing for because the Jena Carboscope is strictly linear. Moreover, the $^{14}CO_2$ also increased (although marginally) the uncertainty reduction for fossil over Southern Germany (increase of 3.35 and 0.9 percentage points for Baden-Wurttemberg and Bavaria respectively), Bohemia (1.36 percentage points increase) and Lower Saxony (1.43 percentage points increase). Surprisingly, for fossil fuel emissions, the CO constraint provided the strongest gain in uncertainty reduction especially in the French part of the English Channel (13.81 percentage points), and Southern Germany (6.68 and 2.42 percentage points for Baden-Wurttemberg and Bavaria respectively). In the case of APO, the added an average 0.9 percentage points to the uncertainty reduction of fossil fuel emissions in Eastern France, Benelux, and Western Germany (maximum of 2.9 and 2.1 percentage points in Baden-Wurttemberg and Haus-de-France respectively).

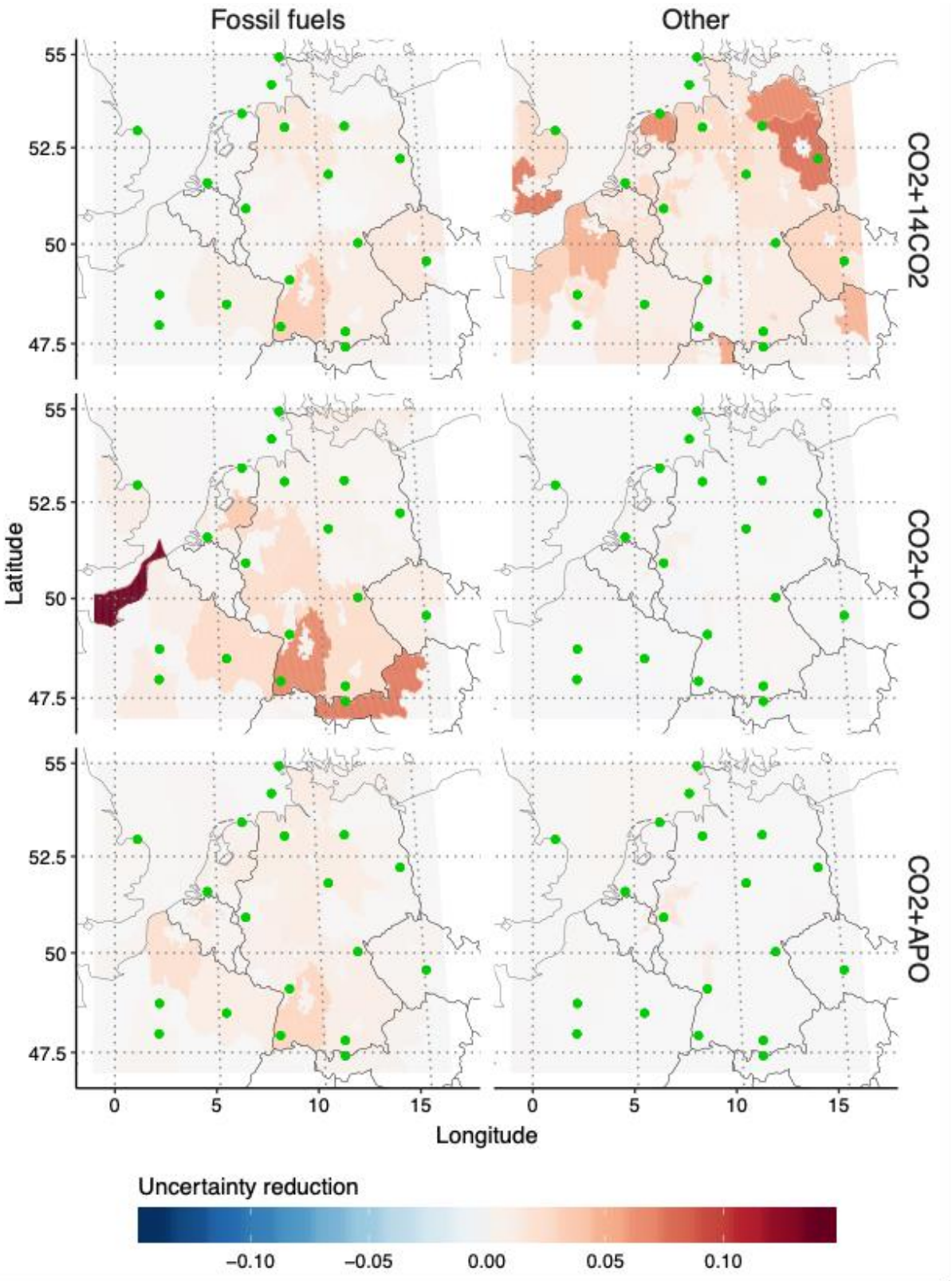

Figure 4-27 Difference in uncertainty reduction of the yearly fluxes with respect to the CO2 only scenario. Red colours mean the uncertainty reduction increases. Green dots represent the measurement stations.

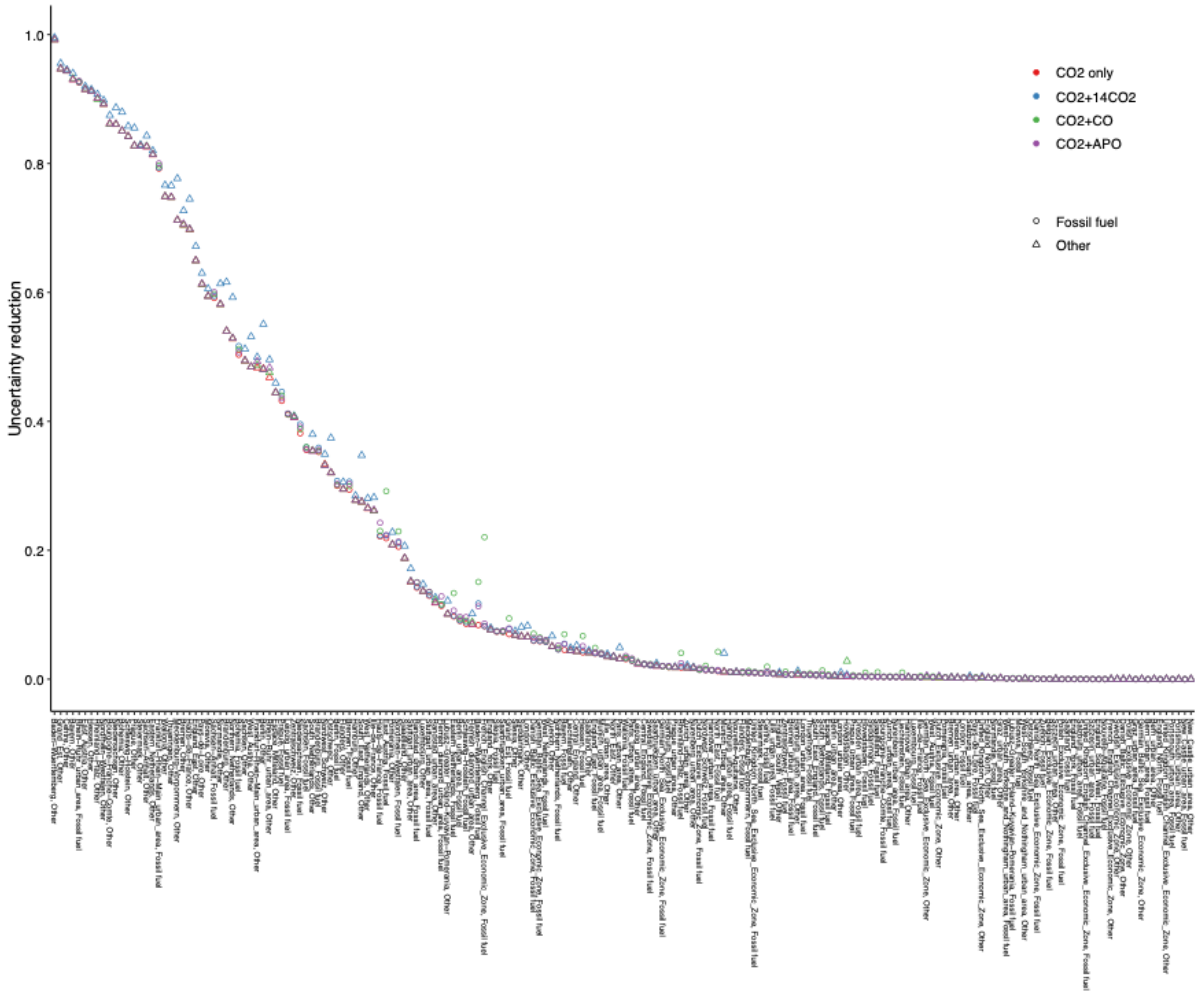

Figure 4-28 Uncertainty reduction of the yearly fluxes ordered from highest to lowest contrasting the effect of the additional constraints.

4.3.2 Posterior correlations

In contrast to the *a posteriori* uncertainty, which only have a meaning in relation to the *a priori* uncertainties, the *a posteriori* correlation coefficient between regional integrals of the flux fields (adjustable part only) have a direct interpretation. Ideally, the correlation coefficients are close to zero because this means that the regions are constrained independently by the data. Positive correlations indicate that two regions depend on the same signals in the data, which means that the information distinguishing them is potentially missing. Negative correlation coefficients (anti-correlation) indicate a so-called dipole between two regions, which means that the sum of the signals from both regions is better constrained than the regions individually. In consequence, the uncertainty reduction would increase if it were calculated for two merged anti-correlated regions.

The objective of this study is to determine if we are able to separate fossil fuel emissions from the other fluxes, mainly biospheric fluxes. We found that, while the correlations between the fossil fuel emissions and the remaining fluxes in the integration regions are relatively weak, they are also clearly negative for most of the processes (average correlation coefficient of -0.038 ± 0.067), which indicates that the sum of the signals from all processes is better constrained than the processes individually (Figure 4-29). We also found that the correlation

coefficients between fossil fuel emissions and the remaining fluxes in each region do not change significantly with the use of additional tracers (average correlation coefficients for the different scenarios of -0.0394 ± 0.07, -0.0356 ± 0.0623, -0.0392 ± 0.0694, and -0.0386 ± 0.0687 for the CO_2 only, CO_2+$^{14}CO_2$, CO_2+CO and CO_2+APO scenarios respectively). The largest difference was found when using the $^{14}CO_2$ constraint (Figure 4-30), which clearly is able to better separate fluxes in Baden-Wurttemberg and Lower Saxony in Germany, Bohemia in the Czech Republic and Grand-Est in France (increases in the correlation coefficient of 0.0655, 0.0256, 0.0389 and 0.0165 respectively). The constraints of CO and APO only marginally change the correlations between the processes. With CO, the correlation at Bourgogne-Franche-Comté in France becomes slightly more negative (decrease of -0.014). With APO, there are some improvements in the separation of fluxes in the Rhein-Ruhr and Frankfurt-Rhein-Main urban areas (increases of 0.0175 and 0.01303) but also a slightly more negative correlation coefficient in Northern Netherlands (decrease of -0.0073) which could be related to oceanic influences.

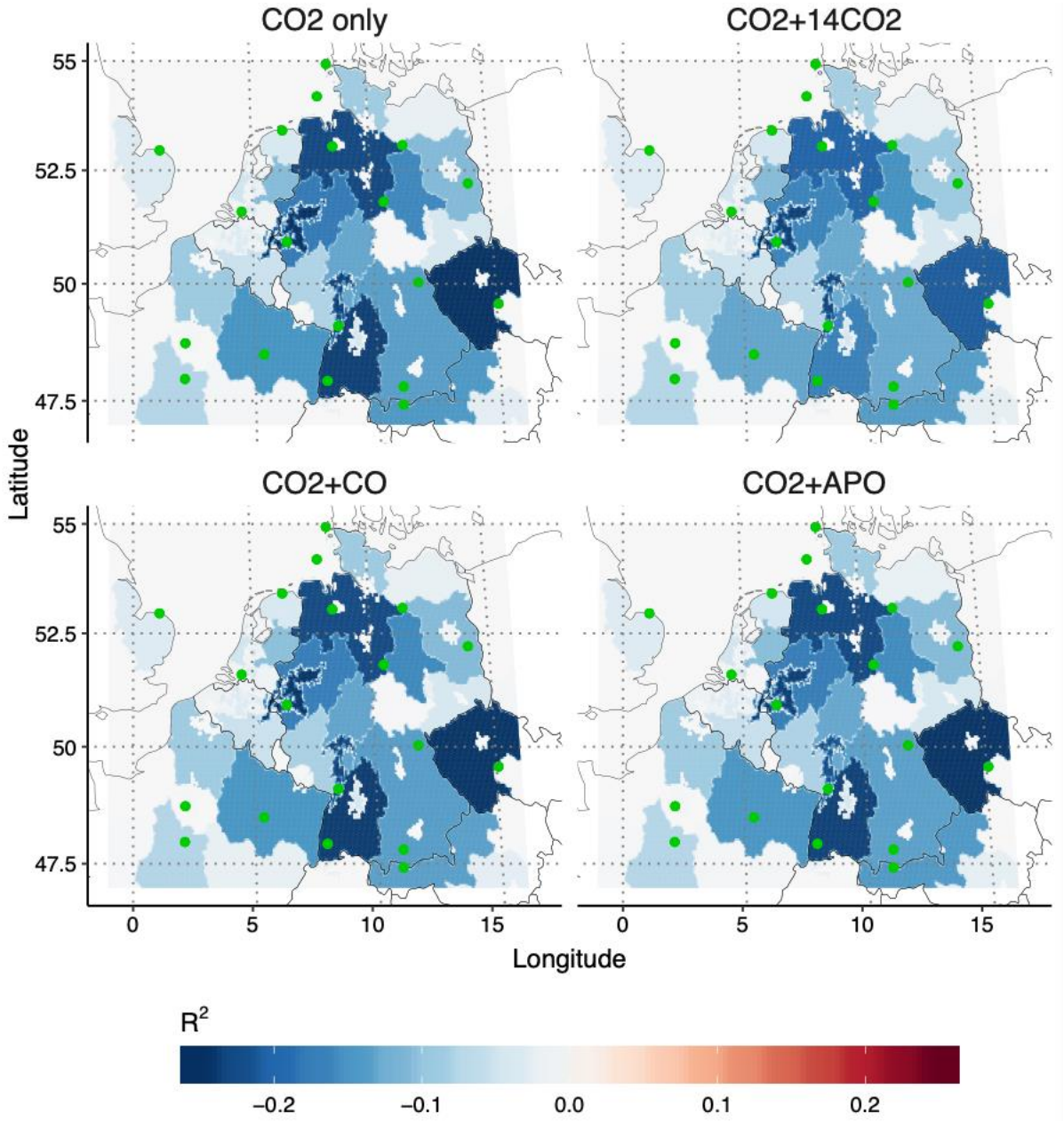

Figure 4-29 Correlation coefficient between fossil fuel emissions and other fluxes for each integration region.

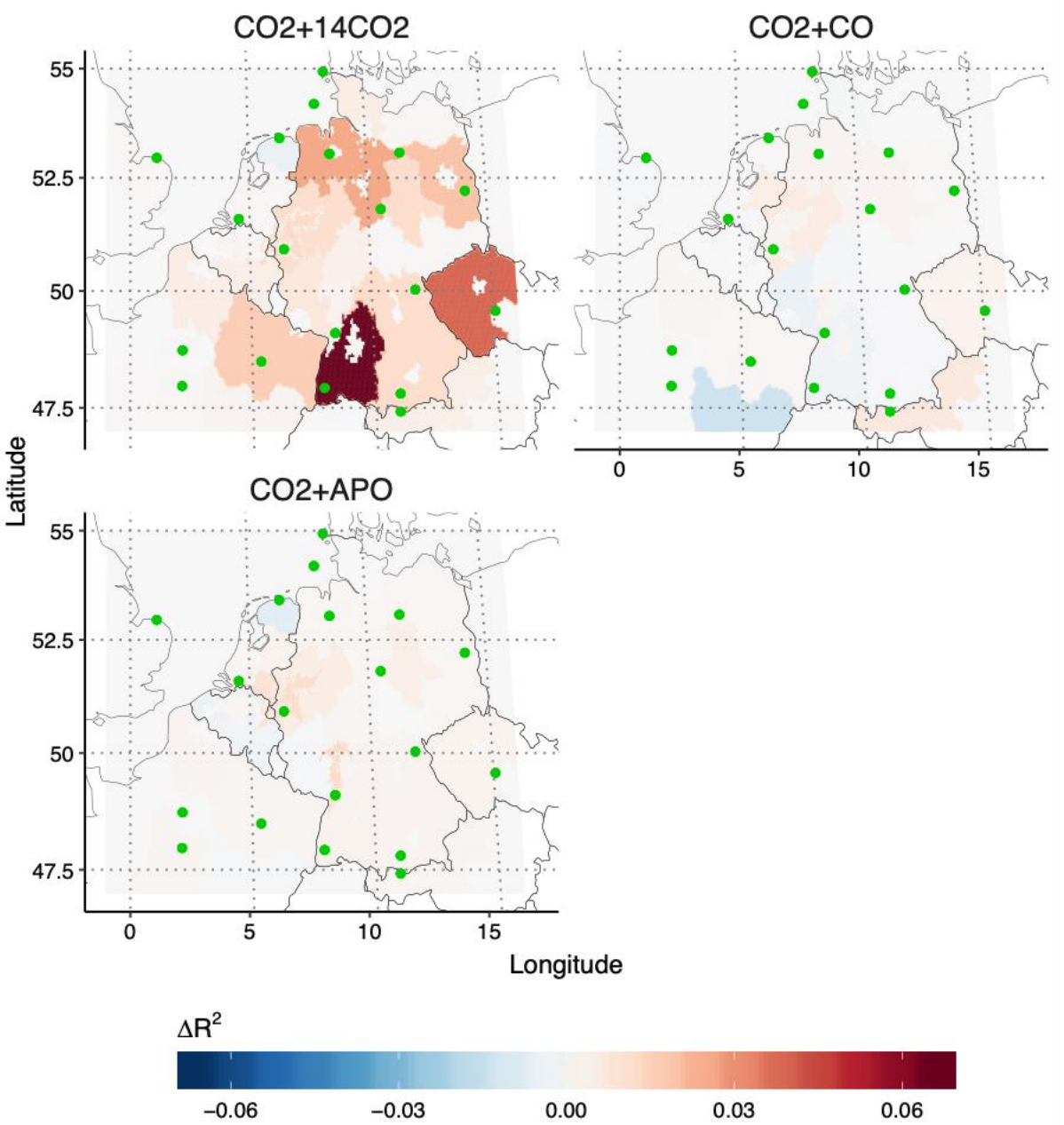

Figure 4-30 Difference correlation coefficient between fossil fuel emissions and other fluxes for each integration region in the scenarios with an additional constraint with respect to the CO_2 only scenario.

Finally, we added in quadrature the rows of the *a posteriori* correlation matrix for the different scenarios (Figure 4-31) to determine which regions were better constrained by the data (regions with the smallest sums of squares). We found that the inversion has problems separating regions enclosed by larger regions, e.g., Prague and Bohemia (average R^2 of 0.9299 ± 0.0149 and -0.243 ± 0.02 for fossil fuel emissions and other fluxes respectively from Prague against fossil fuel emissions in Bohemia), Berlin and Brandenburg (average R^2 of 0.9601 ± 0.0018 and -0.0126 ± 0.0033 for fossil fuel emissions and other fluxes respectively from Berlin against fossil fuel emissions in Brandenburg), Lower Saxony and Bremen (average R^2 of 0.854 ± 0.0043 for fossil fuels) and South East England and London (average R^2 of 0.6008 ± 0.0003 for fossil fuels). Furthermore, the Baltic Sea regions (Danish, Swedish and German) cannot be easily separated by the inversion for the fossil fuel emissions (average R^2 of 0.2503 ± 0.2896). It should be pointed out that the $^{14}CO_2$ constraint has a noticeable (although small) effect in the regions which cannot be separated from each other.

Interestingly, the correlations between the processes in the same regions are negative, which means that the sum of the signal from both processes is better constrained than for the processes individually, while the correlations between regions close to each other are positive, which indicates that the information distinguishing the regions is potentially missing.

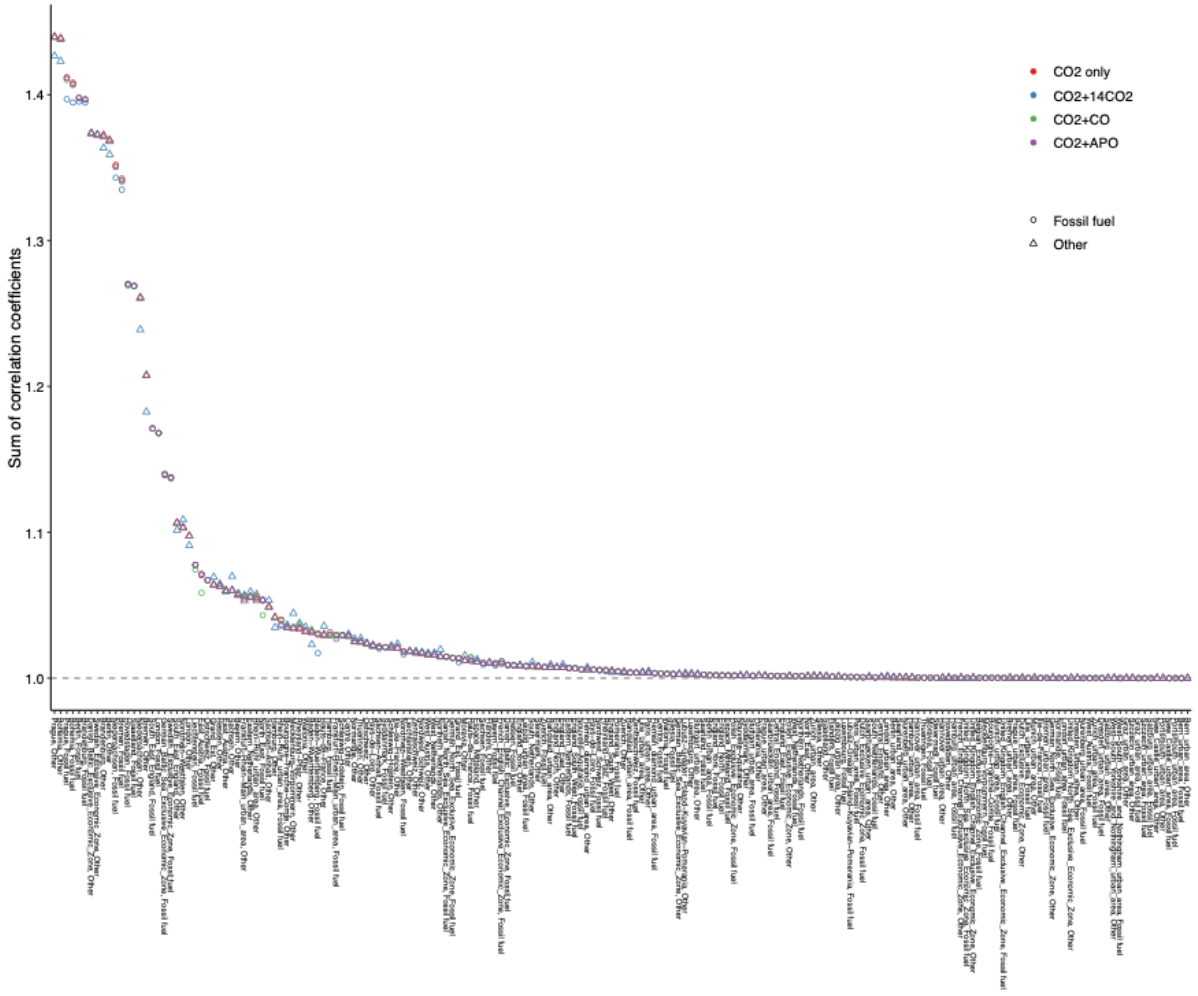

Figure 4-31 Square sums along the columns of the posterior correlation matrix ordered from highest to lowest. The regions with the highest sums are less well constrained.

4.4 Concluding recommendations

4.4.1 Station distribution

Fossil fuel signals are concentrated around urban centres and decrease in strength with the distance from the urban centres. Because the ICOS network was designed to constrain biospheric fluxes, most stations are located in rural or semi-rural settings and, in consequence, the ICOS network has a low sensitivity to fossil fuel emissions. Furthermore, for historical reasons stations were established in a bottom-up way by national research or environmental institutions at locations which reflect their interests, available infrastructure, funding and accessibility. Hence, in Europe, stations are concentrated in Central Europe with large gaps in Southern and Eastern Europe.

We recommend a new top-down approach using the tools demonstrated in this study, which included: analysis of footprints, analysis of modelled signals and analysis of uncertainty to find the most advantageous locations for stations. The network configuration shall follow these guidelines:

1. Close gaps. The analysis of the footprints revealed that it is possible to group the stations into regional clusters based on the correlations of their footprints. This is important because we can conclude that for a continental-wide observing system at least one station per region is required.
2. It is important to keep in mind that atmospheric inverse modelling is based on the gradients between stations. In this study, uncertainty reduction was larger in the centre of the domain than at the margins. Hence, the network should have stations upwind and downwind from the cities.
3. Separate the constraint on urban areas from the surrounding region. In this study it was possible to get a good constraint on two urban areas (the Rhine-Ruhr and Frankfurt-Rhine-Main regions) because of the near location of station FZJ and KIT respectively. However, other urban regions were not well constrained, despite the fact that they could have a nearby station, e.g. SAC near Paris. The number and location of stations around a city must be investigated.

4.4.2 Co-emitted tracers

In the determination of $ffCO_2$ from atmospheric measurements, APO had the best performance except for coastal stations, where oceanic fluxes can impede the accurate determination of $ffCO_2$, e.g., during the summer when the ocean is degassing due to warming. Furthermore, although APO is a tracer that was design to be conservative with respect biospheric fluxes, we observed that biospheric fluxes have non-negligible contributions to the regional APO signal because the oxidative ratios of photosynthesis and respiration deviate from the -1.1 ratio that defines the APO tracer. $\delta^{14}CO_2$ observations, which are assumed to be the "gold-standard" to determine $ffCO_2$ because fossil fuels are void of ^{14}C, have significant interference from $^{14}CO_2$ emissions from gas-cooled nuclear power plants, biospheric fluxes and biomass burning emissions. Importantly, studies to determine $ffCO_2$ based on atmospheric measurements have often only considered fossil fuel emissions and biospheric fluxes (photosynthesis and respiration). Yet, in this study we found significant interference from biomass burning emissions across the domain even though Western Europe is not a region with strong biomass burning emissions (Europe as a whole only contributes with 0.2% of the global biomass burning emissions, van der Werf, et al., 2010).

We extend the following recommendations:

1. APO is the best tracer to estimate $ffCO_2$ from atmospheric measurements except for locations with strong ocean influence.
2. The effect of processes beyond fossil fuel combustion and biospheric fluxes, which are often neglected, should be taken in consideration, at least biomass burning. Additionally, at least, the effects of nuclear power plants emissions, ocean fluxes and biofuels should be considered for $^{14}CO_2$, APO and CO respectively.

Wrong $^{14}CO_2/CO_2$, CO/CO_2 or APO/CO_2 ratios can introduce significant errors to the estimation of $ffCO_2$. In a modelling framework, the accurate CO/CO_2 or APO/CO_2 ratios depend on the accuracy of the inventory and the accuracy of transport. We extend the following recommendations:

3. Keep developing and refining emission inventories of co-emitted species, mainly:
   3.1. The dynamic modelling of changes in the CO/CO_2 or APO/CO_2 ratios given by changes in fuel proportions or combustion efficiency, e.g., automobile engines have less combustion efficiency during cold-starts in the winter.

3.2. The O_2/CO_2 ratios in the anthropogenic emission inventories use the assumption of full combustion (all organic carbon is transformed to CO_2). However, co-emitted species such as CO and NOx modify the amount of O_2 consumed. The development of stoichiometrically-correct inventories may reduce errors in the $ffCO_2$.

3.3. In the case of APO, it would be important to expand information on oxidative ratios of biospheric fluxes, e.g., Clay and Worral (2015), and how much they actually deviate from the canonical value of -1.1. Is the canonical O_2/CO_2 ratio of -1.1 really representative of global biospheric fluxes?

3.4. Further development of $^{14}CO_2$ inventories and models is required to determine the biospheric signals and ^{14}C content of vegetation, which is released through respiration and burning. ^{14}C content in annual crops can also be used to constrain atmospheric $ffCO_2$, e.g., Bozhinova et al. (2016).

3.5. Emissions are derived from a relatively simple model linking electricity generation at a particular nuclear power plant to its annual $^{14}CO_2$ emissions. Further refining, e.g., other factor driving emissions, and time-varying activity data of the power plants, e.g., times taken offline, is required.

4. Make accurate footprint calculations easily available for atmospheric measurement groups, e.g., a website where measurement location and time is provided and the user obtains a footprint and mole fraction.

The analysis of uncertainty of the inverse model results provided important information on how well the signals from different regions and processes were constrained. However, it was not capable of fully separating the contribution from fossil fuels and the contribution from the rest of the flux processes. An interesting fact to consider, is that in the inversion the constraint improves more when there are emissions and not when they are missing, e.g., $^{14}CO_2$ improves mainly the uncertainty reduction of the other flux processes (mainly biospheric), while CO and APO improve the uncertainty reduction of fossil fuel emissions. We provide the following recommendation:

5. The analysis of inversions using CO_2, $^{14}CO_2$, CO and APO should be expanded considering the following:

5.1. Include different network configuration, e.g., more urban, more rural or mixed, and more or less.

5.2. In D4.3, we set particular values for the measurement and modelling uncertainty of the measurements. While the measurement uncertainty is typically set by data providers, the model uncertainty is rather arbitrary. The proportion of the model uncertainty to the measurement values is different for each tracer. This may explain the fact that CO was better to constrain the fossil fuel emissions than APO. To solve this issue, a characterization of the modelling error for all tracers is required, e.g., by the analysis of inversions with pseudo-data or by the spread of the modelled mole fractions in different models using the same fluxes.

5.3. Due to the fact that $^{14}CO_2$ improves the uncertainty reduction of the other flux processes (mainly biospheric), while CO and APO improve the uncertainty reduction of fossil fuel emissions, we recommend further experiments with three tracers to determine if these tracers can be used complementarily.

4.4.3 Other recommendations

1. The growing amount of data and increasing resolution required for emission inventories has caused very high demands on the computational cost of running simulations or even to ingest the data into the model. We recommend to invest in expanding the computational capacity of the community and at the same time improving and optimizing the models.

5 Assessment from NILU

NILU performed forward and backward simulations with the Lagrangian particle dispersion model FLEXPART for winter and summer 2015. Synthetic in situ and remote (XCO_2) measurements were simulated and used in CO_2 flux assessment OSSEs. The species simulated were CO_2 (fossil fuel, biofuel, biogenic and background), CO (fossil and biofuel), $^{14}CO_2$ and APO. CO_2 background fields were provided by FLEXPART-CTM. Fluxes for fossil fuel and biofuel CO_2 and CO were provided by TNO. Biogenic CO_2 was simulated using LPJ-GUESS NEE. $^{14}CO_2$ considers anthropogenic emissions from nuclear facilities. Except for the $^{14}CO_2$ from nuclear facilities, simulations were performed in two nested domains centered around the Oslo fjord area. Synthetic in situ measurements were simulated and used in CO_2 flux assessment OSSEs.

5.1 Simulations setup

5.1.1 Models

The simulations were performed with different versions of the Lagrangian particle dispersion model FLEXPART (Pisso et al. 2019b), representing atmospheric transport by means of Lagrangian trajectories of a large number of particles in the atmosphere. Forward calculations were performed with both the standard (with ECMWF winds) and WRF (Brioude et al., 2013) versions. Backward calculations for the background were performed with the standard version coupled with FLEXPART-CTM (Groot Zwaaftink et al., 2018).

5.1.2 Domains

For local simulations, two domains containing the Oslo fjord area were used: [8.5ºE 12.5ºE 58.8ºN 61.2ºN] at 0.05 degrees resolution and [10.36ºE 10.94ºE 59.74ºN 60.02ºN] at 0.01º resolution (0.5 km). For the $^{14}CO_2$ simulations, a European domain [10ºW 40ºE 35ºN 70ºN] at 1º and nested 0.5º resolution was used instead only in forward mode to estimate the influence from nuclear facilities.

5.1.3 Meteorology

For ECMWF runs nested fields were used. The mother domain uses global 1º × 1º fields at full levels and the nest 0.1º × 0.1º fields in the domain [8.5ºE 12.5ºE 58.8ºN 61.2ºN] with the lowest 39 eta levels.

5.1.4 Emission fluxes and background mixing ratios

5.1.4.1 CO_2 emissions

The input fluxes were obtained from TNO. Alternative fossil fuel simulations were performed with ODIAC (Oda et al., 2018) and with the NILU-URGE Anthropogenic CO_2 emission inventory for Oslo (Pisso and Lopez Aparicio, in preparation). The anthropogenic CO_2 fields that were used together with other tracers (same grid as for CO and O_2) were calculated with emissions produced by TNO for the CHE project (D4.2, mid resolution fluxes ; note that the TNO mid-resolution fluxes include Oslo, but not the TNO high-resolution fluxes). The data set includes CO and O_2 in the same grid as for CO_2. Both fossil fuel and biofuels were simulated. All 15 GNFR sectors from TNO files were added together in order to provide a single emission source per gridcell. Point sources were also included in the integrated gridded emissions. Biogenic emissions were from LPJ-GUESS NEE.

5.1.4.2 CO emissions

The anthropogenic CO fields were produced by TNO for the CHE project (D4.2). Both fossil fuel and biofuels were simulated. The background value was fixed at 80 ppbv for most OSSEs.

5.1.4.3 $^{14}CO_2$ emissions

Fossil fuel emissions are devoid of $^{14}CO_2$. Background and biogenic emissions are assumed to have a $\Delta^{14}C$ of 45 per mil which is about the background value measured at the site of Jungfraujoch (Bozhinova et al., 2014; Levin et al. 2010). Anthropogenic emissions from the nuclear industry were provided by LSCE. We used continuous releases at a constant yearly rate (e.g. the largest source from the La Hague processing plant resulted in emissions of 0.0994 kg/yr ~ 16.4 TBq/yr). This yielded an influence in Southern Norway of the order of ~10^{-12} ppmv in agreement with Bozhinova et al., (2014). The $\Delta^{14}C$ values simulated in Oslo during e.g. winter 2015 ranged between 8 and 47 per mil.

5.1.4.4 APO emissions

The O_2 consumption fields from TNO (calculated according to the fossil fuel CO_2) were used in order to simulate the contribution to APO from fossil fuel and biofuel combustion to APO. The definition of APO was used in order to simulate the contribution from biogenic activity. Reference values of O_2 and N_2 in all cases were those of a standard atmosphere. The contribution from oceanic fluxes is not simulated but introduced as a perturbation on the mean state for sensitivity calculations. Although a more comprehensive modelling framework may be necessary to establish comparisons with actual measurements, a simplified setting is deemed appropriate for the OSSEs presented in this assessment.

5.2 Tracer simulations

5.2.1 FLEXPART runs

The Lagrangian model was run with 3-hourly releases each release containing 5×10^5 and 8×10^4 particles for CO_2^{ff} and CO_2^{bio}, with a maximum total number of 3.5×10^8 particles per simulation.

Table 1: FLEXPART simulations

Name	Description	Settings
201501	Jan 2015	Integrated releases
201502	Feb 2015	Integrated releases
201507	July 2015	Integrated releases
201501 WRF	Jan 2015	Integrated releases
BKG	Background from full columns	Oslo domains. Coupled with FLEXPART-CTM
14C	LSCE emissions	Europe domain
fwd_TNO	TNO emissions	Oslo domains
fwd_3d	NILU emissions	Oslo domains

5.2.2 Simulated tracer fields and synthetic *in-situ* observations

Spatio temporal distributions of tracer fields were calculated using a combination of forward and backward trajectory calculations. For the simulated contribution of the available emission inventories (both natural and anthropogenic) forward calculations were used. Unit emissions were simulated from releases representing all available sources. Separated calculations were performed for both biogenic (e.g. LPJ-GUESS) and anthropogenic (e.g.

TNO, NILU) inventories, due to the different spatio-temporal resolutions of the input data. For each release hourly outputs of mass concentration and mixing ratio fields were produced in the mother and nest FLEXPART output grids described above.

Backward calculations were used for the background together with FLEXPART-CTM CO_2 output fields.

The simulated tracer fields were interpolated in order to produce synthetic measurements.

NILU simulated both in situ and remote synthetic measurements for January and July 2015. Results are illustrated mainly with a focus on summer simulations, when the biogenic component is more active and the separation of fossil fuel from background is more challenging than in winter due to the signal being overwhelmed by the other components. Oslo (60ºN) displays strong seasonal contrasts.

5.2.2.1 CO_2 fields and synthetic in-situ observations

The CO_2 synthetic measurements include, in addition to the background, biogenic fluxes, biofuel and fossil fuels.

$$CO_2^{tot}=CO_2^{bkg}+CO_2^{bio}+CO_2^{ff}+CO_2^{bf}$$

Anthropogenic emissions from the NILU inventory from fossil and biofuel are available as annual means, therefore when included the temporal variations are daily/weekly cycles around the mean. The same applies to the outer domain (mid resolution) of TNO D4.2 emissions used here. In the case of biogenic fluxes (LPJ-GUESS) an adequate representation of the time variation is necessary in order to represent well the daily cycle in the mixing ratio. Biogenic emission time resolution is 3 hours. Figure 5-1 shows the synthetic observations together with its components for the selected period 1-3 July 2015.

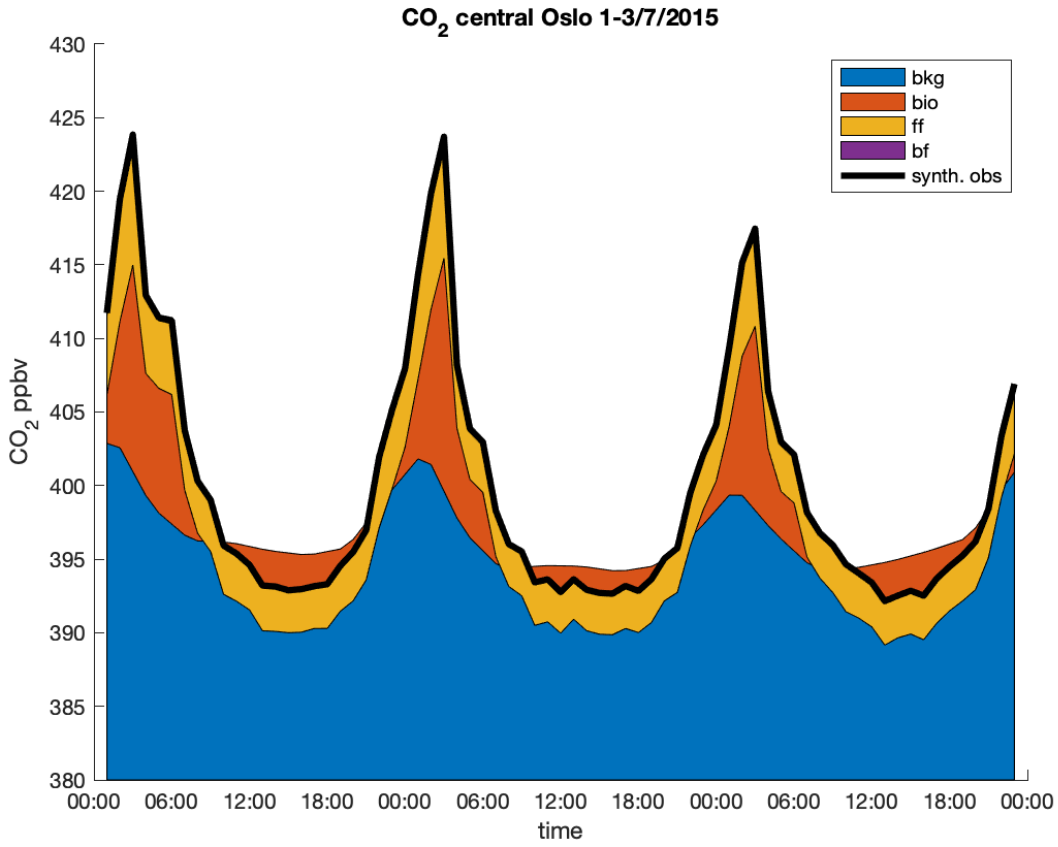

Figure 5-1: Synthetic CO_2 observations and its components for the selected period 1-3 July 2015 in the Oslo domain.

5.2.2.2 CO fields and synthetic in-situ observations

For CO only fuel combustion and a constant background are considered. Biogenic emissions and biomass burning are included only as a perturbation to the background for sensitivity tests.

$$CO^{tot}=CO^{bkg}+CO^{bio}+CO^{ff}$$

Figure 5-2 shows the synthetic observations together with its components for the selected period 1-3 July 2015.

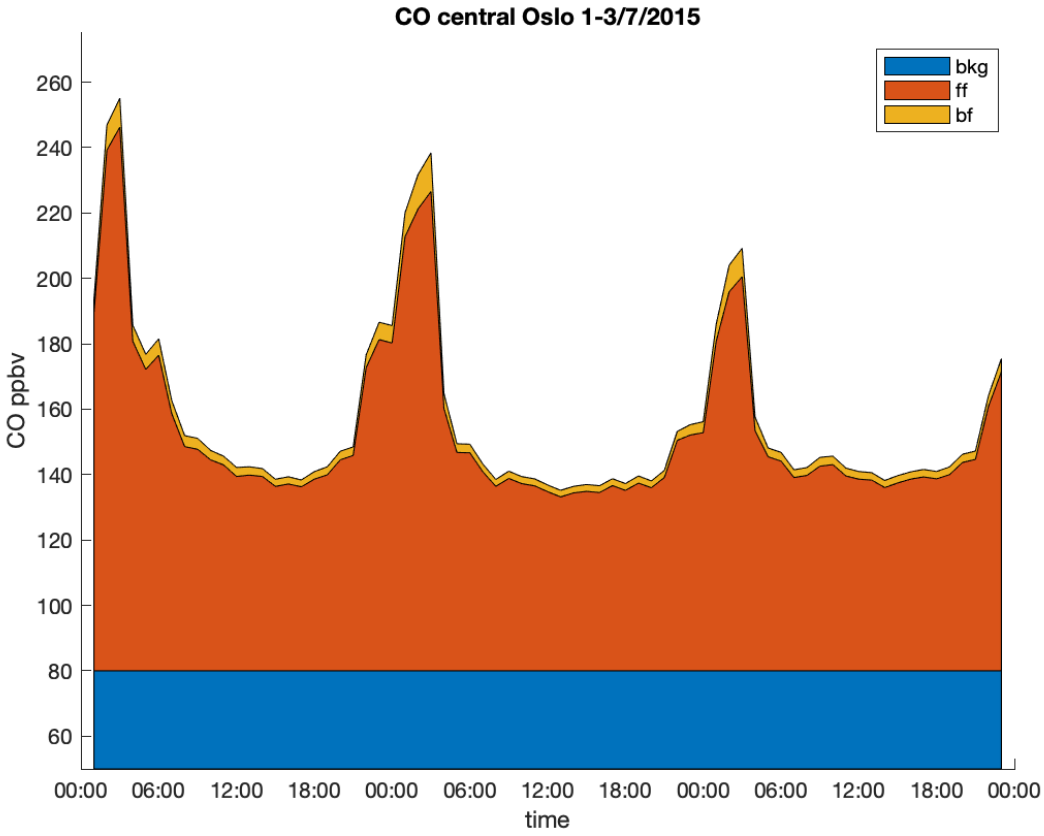

Figure 5-2: Synthetic CO observations and its components for the selected period 1-3 July 2015 in the Oslo domain.

5.2.2.3 $^{14}CO_2$ fields and synthetic in-situ observations

The atmospheric budget of $^{14}CO_2$ was modelled following Levin et al. (2003) and Bozhinova et al. (2014). For the mixing ratios:

$CO_2^{obs} = CO_2^{bkg} + CO_2^{ff} + CO_2^{bio} + CO_2^{bf}$

and for the isotopic ratios (Δ^x indicates the $\Delta^{14}CO_2$ signature of CO_2 of a particular origin):

$\Delta^{obs}CO_2^{obs} = \Delta^{bkg}(CO_2^{bkg} + CO_2^{bio} + CO_2^{bf}) + 0 \times CO_2^{ff} + \Delta^{nuc}\,{}^{14}CO_2^{nuc}$

where the last term corresponds to the nuclear plant emissions.

This yielded an influence in Southern Norway of the order of ~10-12 ppmv in agreement with Bozhinova et al., (2014). The $\Delta^{14}C$ values simulated in Oslo during e.g. winter 2015 ranged

between 8 and 47 per mil.

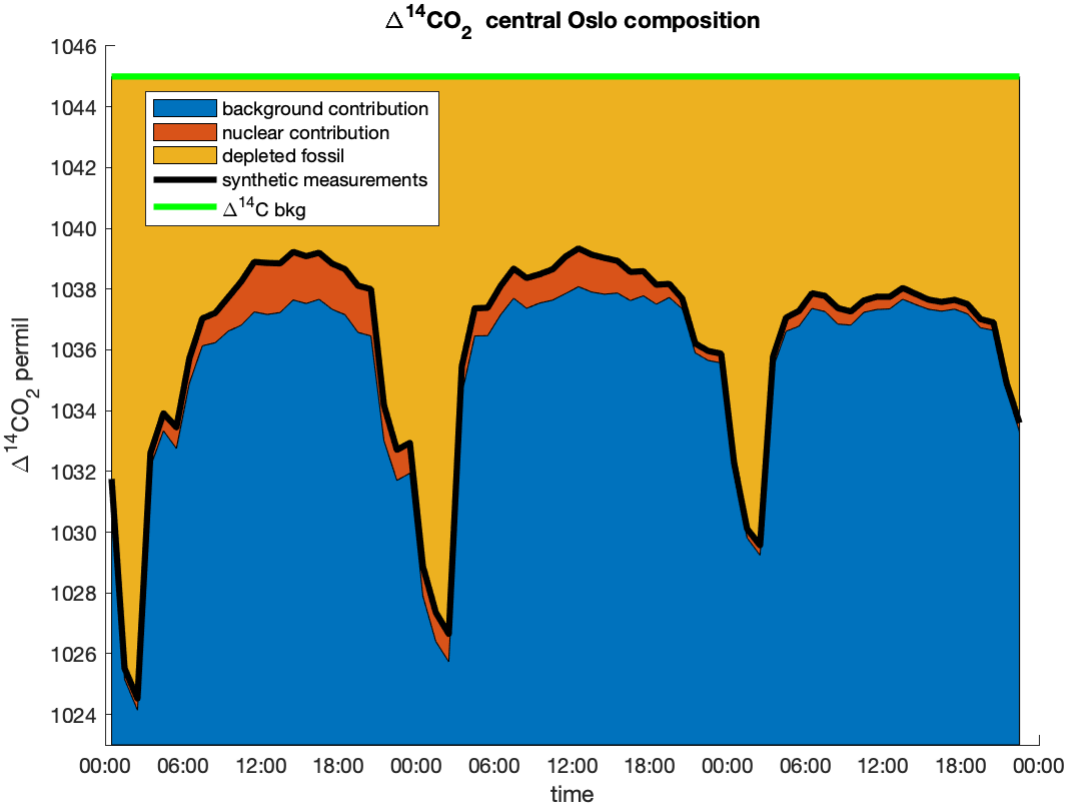

Figure 5-3: Synthetic $\Delta^{14}CO_2$ observations (in permil) and its components for the selected period 1-3 July 2015 in the Oslo domain.

5.2.2.4 APO fields and synthetic in-situ observations

The definition of APO used was (with APO and δO_2 in per meg, CO_2 in ppmv and 0.2095 the conversion factor):

$APO = \delta O_2 + (-1.1/0.2095) * (350 - CO_2)$

APO was simulated based on O_2 consumption by combustion provided by TNO and biogenic CO_2 fluxes form LPJ. The representation of APO is schematic and chiefly for its use in sensitivity analysis. In particular the influence of oceanic fluxes is limited to perturbations on the background state. However, we focus on short time scales in limited domains around an urban area where the main short-range influence comes from fossil CO_2.

The main processes considered affecting the oxygen balance are combustion and photosynthesis/respiration (O_{2apo} represents the O_2 consumed and O_2^{bio} = - 1.1 CO_{2bio} from LPJ fields)

$O_2^{apo}=O_2^{bf}+O_2^{ff}+O_2^{bio}$

The (synthetic) reference values for O_2^{ref} and N_2^{ref} were 209460 and 780840 ppmv respectively.

Therefore for a location loc (e.g. background or sample) at x^{loc}:

$O_2^{loc} = O_2^{ref} - O_2^{apo}(x^{loc})$

$N_{2loc}=N_2^{ref}$

$\delta O_2^{loc}= ((O_2^{loc}/N_2^{loc})/O_2^{ref}/N_2^{ref} -1)*10^6$

$CO_2^{loc}=CO_2^{tot}$ (i.e total CO_2 using TNO fuel emissions consistent with the O_2 consumption)

$APO^{loc} = \delta O_2^{loc} + (-1.1/0.2095) * (350 - CO_2^{loc})$

Figure 5-4: Synthetic APO simulations.

5.3 Separating background from fossil fuel CO_2 using additional tracers

In order to generate arbitrary time series of synthetic measurements of additional tracers within the domain, first 4D fields of the four artificial tracers described above were generated with the model output described in section 5.2. Each simulated time series of additional tracers was used to separate CO_2^{ff} from the total CO_2 measurements interpolated from the total three dimensional CO_2 concentration field described above. Figure 5-5 shows synthetic measurements of CO_2 and additional tracers during a 1st -3rd July 2015.

The proxy CO_2^{ff} values were calculated from CO, $^{14}CO_2$ and APO using the following formulas:

$$CO_2^{ff}{}_{CO} = (CO^{meas} - CO^{bkg})/R_{CO}$$

$$CO_2^{ff}{}_{14CO2} = CO_2^{meas} (1 - {}^{14}CO_2^{meas}/{}^{14}CO_2^{bkg})$$

$$CO_2^{ff}{}_{APO} = (APO^{meas} - APO^{bkg})/R_{APO}$$

Where ‘meas’ corresponds to the synthetic measurements, ‘bkg’ to the background and R is a proportionality constant. The values of the proportionality constants were R_{CO}~20 (notice the range 7.9 - 14.5 ppb ppm^{-1} for Paris after Lopez et al. (2013)) and R_{APO}~0.23 ppmbv $permeg^{-1}$ (range 0.2 to 0.5 with a conversion factor 0.2095 between permeg and ppmv). The corresponding time series of estimated CO_2^{ff} proxies for central Oslo during the period selected for analysis are shown in Figure 5-6. The resulting estimated CO_2^{ff} time series at hypothetical station locations were used to constrain short term CO_2^{ff} fluxes via inverse modelling.

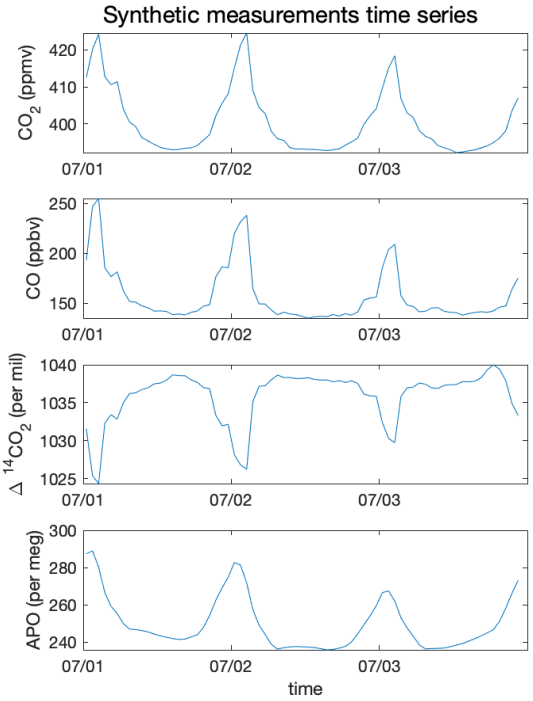

Figure 5-5: Synthetic measurements of CO_2, CO, ^{14}C and APO used to create proxy CO_2^{ff} pseudo observations

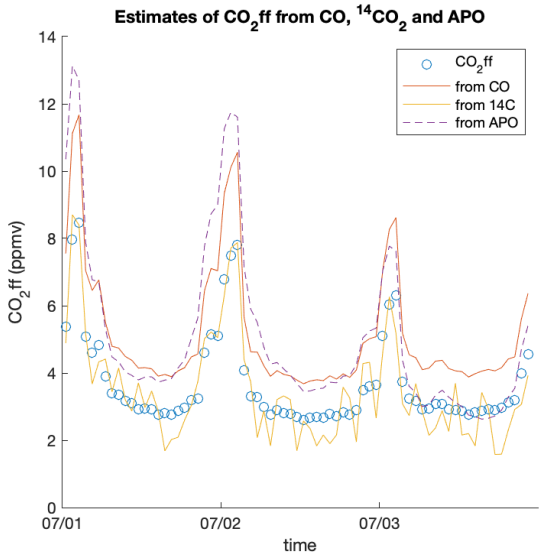

Figure 5-6: Pseudo observations of CO_2^{ff} estimated form additional tracers (CO_2, CO and ^{14}C)

5.4 Fossil fuel CO_2 constraints from local area inversions

In order to assess how in-situ measurements of additional species contribute in constraining CO_2^{ff} fluxes in an idealised scenario we performed local area inverse calculations. The constraints are based on estimates of CO^{ff} from pseudo observations of additional tracers.

5.4.1 SRR sensitivity calculations

SRRs were calculated using FLEXPART with a similar setting as for the tracer simulations but releasing unit emissions and processing separately the 4D fields resulting from each individual source. For each release hourly outputs of mass concentration and mixing ratio fields were produced in the mother and nest FLEXPART output grids described above resulting in four 5D fields for each simulation.

The source relation relationship was calculated from FLEXPART forward trajectories. This allowed for increased flexibility in the definition of the synthetic network of stations at the local level. A subset of the nested grid was defined with a resolution of 0.3º and a synthetic measurement station was considered in each grid point. A time series for each additional species and proxy CO_2^{ff} are available at each point.

5.4.2 Inverse flux estimates

A series of local scale inverse problems were constructed using these time series and the TNO emissions grid. The inverse problems configurations follow D4.3. The inversion settings follow those described in Pisso et al. (2019a). The observation error covariance was diagonal with a 1 ppb absolute error. The flux error covariance has a relative error of 100 % with non-diagonal terms with exponentially decaying spatial correlations with a scale of 0.1º. The prior fluxes were constructed from the inventories by adding a random noise and a 10% bias.

5.4.3 Pseudo-network optimisation maximising uncertainty reduction

For each one of the 200 points on the grid, a one-station inverse calculation was run. The results and derived diagnostics such as the uncertainty reduction and the relative difference to the true fluxes were recorded. Using the uncertainty reduction as metric, the points with maximum uncertainty reduction follow the transport patterns and are located downwind from the densest urban areas. Starting from the optimal location, a subsequent exploration of the synthetic station list was performed in order to choose the optimal multi-point configuration. The process was iterated in and Incremental Optimisation (Patra and Maksyutov, 2003) until choosing five synthetic stations. A question arising in placing stations around a city is whether the sites should be in the centre or in the periphery. The correlation of the locations of the stations with the magnitude of the flux in the corresponding location, as the use of the uncertainty reduction as a metric does not favour the choice of locations in the city centre but rather around, in a peripheral ring. The uncertainty reduction is a robust metric that does not use the distribution of the prior fluxes but only the transport/observation operator and the error covariances (fluxes and observations).

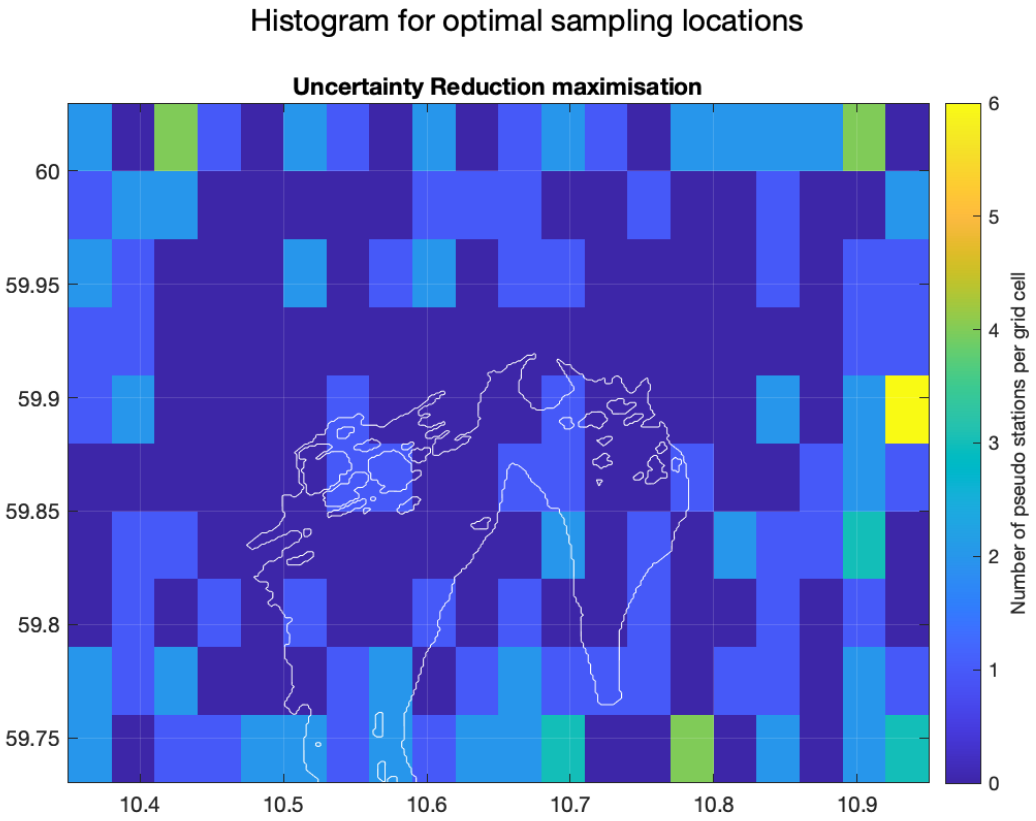

Figure 5-7: Histograms of all locations of sampling locations defined for July 2015. Every day of July an Incremental Optimisation process is executed and 5 pseudo stations are obtained using the maximisation of uncertainty reduction as the metric.

5.4.4 Optimisation using alternative metrics

There are alternative metrics to uncertainty reduction that use information explicitly about the location of the prior fluxes. In the case of OSSEs where the true fluxes are known, the normalised distance to the nature run can be used as penalty function. Here, the Incremental Optimisation procedure described above was executed using CO_2^{ff} proxies derived from the pseudo observations of CO, ^{14}C and APO.

In this case in contrast with the previous one, there is a significant correlation between the relative difference with respect to the true fluxes and the fluxes themselves. This is the case using the CO_2^{ff} proxy from CO, ^{14}C and APO. In contrast with the case of uncertainty reduction, the use of the nature run is strongly dependent on the prior and biased towards it. Therefore, in practice it can only be used where the real location of the source is known with a high confidence. Uncertainty reduction on the other hand is suitable in general, also when there is little knowledge about the true fluxes.

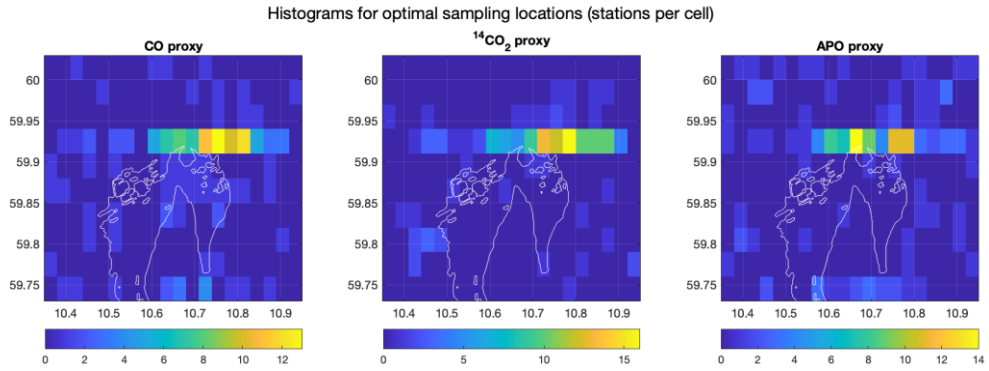

Figure 5-8: Histograms of all locations of sampling locations defined for July 2015. Normalised difference with nature run was used as metric with CO_2, CO, ^{14}C and APO used to create proxy CO_2^{ff} pseudo observations

Table 5-2: Spatial correlation for the histograms of 5 optimal locations per day in July 2015 and nature run fluxes

Metric	correlation coefficient	p value	confidence interval
UR	-0.27	$<10^{-5}$	[-0.40 -0.14]
CO proxy	0.74	$<10^{-5}$	[0.67 0.80]
^{14}CO2 proxy	0.74	$<10^{-5}$	[0.68 0.80]
APO proxy	0.62	$<10^{-5}$	[0.53 0.70]

5.5 Recommendations

While assessing anthropogenic emission fluxes of CO_2, measurements in or close to the city centre provide a stronger constraint than rural sites.

We tested the hypothesis that stations located within the highest emitting grid cells provide the most information. We found that when using a limited amount of measuring points, the accuracy of the retrieved fluxes has a weak correlation with the measurements located in the highest emitting cells. The alternative arrangement consists in measurements up and downwind from the highest emitting grid cells, such as in a ring distribution around the city centre, in agreement with previous examples described in the literature.

In the configuration used here, the weak correlation with the city centre holds for calculations with the three different proxy CO_2^{ff} (CO, ^{14}C, and APO) tracers. However, in the idealised setting used here, there is a sufficiently good knowledge of the background magnitude of the additional tracers and only perturbations thereof are studied. In a more realistic setting great care should be taken in properly assessing the background of all three species.

A similar statement applies to the factors used to convert each additional tracer and CO_2^{ff} as these are dependent on season and location and likely to have long term trends.

6 Assessment from UEA

6.1 Background: Covid-19 detection from atmospheric data

A new study by Pickers et al. (2020) has robustly detected a reduction in $ffCO_2$ in the atmosphere associated with the Covid-19 lockdown restrictions. This was achieved using continuous (hourly) Atmospheric Potential Oxygen (APO) data from Weybourne Atmospheric Observatory, UK, combined with a machine learning algorithm to account for the effects of weather and atmospheric transport processes on the atmospheric $ffCO_2$ signal. To our knowledge, this is the first study to identify and quantify a Covid-19 $ffCO_2$ signal in atmospheric data. The main text and figures of the submitted manuscript are included in the CHE deliverable 1.3 report, section 7, as part of the "detection of key/extreme events" part of work package 1.

6.2 How was this achieved?

The detection of a Covid-19 $ffCO_2$ signal in the atmosphere was only made possible by the use of a continuous (i.e. high frequency, such as hourly) $ffCO_2$ tracer, used in conjunction with machine learning techniques. It would not have been possible to detect such a signal using a discrete tracer, such as $^{14}CO_2$, owing to the requirement for high frequency data with which to train the machine learning model. Using continuous atmospheric CO_2 data, instead of APO data, combined with the machine learning was also unsuccessful, owing to large signals in the atmospheric CO_2 data from the terrestrial biosphere. In addition, it was not possible to detect the Covid-19 $ffCO_2$ signal using the APO data alone (i.e. without the use of machine learning), owing to the significant influence of atmospheric transport processes on the APO data.

6.3 Implications for surface network design

For any future design of Europe's surface GHG network, it is important to consider the value added by continuous $ffCO_2$ capability. While any network design should rightly be based on well-established methods, such as discrete $^{14}CO_2$ sampling, recent developments in new continuous $ffCO_2$ tracers may offer their own benefits. In particular, the advent of machine learning methods may lead to changes in the traditional landscape of the top-down detection and attribution problem in coming decades.

Continuous tracers can, by nature, provide higher temporal resolution information (e.g. sub-annually, sub-monthly), which is important for the timely detection of top-down emissions estimates. For example, the effects of Covid-19 lockdowns may yet become visible in discrete $^{14}CO_2$ datasets in a few years' time, though it is unlikely that the signal will be visible on the sub-annual timescale (an important consideration for Covid-19, which is characterised by months of significant emissions reductions during national/local lockdowns interspersed by months of relative normality). Thus, it may be that the $^{14}CO_2$ signal, once detected, will be too late to have significant bearing on environmental policies arising from lessons learnt during the Covid-19 crisis.

Finally, in any network where the availability of atmospheric data is a key constraint, continuous $ffCO_2$ tracers can help improve the robustness of data availability, since they are generally less susceptible to the potential pitfalls experienced by discrete sampling strategies, which are: sampling when $ffCO_2$ signals are too low; sampling when the wind dynamics are sub-optimal; and sampling when air masses are unduly affected by local emissions or undesirable contaminants (such as nuclear powerplant emissions, in the case of $^{14}CO_2$).

7 Conclusion

This report marks the formal end of CHE WP4. It was designed as an ambitious collective work that mutualized much of the preparatory effort for the high-resolution forward and inverse numerical simulations, as highlighted with D4.3, “Attribution Problem Configurations”. The challenges of carrying out the high-resolution simulations were also taken with success despite various technical difficulties. The four modelling groups (CEA/LSCE, EMPA, MPG and NILU), helped by TNO and UEA, have gathered a large amount of results about the contribution of fossil fuel emissions in CO_2, CO, $^{14}CO_2$, CO and APO ground-based (all tracers) and satellite (in the case of CO_2 only) observations and the possibility to infer the former form the latter. The time-scale of the project has not allowed discussing the results much within the group after the simulations were made: we therefore forward the reader to the individual conclusion sections above (2.4 for CEA/LSCE, 3.3 for EMPA, 4.4 for MPG, 5.5 for NILU and 6.3 for the experimental results of UEA) that best represent the understanding of the results at this stage. They will all make their way towards the peer-reviewed literature with additional analyses.

At this stage, it remains interesting to note the converging conclusion about the information content of all tracers, including the CO_2 column averages observed from space. All works highlight the complex link between the CO_2, $^{14}CO_2$, CO and APO atmospheric tracers on the one hand, and the CO_2 fossil fuel emissions on the other hand. This complexity comes with modelling uncertainties that remain too large for a CO_2 emissions Monitoring and Verification Support capacity to rely on a single tracer. The observation system has therefore to expand into a robust system of systems where redundancy among information sources compensates for modelling errors, and where complementarity among tracers compensates for the temporary blindness of some data sources during longer or shorter periods of time. Last, the various modelling studies also note the importance of ground-based tracer measurements in the close vicinity of cities.

Acknowledgements

The simulation of CO_2M XCO_2 samplings over the area of interest in the CEA/LSCE section has been generated by IUP-UB in the framework of the ESA PMIF project.

8 References

Basu, S., Baker, D. F., Chevallier, F., Patra, P. K., Liu, J., and Miller, J. B.: The impact of transport model differences on CO2 surface flux estimates from OCO-2 retrievals of column average CO2, Atmos. Chem. Phys., 18, 7189–7215, https://doi.org/10.5194/acp-18-7189-2018, 2018.

Bozhinova D, Van Der Molen MK, Van Der Velde IR, Krol MC, Van Der Laan S, Meijer HAJ, et al. Simulating the integrated summertime δ14CO2 signature from anthropogenic emissions over Western Europe. Atmos Chem Phys. 2014;14(14):7273–90.

Bozhinova, D. N., Palstra, S. W. L., van der Molen, M. K., Krol, M. C., Meijer, H. A. J., & Peters, W. (2016). Three Years of $\Delta^{14}CO_2$ Observations From Maize Leaves in the Netherlands and Western Europe. *Radiocarbon*, *58*(3), 459–478. http://doi.org/10.1017/RDC.2016.20

Bréon, F. M., G. Broquet, V. Puygrenier, F. Chevallier, I. Xueref-Remy, M. Ramonet, E. Dieudonné, et al. 2015. « An attempt at estimating Paris area CO2 emissions from atmospheric concentration measurements ». Atmos. Chem. Phys. 15 (4): 1707-24. https://doi.org/10.5194/acp-15-1707-2015.

Brioude J, Arnold D, Stohl A, Cassiani M, Morton D, Seibert P, et al. The Lagrangian particle dispersion model FLEXPART-WRF version 3.1. Geosci Model Dev. 2013;6(6):1889–904.

Broquet, G., F.-M. Bréon, E. Renault, M. Buchwitz, M. Reuter, H. Bovensmann, F. Chevallier, L. Wu, et P. Ciais. 2018. « The potential of satellite spectro-imagery for monitoring CO2 emissions from large cities ». Atmos. Meas. Tech. 11 (2): 681-708. https://doi.org/10.5194/amt-11-681-2018.

Chevallier, F., B. Zheng, et al. (2020), Local anomalies in the column-averaged dry air mole fractions of carbon dioxide across the globe during the first months of the coronavirus recession, Geophys. Res. Lett, doi:10.1029/2020GL090244.

Ciais, P., D. Crisp, H. Denier van der Gon, R. Engelen, G. Janssens-Maenhout, M. Heimann, P. Rayner, and M. Scholze: Towards a European Operational Observing System to Monitor Fossil CO2 Emissions - Final Report from the expert group, European Commission, B-1049 Brussels, doi: 10.2788/350433, 2015.

Clay, G. D., & Worrall, F. (2015). Oxidative ratio (OR) of Southern African soils and vegetation: Updating the global OR estimate. *Catena*, *126*(C), 126–133. http://doi.org/10.1016/j.catena.2014.10.029

Denier van der Gon, Hugo A. C., Jeroen J. P. Kuenen, Greet Janssens-Maenhout, Ulrike Döring, Sander Jonkers, et Antoon Visschedijk. 2017. « TNO_CAMS High Resolution European Emission Inventory 2000–2014 for Anthropogenic CO2 and Future Years Following Two Different Pathways ». Earth System Science Data Discussions, novembre, 1-30. https://doi.org/10.5194/essd-2017-124.

Gamnitzer, U., Karstens, U., Kromer, B., Neubert, R. E. M., Meijer, H. A. J., Schroeder, H., & Levin, I. (2006). Carbon monoxide: A quantitative tracer for fossil fuel CO2? *Journal of Geophysical Research*, *111*(D22), 15915. http://doi.org/10.3402/tellusb.v48i4.15934

Gerbig, C., Lin, J. C., Wofsy, S. C., Daube, B. C., Andrews, A. E., Stephens, B. B., et al. (2003). Toward constraining regional-scale fluxes of CO 2with atmospheric observations over a continent: 2. Analysis of COBRA data using a receptor-oriented framework. *Journal of Geophysical Research*, *108*(D24), n/a–n/a. http://doi.org/10.1034/j.1600-0889.2003.00030.x

Groot Zwaaftink CD, Henne S, Thompson RL, Dlugokencky EJ, Machida T, Paris JD, et al. Three-dimensional methane distribution simulated with FLEXPART 8-CTM-1.1 constrained with observation data. Geosci Model Dev. 2018;11(11):4469–87.

Janssens-Maenhout, G., Pinty, B., Dowell, M., Zunker, H., Andersson, E., Balsamo, G., Bézy, J.-L., Brunhes, T., Bösch, H., Bojkov, B., Brunner, D., Buchwitz, M., Crisp, D., Ciais, P., Counet, P., Dee, D., van der Gon, H. D., Dolman, H., Drinkwater, M. R., Dubovik, O., Engelen, R., Fehr, T., Fernandez, V., Heimann, M., Holmlund, K., Houweling, S., Husband, R., Juvyns, O., Kentarchos, A., Landgraf, J., Lang, R., Löscher, A., Marshall, J., Meijer, Y., Nakajima, M., Palmer, P. I., Peylin, P., Rayner, P., Scholze, M., Sierk, B., Tamminen, J., &

Veefkind, P. (2020). Towards an operational anthropogenic CO2 emissions monitoring and verification support capacity. Bulletin of the American Meteorological Society, 101. https://doi.org/10.1175/BAMS-D-19-0017.1

Kaminski, Thomas, Peter J. Rayner, Martin Heimann, et Ian G. Enting. 2001. « On Aggregation Errors in Atmospheric Transport Inversions ». Journal of Geophysical Research: Atmospheres 106 (D5): 4703-15. https://doi.org/10.1029/2000JD900581.

Kuhlmann, Gerrit, Grégoire Broquet, Julia Marshall, Valentin Clément, Armin Löscher, Yasjka Meijer, et Dominik Brunner. 2019. « Detectability of CO2 Emission Plumes of Cities and Power Plants with the Copernicus Anthropogenic CO2 Monitoring (CO2M) Mission ». Atmospheric Measurement Techniques 12 (12): 6695-6719. https://doi.org/10.5194/amt-12-6695-2019.

Lespinas, Franck, Yilong Wang, Grégoire Broquet, François-Marie Bréon, Michael Buchwitz, Maximilian Reuter, Yasjka Meijer, et al. 2020. « The potential of a constellation of low earth orbit satellite imagers to monitor worldwide fossil fuel CO2 emissions from large cities and point sources ». Carbon Balance and Management 15 (1): 18. https://doi.org/10.1186/s13021-020-00153-4.

Levin I, Kromer B, Schmidt M, Sartorius H. A novel approach for independent budgeting of fossil fuel CO2 over Europe by 14CO2 observations. Geophys Res Lett. 2003;30(23).

Levin, I., & Karstens, U. (2007). Inferring high-resolution fossil fuel CO2 records at continental sites from combined 14CO2 and CO observations. *Tellus B*, *59*(2), 245–250. http://doi.org/10.1029/2005GL024213

Levin I, Naegler T, Kromer B, Diehl M, Francey RJ, Gomez-Pelaez AJ, et al. Observations and modelling of the global distribution and long-term trend of atmospheric 14CO2. Tellus, Ser B Chem Phys Meteorol. 2010;62(1):26–46.

Levin, I., Karstens, U., Eritt, M., Maier, F., Arnold, S., Rzesanke, D., et al. (2020). A dedicated flask sampling strategy developed for ICOS stations based on CO2 and CO measurements and STILT footprint modelling. *Atmospheric Chemistry and Physics Discussions*, 1–29. http://doi.org/10.5194/acp-2020-185

Lian, J., Breon, F.-M., Broquet, G., Zheng, B., Ramonet, M., & Ciais, P. (2020). Quantitative evaluation of the uncertainty sources for the modeling of atmospheric CO_2 concentration within and in the vicinity of Paris city. *Atmospheric Chemistry and Physics Discussions*, 1–22. http://doi.org/10.5194/acp-2020-540

Lin, J. C., Gerbig, C., Wofsy, S. C., Andrews, A. E., Daube, B. C., Davis, K. J., & Grainger, C. A. (2003). A near-field tool for simulating the upstream influence of atmospheric observations: The Stochastic Time-Inverted Lagrangian Transport (STILT) model. *Journal of Geophysical Research*, *108*(D16), ACH 2–1–ACH 2–17. http://doi.org/10.1029/2002JD003161

Lin, J. C., Gerbig, C., Wofsy, S. C., Andrews, A. E., Daube, B. C., Grainger, C. A., et al. (2004). Measuring fluxes of trace gases at regional scales by Lagrangian observations: Application to the CO 2Budget and Rectification Airborne (COBRA) study. *Journal of Geophysical Research*, *109*(D15), 401. http://doi.org/10.1126/science.260.5112.1314

Lopez M, Schmidt M, Delmotte M, Colomb A, Gros V, Janssen C, et al. CO, NOx and 13CO2 as tracers for fossil fuel CO2: Results from a pilot study in Paris during winter 2010. Atmos Chem Phys. 2013;13(15):7343–58.

Mahadevan, Pathmathevan, Steven C. Wofsy, Daniel M. Matross, Xiangming Xiao, Allison L. Dunn, John C. Lin, Christoph Gerbig, J. William Munger, Victoria Y. Chow, et Elaine W. Gottlieb. 2008. « A Satellite-Based Biosphere Parameterization for Net Ecosystem CO2 Exchange: Vegetation Photosynthesis and Respiration Model (VPRM) ». Global Biogeochemical Cycles 22 (2). https://doi.org/10.1029/2006GB002735.

Menut, L., B. Bessagnet, D. Khvorostyanov, M. Beekmann, N. Blond, A. Colette, I. Coll, et al. 2013. « CHIMERE 2013: A Model for Regional Atmospheric Composition Modelling ». Geoscientific Model Development 6 (4): 981-1028. https://doi.org/10.5194/gmd-6-981-2013.

Oda et al., 2018

Oda T, Maksyutov S, Andres RJ. The Open-source Data Inventory for Anthropogenic CO2, version 2016 (ODIAC2016): A global monthly fossil fuel CO2 gridded emissions data product for tracer transport simulations and surface flux inversions. Earth Syst Sci Data. 2018;10(1):87–107.

Pickers, P. (2016), New applications of continuous atmospheric O2 measurements: meridional transects across the Atlantic Ocean, and improved quantification of fossil fuel-derived CO2, PhD. dissertation, School of Environmental Sciences, University of East Anglia, 291 pp.

Pickers, P. A., Manning, A. C., Le Quéré, C., Gerbig, C., Hoshina, Y., Tohjima, Y., Luijkx, I. T., Forster, G. L., and Sturges, W. T. (under review) Quantifying fossil fuel CO_2 using atmospheric O2 observations, Nature Climate Change, 2020.

Pisso I, Patra P, Takigawa M, Machida T, Matsueda H, Sawa Y. Assessing Lagrangian inverse modelling of urban anthropogenic CO2 fluxes using in situ aircraft and ground-based measurements in the Tokyo area. Carbon Balance Manag. 2019;14(1).

Pisso I, Sollum E, Grythe H, Kristiansen N, Cassiani M, Eckhardt S, et al. The Lagrangian particle dispersion model FLEXPART version 10.4. Geosci. Model Dev. 12, 4955–4997 (2019).

Rödenbeck, C., Houweling, S., Gloor, M., & Heimann, M. (2003). CO2 flux history 1982–2001 inferred from atmospheric data using a global inversion of atmospheric transport. *Atmospheric Chemistry and Physics*, *3*, 1919–1964. http://doi.org/10.5194/acp-3-1919-2003

Santaren, Diego, Grégoire Broquet, François-Marie Bréon, Frédéric Chevallier, Denis Siméoni, et Philippe Ciais. 2020. « A Local to National-Scale Inverse Modeling System to Assess the Potential of Spaceborne CO2 Measurements for the Monitoring of Anthropogenic Emissions ». Atmospheric Measurement Techniques Discussions, mai, 1-41. https://doi.org/10.5194/amt-2020-138.

Staufer, J., Broquet, G., Breon, F.-M., Puygrenier, V., Chevallier, F., Xueref-Remy, I., et al. (2016). The first 1-year-long estimate of the Paris region fossil fuel CO_2 emissions based on atmospheric inversion. *Atmospheric Chemistry and Physics*, *16*(22), 14703–14726. http://doi.org/10.1029/2005JD006003

Super, I., van der Gon, H. A. C. D., Visschedijk, A. J. H., Moerman, M. M., Chen, H., van der Molen, M. K., & Peters, W. (2017). Atmospheric Pollution Research. *Atmospheric Pollution Research*, *8*(1), 174–187. http://doi.org/10.1016/j.apr.2016.08.008

Super, Ingrid, Stijn N. C. Dellaert, Antoon J. H. Visschedijk, et Hugo A. C. Denier van der Gon. 2020. « Uncertainty Analysis of a European High-Resolution Emission Inventory of CO2 and CO to Support Inverse Modelling and Network Design ». Atmospheric Chemistry and Physics 20 (3): 1795-1816. https://doi.org/10.5194/acp-20-1795-2020.

Tarantola, Albert. 2005. Inverse Problem Theory and Methods for Model Parameter Estimation. Society for Industrial and Applied Mathematics. https://doi.org/10.1137/1.9780898717921.

Turnbull, J. C., Miller, J. B., Lehman, S. J., Tans, P. P., Sparks, R. J., & Southon, J. (2006). Comparison of 14CO2, CO, and SF6 as tracers for recently added fossil fuel CO2 in the atmosphere and implications for biological CO2 exchange. *Geophysical Research Letters*, *33*(1), n/a–n/a. http://doi.org/10.1034/j.1600-0889.1996.00013.x

Turnbull, Jocelyn, Peter Rayner, John Miller, Tobias Naegler, Philippe Ciais, et Anne Cozic. 2009. « On the Use of 14CO2 as a Tracer for Fossil Fuel CO2: Quantifying Uncertainties Using an Atmospheric Transport Model ». Journal of Geophysical Research: Atmospheres 114 (D22). https://doi.org/10.1029/2009JD012308.

Vogel, F. R., Levin, I., & Worthy, D. E. J. (2013). Implications for Deriving Regional Fossil Fuel CO_2 Estimates From Atmospheric Observations in a Hot Spot of Nuclear Power Plant $14CO_2$ Emissions. *Radiocarbon*, *55*(2-3), 1556–1572.

Vogel, F., Hamme, S., Steinhof, A., Kromer, B., & Levin, I. (2017). Implication of weekly and diurnal 14C calibration on hourly estimates of CO-based fossil fuel CO 2ata moderately polluted site in southwestern Germany. *Tellus B*, *62*(5), 512–520. http://doi.org/10.1007/s00114-007-0313-4

Wang, Peng, Weijian Zhou, Zhenchuan Niu, Peng Cheng, Shugang Wu, Xiaohu Xiong, Xuefeng Lu, et Hua Du. 2018. « Emission characteristics of atmospheric carbon dioxide in Xi'an, China based on the measurements of CO2 concentration, △14C and δ13C ». Science of The Total Environment 619-620 (avril): 1163-69. https://doi.org/10.1016/j.scitotenv.2017.11.125.

Wang, Yilong. 2016. « The Potential of Observations of Radiocarbon in Atmospheric CO2 for the Atmospheric Inversion of Fossil Fuel CO2 Emission at Regional Scale », novembre. https://tel.archives-ouvertes.fr/tel-01529200.

Wang, Yilong, Grégoire Broquet, François-Marie Bréon, Franck Lespinas, Michael Buchwitz, Maximilian Reuter, Yasjka Meijer, et al. 2020. « PMIF v1.0: Assessing the Potential of Satellite Observations to Constrain CO2 Emissions from Large Cities and Point Sources over the Globe Using Synthetic Data ». Geoscientific Model Development 13 (11): 5813-31. https://doi.org/10.5194/gmd-13-5813-2020.

Wang, Yilong, Grégoire Broquet, Philippe Ciais, Frédéric Chevallier, Felix Vogel, Nikolay Kadygrov, Lin Wu, Yi Yin, Rong Wang, et Shu Tao. 2017. « Estimation of observation errors for large-scale atmospheric inversion of CO2 emissions from fossil fuel combustion ». Tellus

B: Chemical and Physical Meteorology 69 (1): 1325723. https://doi.org/10.1080/16000889.2017.1325723.

van der Werf, G. R., Randerson, J. T., Giglio, L., Collatz, G. J., Mu, M., Kasibhatla, P. S., et al. (2010). Global fire emissions and the contribution of deforestation, savanna, forest, agricultural, and peat fires (1997–2009). *Atmospheric Chemistry and Physics*, *10*(23), 11707–11735. http://doi.org/10.5194/acp-10-11707-2010

Wu, Lin, Grégoire Broquet, Philippe Ciais, Valentin Bellassen, Felix Vogel, Frédéric Chevallier, Irène Xueref-Remy, et Yilong Wang. 2016. « What Would Dense Atmospheric Observation Networks Bring to the Quantification of City CO₂ Emissions? » Atmospheric Chemistry and Physics 16 (12): 7743-71. https://doi.org/10.5194/acp-16-7743-2016.

Zazzeri, G., E. Acuña Yeomans, et H. D. Graven. 2018. « Global and Regional Emissions of Radiocarbon from Nuclear Power Plants from 1972 to 2016 ». Radiocarbon, juin, 1-15. https://doi.org/10.1017/RDC.2018.42.

Document History

Version	Author(s)	Date	Changes
	Name (Organisation)	dd/mm/yyyy	
0.0	F Chevallier (CEA) and all authors	11/01/2021	Initial full draft
1.0	F Chevallier (CEA) and all authors	04/02/2021	Consolidated version

Internal Review History

Internal Reviewers	Date	Comments
Daniel Thiemert	04/02/2021	Approved

Estimated Effort Contribution per Partner

Partner	Effort
CEA	4 person-months
Empa	5 person-months
MPG	21 person-months
NILU	4.5 person-months
UEA	5 person-months
Total	**39.5 person-months**